Implications of Stability Modeling for High-Speed Axial Compressor Design

by

Luc G. Fréchette

B. Ing. Génie Méchanique, École Polytechnique de Montréal (1994)

Submitted to the Department of Aeronautics and Astronautics
in partial fulfillment of the requirements for the degree of

Master of Science

at the

Massachusetts Institute of Technology

February 1997

Author_____
Department of Aeronautics and Astronautics
January 10, 1997

Certified by_____
Professor Alan H. Epstein
R. C. Maclaurin Professor of Aeronautics and Astronautics
Thesis Supervisor

Accepted by_____
Professor Jaime Peraire
Associate Professor of Aeronautics and Astronautics
Chair, Graduate Office

Implications of Stability Modeling for High-Speed Axial Compressor Design

by

Luc G. Fréchette

Abstract

This thesis is a first study of the uses of modern stability modeling in the design of compressors. A methodology for predicting and analyzing the fluid dynamics leading to rotating stall and surge in high-speed axial compressors is established, based on an existing two-dimensional, linear, compressible modal stall and surge inception model. It allows three main issues to be addressed concerning the use of stability modeling:

New concepts for addressing stability of high-speed compressors - The stability of pre-stall modes is explained using an original energy-based analysis of instability inception in high-speed compressors. A Disturbance-Energy Corollary is developed and applied to compressor pre-stall flow fields. This new tool allows the individual blade row energy contributions to overall stability of high-speed, multistage compressors to be determined.

Error analysis on stability analysis - The predictive capability of the stability model is assessed. From an error propagation analysis, the total uncertainty range on surge margin prediction due to input errors is found to be 3.6% (nominal surge margin of 21.2%), for a representative 11 stage high-speed axial compressor. The main sources of uncertainty are the steady flow parameters (contributing $\frac{3}{4}$ of the uncertainty) and the time lag constant for losses (contributing almost $\frac{1}{4}$ of the uncertainty).

Compressor modifications for enhancing stability - The effects of compressor design parameters on stability are addressed. A sensitivity analysis determines the trends, which are explained by energy-based arguments. A methodology for compressor design (or redesign) using stability modeling is proposed and illustrated. Minor modifications of the 11 stage compressor improve the surge margin by up to 5.6% (25% of the nominal surge margin) by re-optimizing variable guide vane stagger settings. Modifications maximizing surge margin and conserving steady performance are determined using this new technique and suggests modifications which are not obvious from conventional techniques. This indicates the usefulness of these stability modeling ideas in compressor design.

Thesis Supervisor: Professor Alan H. Epstein
Title: R. C. Maclaurin Professor of Aeronautics and Astronautics

ACKNOWLEDGMENTS

The results of this research would not be what they are without the contributions of many.

First, I wish to thank to Professor Epstein for having confidence in me and offering me this project. His support, interest, discussions, and original views were greatly appreciated.

I am also indebted to Harald Weigl for his unmeasurable help throughout this research. Without his knowledge, interest and close collaboration, this work would not have been possible. This team work was not only educative, but also very pleasant.

I also wish to thank Professor Paduano. His interest, patience, and insightful comments and ideas solved many problems and help guiding this research. His advisory role is greatly acknowledged.

My research and learning during the past years at MIT is also the result of working with others, whom I wish thank:

- Professor Greitzer for the enlightening discussions and for exemplifying the qualities of a good researcher;
- Dr. Choon Tan, Professor McGee, Dr. Gavin Hendricks and Dr. Jayant Sabnis for interest in my research, discussions and suggestions;
- Ken Gordon for the many discussions and especially for opening the door leading to the energy-based analysis in this thesis;
- Charles LeJambre for mindfully supplying me with input uncertainty for the error propagation analysis;
- The students in the smart-engine group for entertaining my questions and asking me for a hint of knowledge.

I must also thank the GTL crowd for making the work here that much more enjoyable. Thanks for making my MIT experience more than academic by many ways: from basketball to lunch-time discussions! In particular, I thank my former and current officemates for their cheerfulness and friendships.

Finally, I thank my family and friends for the support and good times, keeping the spirits always high. In particular, I wish to thank my parents for their inspiring determination, and Élise, without her belief in me, I would never have made it here.

This project was supported by United Technologies Corporation, Pratt & Whitney and the US Air Force Office of Scientific Research. This support is gratefully acknowledged

CONTENTS

List of Figures

List of Tables

NOMENCLATURE

Roman

$axdr$	axial velocity-density ratio across a blade row $(\frac{\rho_2 V_{x,2}}{\rho_1 V_{x,1}})$
$AVDR$	axial velocity-density ratio between the blade row leading edge and the inlet $(\frac{\rho_1 V_{x,1}}{\rho_{in} V_{x,in}})$
a	speed of sound $(\sqrt{\gamma RT})$
A	annulus area
B_n	upstream potential wave coefficient
C_n	downstream potential wave coefficient
c	axial velocity ratio across blade row $(\frac{V_{x,2}}{V_{x,1}})$
C	axial velocity ratio between the blade row leading edge and inlet $(\frac{V_{x,1}}{V_{x,in}})$
c_x	axial chord
D_n	vortical wave coefficient
E_n	entropic wave coefficient
I_{br}	blade row continuity parameter $(\frac{W}{V_{x,1}})$
j	imaginary unit $(\sqrt{-1})$
M	Mach number $(\frac{V}{a})$
N	Total number of blade rows in the compressor
n	harmonic number
P	pressure
r	mean radius
s	eigenvalue, or Laplace variable
δs	entropy perturbation
t	time

T	temperature
TS	total-to-static pressure rise parameter (Eqn A.39)
V	velocity
W	blade passage relative velocity

Greek

α	absolute flow angle
α_n	upstream potential wave propagation coefficient
β	relative flow angle
β_n	downstream potential wave propagation coefficient
χ	non-dimensional axial coordinate
χ_n	convecting wave coefficient
γ	Ratio of specific heats
δ°	deviation angle
δ	prefix denoting a perturbation quantity
κ	blade metal angle
Λ_{row}	single blade row inertia
λ	sum of rotor inertias
μ	sum of all blade row inertias
σ	real part of the eigenvalue (stability)
ω	imaginary part of the eigenvalue divided by n (frequency)
ω_{vor}	vorticity
ω_l'	relative total pressure loss coefficient
Ω	rotor frequency
ϕ	non-dimensional axial velocity (flow coefficient)
ψ	non-dimensional pressure rise across a blade row
Ψ	non-dimensional pressure rise across the entire compressor
ρ	density
ϱ	non-dimensional density

τ	non-dimensional time
τ_p	total pressure loss time lag constant
τ_d	deviation time lag constant
θ	tangential coordinate
υ	axial momentum ratio across a blade row ($\frac{\rho_2 V_{x,2}^2}{\rho_1 V_{x,1}^2}$)
Υ	axial momentum ratio between the blade row leading edge and the inlet ($\frac{\rho_1 V_{x,1}^2}{\rho_{in} V_{x,in}^2}$)
φ	velocity potential
ϑ	non-dimensional tangential velocity
ξ	blade row stagger angle

Subscripts

x	axial component
θ	tangential component
in	inlet value
ex	exit value
1	leading edge value
2	trailing edge value
n	n^{th} harmonic quantity
N	last blade row value
t	stagnation (or total) fluid quantity
o	reference value used for non-dimensionalization

Superscripts

$'$	relative frame value
ss	static-to-static (exit static minus inlet static)
ts	total-to-static (exit static minus inlet total)

Other useful notations

CFD	computational fluid dynamics
SM	surge margin
IGV	inlet guide vanes
VGV	variable guide vanes
2D	two-dimensional (x and θ)
3D	three-dimensional (r, x and θ)
pdli	partial derivative of loss coefficient versus incidence, $\frac{\partial \omega_l'}{\partial inc}$
pdlm	partial derivative of loss coefficient versus Mach number, $\frac{\partial \omega_l'}{\partial M_1'}$
pddi	partial derivative of deviation versus incidence, $\frac{\partial dev}{\partial inc}$
pddm	partial derivative of deviation versus Mach number, $\frac{\partial dev}{\partial M_1'}$
wloss	relative total pressure loss coefficient, ω_l'
$\bar{(\cdot)}$	mean value
$\tilde{(\cdot)}$	blade row passage coefficient
$\vec{(\cdot)}$	vector
$[\cdot]$	matrix
$< \cdot >$	area averaged value

CHAPTER 1

INTRODUCTION

Axial compressors, as used in gas turbine engines, exhibit inherent fluid dynamic instabilities when they are driven to higher pressure ratios and lower mass flows. These instabilities, *rotating stall* and *surge*, are important because they limit the performance of the engine and restrict the safe operating range. Surge is basically a circumferentially uniform pulsation of the mass flow through the machine, while rotating stall appears as a reduced flow region in part of the circumference, which travels around the annulus at a fraction of the rotor speed, as depicted in Figure 1-1. A comprehensive review of the flow instabilities present in compression systems is given by Greitzer [14]. Both rotating stall and surge reduce the pressure rise in the machine and can introduce severe mechanical distress. In high speed compressors, rotating stall is generally encountered first, which then (loosely) "triggers" the surge, so the emphasis in this thesis will mostly be rotating stall.

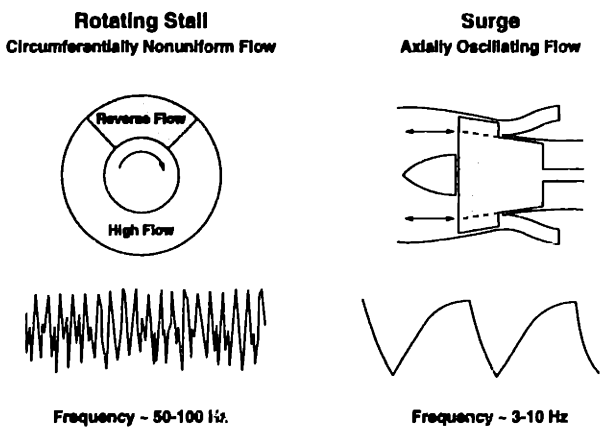

Figure 1-1: Illustration of rotating stall and surge (from [14]). A sketch of the transient signatures that would be given by high response pressure probes in the compressor (for rotating stall) or in the combustor, or other volume downstream of the compressor (for surge).

1.1 The inception of rotating stall

Fully-developed rotating stall can be initiated by at least two types of phenomena: short length-scale (of the order of the blade passage width) and long length-scale (of the order of the compressor annulus). The long length-scale phenomena is usually called *modal stall inception* since it can be represented by a combination of spatial modes with wavelengths equal to some significant portion of the circumference. These pre-stall modes start as small amplitude waves rotating around the annulus of the compressor. As the mass flow is reduced, they grow smoothly, but rapidly, to large amplitude rotating stall. The initial growth or decay of the small amplitude modes has been modeled at various levels of complexity. Following the introduction of the basic model for modal stall inception in low speed axial compressors by Moore and Greitzer [35], Bonnaure developed a model applicable for high speed axial compressors [1]. Pre-stall waves proposed by these models have been identified in low speed and high-speed compressors [12, 42].

These models have been useful for understanding the phenomena and also in proposing strategies to stabilize compression systems. Considerable effort has been given over the past few years in actively controlling the inception of surge and rotating stall [9]. With success, researchers have extended the stable operating region to lower mass flows by sensing the pre-stall waves and damping them out by oscillating vanes [38, 16, 43], or injecting air [15, 47, 44].

The second type of stall inception, *short length-scale inception*, consists of degraded flow in a single or a few blade passages that leads to local flow reversal which then grows to a fully-developed rotating stall cell after only a few rotor revolutions. Characteristic features of this type of stall inception have been seen experimentally by Day [5] in the form of a "spike" in a velocity trace a few revolutions before stall. Although a predictive model for this short length-scale stall inception hasn't been developed yet, physical features have been conjectured by Hoying [19] through computational fluid dynamics (CFD). The tip vortex attached to the leading edge tends to move up in the blade passage, turning from the axial direction to tangential as the mass flow is reduced. Stability of this vortex then depends on the balance between the mean flow convecting it downstream and the vortex inducing itself upstream due to the presence of the casing wall. The short length-scale stall inception

therefore mainly depends on the local flow in a blade passage as opposed to the long length-scale, which depends on flow field in the entire compression system. This thesis will focus on modal stall since models are available and since this type of stall inception in known to be present in many high-speed axial compressors [42].

1.2 Compressor design and stability modeling

Compressors are ideally designed to operate at their maximum efficiency. However, a certain margin must be allowed between the normal operating point and the region of instability. This *surge margin* is necessary in order to withstand transient operation of the engine and safe operation as the compressor performance degrades[1]. The requirement for surge margin reduces the available operating pressure rise from a given machine and can reduce the operating efficiency as well, as shown in Figure 1-2.

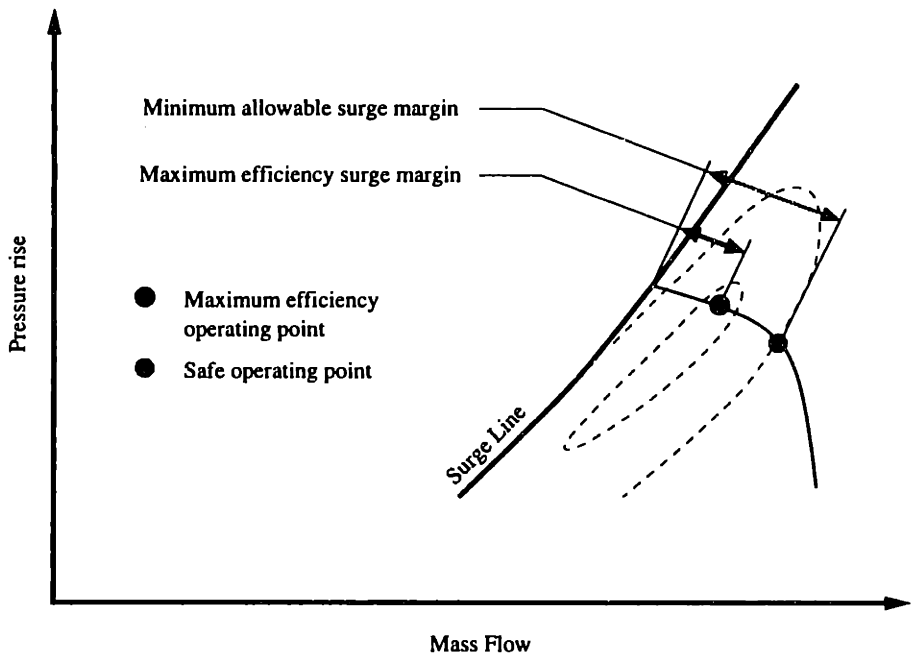

Figure 1-2: Compressor map illustrating the surge margin.

The compressor design procedure is mainly aimed at providing a component delivering the necessary pressure rise and mass flow at a maximum efficiency. The design effort is therefore

[1]The term "surge margin" will be used to denote the distance on the compressor map between the operating point and the region of instability, whether the instability is surge or rotating stall. A general term such as "stability margin" would more appropriate.

concentrated at the nominal operating point. However, the surge margin is determined by the off-design operation of the compressor. This surge margin is a consequence of the performance optimization done at the nominal operating point. Usually, improvements in performance tend to reduce the surge margin [30], so the compression system needs to be modified in order to retain the surge margin, using various classical methods [3].

Since the physical understanding of rotating stall and surge has rapidly evolved over the past decade, new methods for predicting and improving stability of the compression systems are becoming available. Modeling of the rotating stall and surge dynamics has been useful to active control efforts, but hasn't been exploited in the basic design phase of the compressor. These models and concepts could be used during the design process to ensure adequate surge margin, complementing or replacing the correlations and databases currently used to predict the surge line. Stability models can improve the compressor design procedure by:

- predicting the surge line;
- indicating compressor design modifications to improve stability.

In the past years, the compressor design procedures have been evolving, mostly through the increased use of computational fluid dynamics. Such procedures could also be improved by including the use of compression system stability models. The latest procedure used by Pratt & Whitney in designing the growth version of the PW4000's high pressure compressor [30] could be augmented by the stability analysis, shown as the shaded block in Figure 1-3.

This additional step could favorably impact the development time and cost since the stability can be investigated and a few design iterations can been done to improve stability before rig and engine testing. The use of stability models may also reduce the risk associated with developing innovative designs since the surge margin can be predicted and doesn't rely on engine manufacturer knowledge acquired from previous designs.

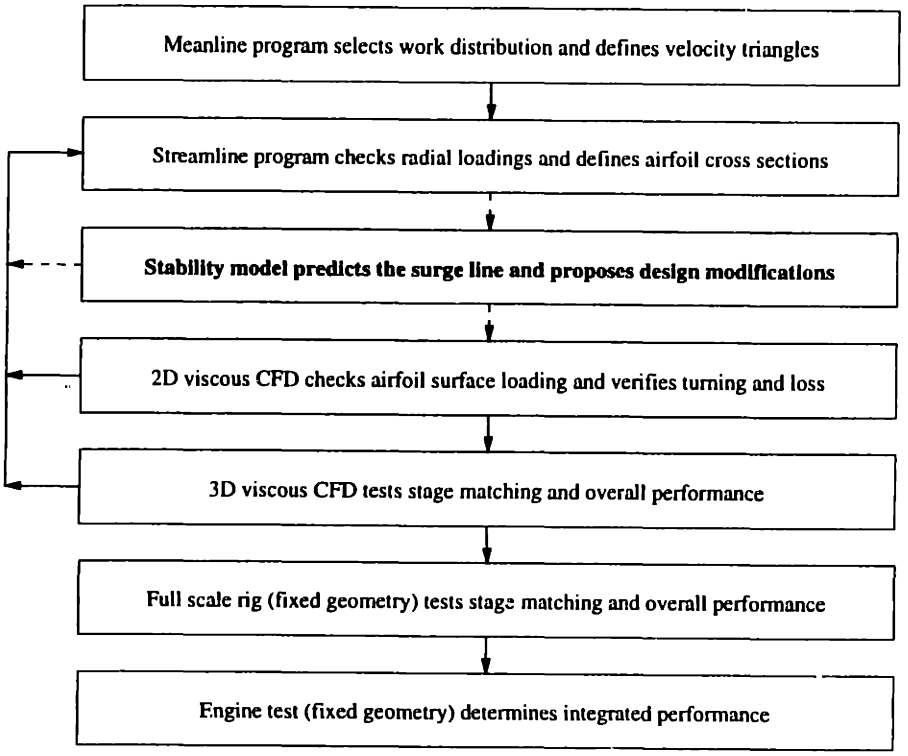

Figure 1-3: Compressor design process with added stability analysis step (modified from [30]).

1.3 Scope of the present research

For these models to be of use to industry, they must be well understood, be representative of the currently designed compressors (such as high-speed multistage compressors) and offer the required accuracy. This thesis will use a version of Bonnaure's 2-D compressible model for prediction of surge and modal stall inception dynamics of high-speed multistage compressors, extended and reformulated by Feulner [10], and focus on:

1. Describing and elucidating the underlying physics of modal stall inception, especially in high-speed axial compressors;
2. Assessing the predictive capabilities of this type of modeling, through an error propagation analysis;
3. Illustrating methods for improving the stability of compressors using stability modeling.

The thesis is structured about these three main aspects. Chapter 2 reviews the stability models, starting with the incompressible models to introduce the basic physics involved

in rotating stall inception, then followed by the compressible model, its flow physics, and its utilization. Chapter 3 then presents an energy-based explanation for the inception of rotating stall in low-speed and high-speed compressors, leading to a better physical understanding of modal stall inception. Chapter 4 assesses how well the modeling parameters need to be known for accurate surge line prediction. The effect of compressor design parameters on stability are discussed in Chapter 5, along with a method for designing (or redesigning) compressors for enhanced stability. A few examples demonstrate the applicability of stability modeling to compressor design. Finally, Chapter 6 will summarize the results and propose future work to be done.

A modern 11-stage high-speed core compressor representative of current designs for gas turbine engines is chosen for this study. The compressor is composed of 23 blade rows: inlet guide vanes (IGV), 11 rotors, and 11 stators; where the IGV's and first three stators have variable stagger angle. The setting angles of these variable guide vanes (VGV) are mainly a function of rotor speed. They are varied in order to alleviate the stage matching problems encountered when the multistage compressor is operating off its design conditions. Also, air is extracted from the main flow path through bleed ports at two axial locations: after the 10^{th} and 16^{th} blade rows (5^{th} and 8^{th} stage). Compressor bleed air is used to cool engine components and for various aircraft purposes. These VGV angle settings and the bleeds are controlled by the electronic engine control, based on the piloting commands and various measured engine operating parameters.

CHAPTER 2

MODELING THE INCEPTION OF ROTATING STALL

This Chapter describes tools used for predicting axial compressor stability. Although the focus is on the *compressible*, linear, 2-D model for high-speed multistage axial compressor modal stall inception, *incompressible* models will first be reviewed and reformulated in Section 2.1 to introduce the basic dynamics of rotating stall and prepare for the compressible model. Section 2.2 presents the compressible, linear, 2-D model, followed by the main features of pre-stall dynamics in Section 2.3.

2.1 Incompressible rotating stall inception models

In this section, the classic Moore-Greitzer rotating stall model is reviewed, stating that the slope of the overall total-to-static pressure rise characteristic governs the compressor stability. To bridge the gap between this simple model and the complex compressible model, a more detailed incompressible formulation of the Moore-Greitzer model is presented. Finally, additional blade row dynamics (unsteady loss and deviation) are reviewed.

2.1.1 Classic linearized Moore-Greitzer formulation

Rotating stall models for low speed compressors have evolved since their introduction in the eighties. The classic formulation was proposed by Moore and Greitzer [35], where the

flow field is considered incompressible. The linearized form of this model can be used to determine whether the compressor will stall at a given operating condition by assessing the stability of small amplitude flow field perturbations which travel around the compressor annulus. Each flow quantity is decomposed into a steady mean value and a small perturbation. For example, the axial flow coefficient is linearized as:

$$\phi(x,\theta,t) = \bar{\phi} + \delta\phi(x,\theta,t) \tag{2.1}$$

As part of the model formulation, these traveling perturbation waves are decomposed into sinusoidal circumferential harmonics, leading to axial flow perturbations of the form:

$$\delta\phi(x,\theta,t) = \sum_{n=-\infty}^{n=\infty} \bar{\phi}(x,n,t)e^{jn\theta} \tag{2.2}$$

The dynamics can be written and solved separately for each harmonic for a uniform mean flow (no inlet distortion), so each perturbation spatial harmonic is a mode of the system with a unique rotation rate and damping ratio.

The compressor is modeled as a steady pressure delivery (specified by the compressor characteristic), modified by the pressure difference necessary to overcome the unsteady flow in the blade rows. The blade rows are connected together assuming that the axial velocity and density are constant through the compressor. The pressure rise was considered not sensitive to inlet swirl perturbations and the last blade was assumed to let the flow exit strictly in the axial direction. Combining the compressor with semi-infinite ducts upstream and downstream leads to a first order time differential equation of the mass flow perturbation for each circumferential harmonic. By assuming:

- constant density;
- constant axial velocity;
- axial, uniform inlet flow;
- high-solidity exit stator (fixed exit flow angle);
- compressor pressure rise is only a function of the flow coefficient, $\Psi(\Phi)$;

the rotating stall inception dynamics are given by:

$$\left(\frac{2}{|n|}+\mu\right)\frac{\partial(\delta\phi)}{\partial\tau}=\left(\frac{\partial\Psi^{ts}}{\partial\phi}-jn\lambda\right)\delta\phi \tag{2.3}$$

The solution for $\delta\phi$ is then:

$$\delta\phi=\sum_{n=-\infty}^{n=\infty}a_n\,e^{(\sigma-jn\omega)\tau}\,e^{jn\theta} \tag{2.4}$$

where:

$$\begin{aligned}\sigma&=\frac{\frac{\partial\Psi^{ts}}{\partial\phi}}{\left(\frac{2}{|n|}+\mu\right)}\quad\text{(growth rate)}\\ \omega&=\frac{\lambda}{\left(\frac{2}{|n|}+\mu\right)}\quad\text{(rotation rate)}\end{aligned} \tag{2.5}$$

The inertia parameters, λ, μ, and $\frac{2}{|n|}$ represent the fluidic inertias in the rotors, rotors + stators, and inlet + exit ducts respectively. The blade row inertia parameters can be defined as:

$$\begin{aligned}\mu&=\sum_{\text{all rows}}\frac{c_x/r_o}{\cos^2\xi}\\ \lambda&=\sum_{\text{rotors}}\frac{c_x/r_o}{\cos^2\xi}\end{aligned} \tag{2.6}$$

with c_x/r_o representing the chord non-dimensionalized by the mean radius, and ξ, the stagger angle. The imaginary part of the eigenvalue (ω) is the frequency at which the pre-stall mode will rotate about the annulus, while its real part (σ) represents the stability of the compression system. Since the denominator (total compression system inertia) is always positive, the sign of the total-to-static pressure rise slope governs the stability of the mode:

$$\begin{aligned}&\frac{\partial\Psi^{ts}}{\partial\phi}>0:\text{ perturbations will grow }\rightarrow\text{ unstable}\\ &\frac{\partial\Psi^{ts}}{\partial\phi}<0:\text{ perturbations will decay }\rightarrow\text{ stable}\end{aligned}$$

Longley [31] expanded this formulation, allowing for inlet swirl sensitivity and for deviation at the last blade row.

2.1.2 Expanded formulation

These incompressible formulations are useful for analyzing low speed compressors with constant axial velocity, but they can be extended to give insight in analyzing high-speed compressors, which also have a mode that is incompressible-like (Section 2.3). To make use of this analytical formulation, the model should allow for non-uniform axial velocity and density from blade row to blade row.

Incorporating axial velocity variations enable us to model steady blockage and annulus contraction. Axial density variation relaxes the incompressibility assumption: no density perturbations are modeled, but the steady density is allowed to vary along the compressor (*non-uniform* density). These extensions to the classic formulation will be useful in gaining insight on the dynamics of the incompressible-like mode in multistage axial compressors, where V_x and ρ can change considerably along the compressor[1]. Furthermore, the overall pressure rise characteristic should be expanded into the pressure rise of each blade row and expressed as a function of the relative total pressure loss coefficients and deviations, instead of the overall total-to-static pressure rise characteristic. This expanded model then uses classic compressor design parameters, which are also used as input parameters to the compressible model.

Appendix A carries out the formulation of the 2-D, incompressible, linearized rotating stall model with non-uniform velocity and density (Section A.1). The overall pressure rise is allowed sensitivity to inlet swirl and the last blade row is allowed deviation as a function of mass flow and swirl at the face of the compressor.

[1]The density, for example, may increase by a factor of six across an 11-stage high-speed compressor. The axial velocity, even though compressors are usually designed with near constant V_x, may vary by a factor of two at off-design conditions, such as near stall.

The resulting dynamic equation is then Eqn A.43, repeated here:

$$\left(\frac{(AVDR_{ex}+1)}{|n|}+\mu\right)\frac{\partial(\delta\phi)}{\partial\tau}=\left[\left(TS_R-|n|(\Upsilon_{ex}\bar{\phi}^2\,d_{I,ex})\right)-jn\left(\lambda-TS_I-\frac{(\Upsilon_{ex}\bar{\phi}^2\,d_{R,ex})}{|n|}\right)\right]\delta\phi \tag{A.43}$$

where TS_R and TS_I are the real and imaginary parts of the total-to-static pressure rise perturbation, $\delta\Psi^{ts}=(TS_R+jnTS_I)\delta\phi$; $AVDR_{ex}$ is the axial velocity density ratio, $\frac{\rho_{ex}}{\rho_{in}}\frac{V_{x,ex}}{V_{x,in}}$; Υ_{ex} is the momentum ratio, $\frac{\rho_{ex}}{\rho_{in}}\left(\frac{V_{x,ex}}{V_{x,in}}\right)^2$; finally, $d_{R,ex}$ and $d_{I,ex}$ are the real and imaginary parts of the exit duct flow angle perturbation, $\delta\tan\alpha_{ex}=(d_{R,ex}+jn\,d_{I,ex})\,\delta\phi_{in}$.

This leads to the eigenvalue's real and imaginary parts $(\sigma-jn\omega)$ which are given by Eqns A.44 and A.45, repeated here:

$$\sigma=\frac{TS_R-|n|\Upsilon_{ex}\bar{\phi}^2\,d_{I,ex}}{\left(\frac{AVDR_{ex}+1}{|n|}+\mu\right)} \tag{A.44}$$

$$\omega=\frac{\lambda-TS_I-\frac{(\Upsilon_{ex}\bar{\phi}^2\,d_{R,ex})}{|n|}}{\left(\frac{AVDR_{ex}+1}{|n|}+\mu\right)} \tag{A.45}$$

with:

$$TS_R=\frac{\partial\Psi^{ts}}{\partial\phi}-\frac{\tan\bar{\alpha}_{in}}{\bar{\phi}}\frac{\partial\Psi^{ts}}{\partial\tan\alpha_{in}}$$

$$TS_I=\frac{1}{|n|\bar{\phi}}\frac{\partial\Psi^{ts}}{\partial\tan\alpha_{in}}$$

$$d_{R,ex}=\frac{\partial\tan\alpha_{ex}}{\partial\phi_{in}}-\frac{\tan\bar{\alpha}_{in}}{\bar{\phi}}\frac{\partial\tan\alpha_{ex}}{\partial\tan\alpha_{in}}$$

$$d_{I,ex}=\frac{1}{|n|\bar{\phi}}\frac{\partial\tan\alpha_{ex}}{\partial\tan\alpha_{in}}$$

$$\mu=\sum_{\text{all rows}}\frac{c_x/r_o}{\cos^2\xi}I_{br}\;AVDR$$

$$\lambda=\sum_{\text{rotors}}\frac{c_x/r_o}{\cos^2\xi}I_{br}\;\;AVDR$$

$$I_{br}=\frac{1+\frac{V_{x,2}}{V_{x,1}}}{2}$$

$$AVDR=\frac{\rho_1}{\rho_{in}}\frac{V_{x,1}}{V_{x,in}}$$

This formulation introduces parameters that are not usually found in the classic formula-

tions of the 2-D incompressible rotating stall model. According to Eqns A.44 and A.45, the parameters that govern the pre-stall dynamics are[2]:

1. Geometry
   - axial chords (c_x/r_o)
   - stagger angles (ξ)
2. Steady flow values
   - inlet axial flow coefficient ($\bar{\phi}$)
   - inlet swirl angle ($\bar{\alpha}_{in}$)
   - axial velocity ratios ($\frac{\bar{\phi}_2}{\phi_1}$) [3]
   - density ratios ($\frac{\rho_2}{\rho_1}$)
3. Overall performance slopes
   - overall pressure rise sensitivity to inlet flow coefficient ($\frac{\partial \Psi^{ts}}{\partial \phi}$)
   - overall pressure rise sensitivity to inlet swirl angle ($\frac{\partial \Psi^{ts}}{\partial \tan \alpha_{in}}$)
   - last blade row deviation sensitivity to inlet flow coefficient ($\frac{\partial \tan \alpha_{ex}}{\partial \phi}$)
   - last blade row deviation sensitivity to inlet swirl angle ($\frac{\partial \tan \alpha_{ex}}{\partial \tan \alpha_{in}}$)

For constant area and density, the above expressions simplify since $AVDR$, Υ and I_{br} are equal to 1. The resulting simplified form can be shown to be identical to the formulation of the linear rotating stall model presented by Longley ([31], Appendix B).

The *overall performance slopes* are a function of the performance of each blade row (individual pressure rise characteristics and efficiency curves). Using the expansion of the overall pressure rise into an expression containing the loss coefficient and deviation of each blade row will lead to a set of *blade row performance slopes*, replacing these *overall performance slopes*. Details of this expansion are found in Section A.2. The main equations will be summarized here.

[2] $AVDR$, Υ and I_{br} are only functions of the density ratios ($\frac{\rho_2}{\rho_1}$) and the axial velocity ratios ($\frac{\phi_2}{\phi_1}$) across blade rows.

[3] includes both the effects of blockage and annulus area contraction

Blade row performance slopes

The static pressure rise across a single blade row can be expressed as an isentropic pressure rise from which is subtracted a relative total pressure loss, $\psi^{ss} = \psi^{ss}_{is} - \psi_{loss}$, with:

$$\psi^{ss}_{is} = \frac{\varrho\phi_1^2}{2}\left[\tan^2\beta_1 - \upsilon\tan^2\beta_2 + 1 - \upsilon\right] \tag{A.50}$$

$$\psi_{loss} = \omega'_l\frac{\varrho\phi_1^2}{2}\left[1 + \tan^2\beta_1\right] \tag{A.55}$$

where ϱ is the non-dimensional density and υ is the axial momentum ratio across the blade row. The loss coefficient, ω'_l, and the relative exit flow angle, β_2, are given by the blade row performance, i.e. they are function of inflow conditions for a given blade row. As discussed in NASA SP-36 [22], the performance of cascades generally depend on the inlet relative Mach number, incidence angle and the Reynolds number. For subsonic cascades operating in the normal range of axial compressors, the only relevant parameter is the incidence angle. For given loss coefficient and deviation (or trailing edge relative flow angle) as a function of incidence angle (or leading edge relative flow angle), perturbations in loss coefficient and exit angle can be linearized as:

$$\delta\tan\beta_2 = \frac{\partial\tan\beta_2}{\partial\tan\beta_1}\,\delta\tan\beta_1 \tag{A.52}$$

$$\delta\omega'_l = \frac{\partial\omega'_l}{\partial\tan\beta_1}\,\delta\tan\beta_1 \tag{A.56}$$

where $\frac{\partial\tan\beta_2}{\partial\tan\beta_1}$ and $\frac{\partial\omega'_l}{\partial\tan\beta_1}$ are the slopes of the deviation and loss functions respectively.

The pressure rise perturbations as functions of the leading edge axial flow coefficient and flow angle perturbations ($\delta\phi_1$, $\delta\tan\beta_1$) are then:

$$\delta\psi_{is} = \varrho\bar{\phi}_1\left[\tan^2\bar{\beta}_1 - \upsilon\tan^2\bar{\beta}_2 + 1 - \upsilon\right]\delta\phi_1 + \frac{\varrho\bar{\phi}_1^2}{2}\left[(2\tan\bar{\beta}_1) - \upsilon(2\tan\bar{\beta}_2)\frac{\partial\tan\beta_2}{\partial\tan\beta_1}\right]\delta\tan\beta_1 \tag{A.53}$$

$$\delta\psi_{loss} = \varrho\bar{\phi}_1\bar{\omega}'_l\left[1 + \tan^2\bar{\beta}_1\right]\,\delta\phi_1 + \frac{\varrho\bar{\phi}_1^2}{2}\left[(1 + \tan^2\bar{\beta}_1)\frac{\partial\omega'_l}{\partial\tan\beta_1} + 2\,\bar{\omega}'_l\tan\bar{\beta}_1\right]\,\delta\tan\beta_1 \tag{A.57}$$

As shown in Section A.2, the incidence angle perturbation of the k^{th} blade row can be

related to the flow perturbation at the leading edge of the first blade row by:

$$\delta \tan\beta_1(k) = \Big(d_R(k) + jn\, d_I(k) \Big)\, \delta\phi \tag{A.65}$$

where:

$$d_R(k) = \frac{1}{\bar{\phi}^2} \sum_{l=1}^{k} \left[\frac{\Delta\Omega_{nd}(l)}{C(l)} \prod_{m=l}^{k-1} \left(\frac{\partial \tan\beta_2}{\partial \tan\beta_1}(m) \right) \right] - \frac{\tan\bar{\alpha}_{in}}{\bar{\phi}} \prod_{m=1}^{k-1} \left(\frac{\partial \tan\beta_2}{\partial \tan\beta_1}(m) \right)$$

$$d_I(k) = \frac{1}{|n|\bar{\phi}} \prod_{m=1}^{k-1} \left(\frac{\partial \tan\beta_2}{\partial \tan\beta_1}(m) \right)$$

We notice that the product of the deviation slopes ($\frac{\partial \tan\beta_2}{\partial \tan\beta_1}$) of upstream blade rows is the main parameter defining the incidence angle perturbation to the k^{th} blade row.

The overall total-to-static pressure rise perturbation is a summation of the static-to-static pressure rise perturbations of each blade row, from which is subtracted the inlet dynamic head perturbation:

$$\begin{aligned} \delta\Psi^{ts} &= \delta\Psi^{ss} - \bar{\phi}\delta\phi - jn\frac{\bar{\phi}\tan\bar{\alpha}_{in}}{|n|}\delta\phi \\ &= \sum_{\text{all rows}} \delta\psi_{is} + \sum_{\text{all rows}} \delta\psi_{loss} - \bar{\phi}\delta\phi - jn\frac{\bar{\phi}\tan\bar{\alpha}_{in}}{|n|}\delta\phi \end{aligned} \tag{A.46}$$

The analytical summation contains many terms and may be found in Section A.2.

The *overall performance slopes* listed as governing parameters earlier (page 26) can be replaced by the following *biade row performance slopes*:

- blade row pressure loss sensitivities to incidence angle ($\frac{\partial \omega_i'}{\partial \tan\beta_1}$)
- blade row deviation sensitivities to incidence angle ($\frac{\partial \tan\beta_2}{\partial \tan\beta_1}$)

2.1.3 Additional blade row dynamics

As first proposed by Emmons, Pearson and Grant [7], a first order rate equation:

$$\tau\frac{d(\cdot)}{dt} = (\cdot)_{steady-state} - (\cdot) \tag{2.7}$$

can be used to model the unsteady loss and deviation since they do not happen instantaneously. The time constants, τ, related to these lags are of the order of the flow through time across the blade passage. They represent the time needed for the instantaneous loss or deviation to reach steady-state given a perturbation of the inflow conditions. Including these lags was shown by Haynes [16] to be important for accurate modeling. They are shown to have a stabilizing effect, allowing the compressor to be stable at positive $\frac{\partial \Psi^{ts}}{\partial \phi}$. This effect is generally stronger for the higher circumferential harmonics, making the lower harmonics go unstable first as the throttle is closed.

2.2 Compressible stability model

The compressible, 2-D, linear stability model is presented here, emphasizing the physics rather than the mathematical formulation. The elements needed to address the issues in this thesis are presented along with the methodology for applying it to actual compressors. More details can be found in the theses of Bonnaure [1], Feulner [10], Weigl [45], and in Appendix B of this thesis.

2.2.1 Description of the compressible model

Overview

The rotating stall and surge inception in high-speed compressors is modeled by a hydrodynamic stability analysis of the compression system. The compression system is composed of rotors, stators and inter-blade row gaps forming the compressor, upstream and downstream ducts, and the boundary conditions at the far end of each duct. The boundary conditions represent the further upstream and downstream components and may introduce additional dynamics. An example is shown in Figure 2-1, where the downstream boundary condition will include the plenum and throttle dynamics, while the upstream boundary condition is simply an open end impedance condition.

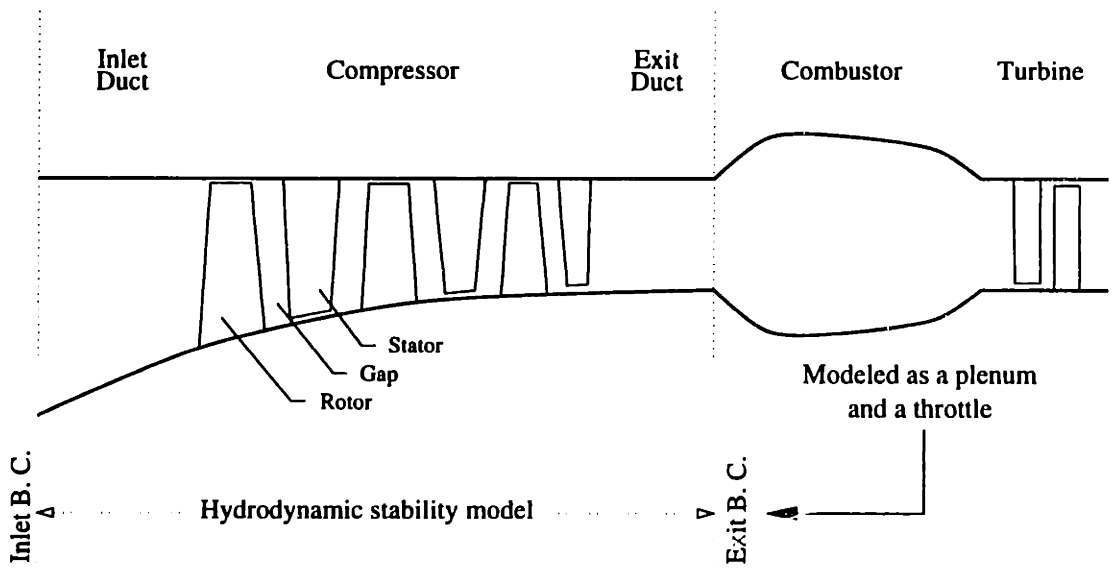

Figure 2-1: Schematic of a modeled compression system.

The model is two-dimensional, in the axial and tangential directions. The analysis superposes two-dimensional disturbances on a steady, mean 2-D flow field. The compression system is decomposed into basic elements: ducts, blade rows, and gaps. Each element has an axially and circumferentially uniform mean flow. The propagation of the flow disturbances within each element can then be expressed analytically. These analytical expressions for the disturbances are connected between elements through appropriate matching conditions. Once coupled with the inlet and exit boundary conditions, the evolution of the disturbances can be solved for, giving the pre-stall unsteady flow field and the rate at which it grows (or decays) and rotates around the annulus. The system of equations is however too complex to directly solve analytically and obtain a closed form expression for the eigenvalues (as was done with the Moore-Greitzer formulation), so numerical methods are used.

Overall, this modeling approach can be considered as a generalization of the incompressible analysis of Moore [34] and Moore and Greitzer [35] to include compressible flow. The modeling of the blade rows is however different. Each blade row is considered as a parallel set of inviscid, 1-D ducts inclined at the stagger angle, as shown in Figure 2-2. The leading and trailing edge matching conditions are actuator disks accounting for the pressure loss across the blade row and the deviation.

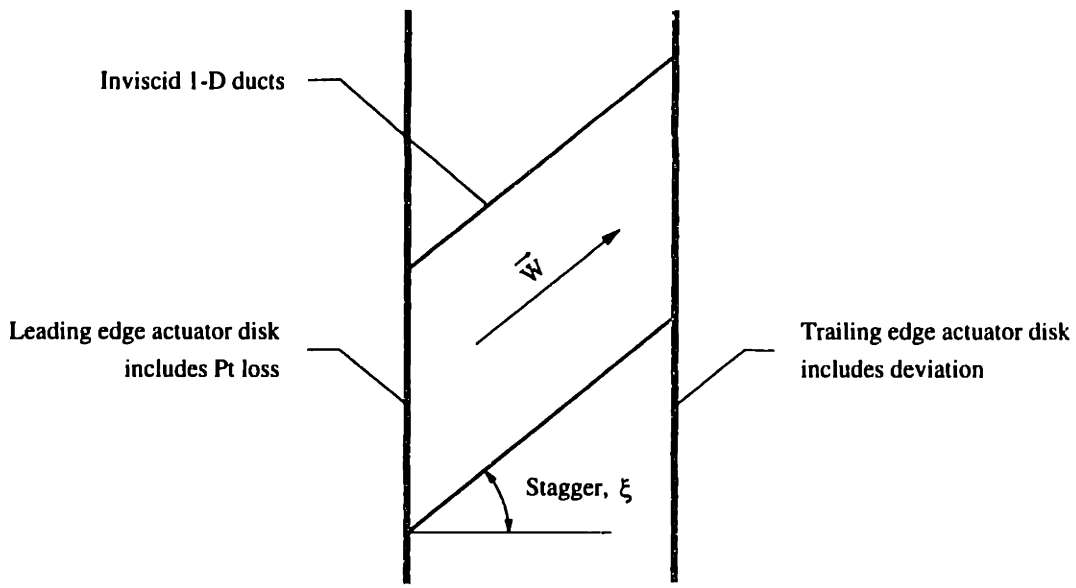

Figure 2-2: 1-D model of the blade rows in *2DCompSIM*.

This type of analysis was introduced in 1970 by Kaji and Okazaki [23], then used by Cumpsty and Marble for sound transmission across turbines [4] and by Hynes for inlet

distortion effects [20]. The first application to rotating stall was by Bonnaure in 1991 [1]. He developed the analytical formulation as a non-standard eigenvalue problem and solved for the eigenvalues using the Nyquist criterion or a graphical method. This code was improved and used by Hendricks [17] to investigate the effects of compressor loading distribution and other parameters on the stability of high-speed compressors. This model was then recast in state-space form by Feulner [10], who also included the effect of actuation, such as injection of air in circumferentially varying patterns. This reformulation allows for control theory to be applied to the system dynamics, but also provides a rapid solution for the system dynamics since the eigenvalue computation becomes a trivial application of matrix eigenvalue routines. This state-space version has since been further developed as required for various applications. Through the work in this thesis and the modeling of NASA Stage 35 for active control of rotating stall [47, 45], mistakes have been corrected, the implementation of the model has been improved, and routines to prepare the inputs to the model and analyze its results have been developed. An update on this work is given by Weigl and Fréchette [46]. The model and its related routines are combined in the *2DSIM Toolbox* described in Appendix B. This latest version of the state-space model will be referred to as *2DCompSIM*, which stands for: 2-D Compressible rotating Stall and surge Inception Model.

Underlying fluid dynamics

As shown by Kovasznay [28], there are three types of disturbances that exist in steady mean flow: *potential* disturbances (which carry the pressure information); *vortical* disturbances; and *entropic* disturbances. These three basic types of disturbances are decoupled and evolve independently if the mean flow is uniform[4] and the disturbances are inviscid and non-conducting[5]. They are only linked through the matching conditions at each blade row, and

[4]The situation would be different if we had a 3-D flow field. As shown by Kerrebrock [24], the presence of a swirling mean flow couples the disturbances. With strong rotation for example, a tangential velocity perturbation implies a *radial* (Coriolis) force perturbation which leads to a pressure fluctuation, thus coupling the vorticity mode to the potential mode. Since our analysis is two-dimensional, the radial equations of motion are not considered and therefore the three basic types of disturbances remain decoupled.

[5]Not only must the viscous and heat transfer effects be negligible with the surroundings, but also *within* the fluid. Flow perturbations introduce gradients in velocity and temperature. The potential, vortical and entropic disturbances are decoupled only if the scales of viscous thermal diffusion allow them to be neglected when compared to the scales of the flow perturbations. Refer to Kovasznay [28] for further details.

the inlet and exit boundary conditions. The vortical and entropic disturbances are convected with fluid particles and can thus only move downstream, whereas the potential disturbances have either evanescent (exponentially decaying) or propagating (acoustic) behavior. These potential disturbances affect the flow field both in the upstream and downstream directions. The resulting flow field is then a combination of the three basic types of disturbances:

- Pressure disturbances, δP: due to the potential disturbances, $\delta\varphi$;
- Velocity disturbances, δV_x and δV_θ: due to potential, $\delta\varphi$, and vortical, $\delta\omega_{vor}$, disturbances;
- Density disturbances, $\delta\rho$: due to potential, $\delta\varphi$, and entropic, δs, disturbances.

This will be applied in each element (duct, gap or blade row), where we model the mean flow as steady and uniform.

Duct and gap dynamics

The ducts and gaps are modeled as constant radius annuli with steady, uniform, and inviscid flow. The linearized continuity, inviscid axial and tangential momentum, and energy equations are combined into a single ODE for pressure in the axial direction, x. The time derivatives have been eliminated using a Laplace transform while the complex Fourier decomposition (Eqn 2.2) is applied to eliminate the tangential derivatives. Details of this derivation can be found in [10]. The duct and gap flow field perturbations satisfying these

equations then take the form:

$$\frac{\delta P}{P}(x,\theta,s) = \sum_{n=-\infty}^{\infty} \gamma \begin{bmatrix} \Big(r\alpha_n(s)M_x + (\frac{sr}{a} + jnM_\theta)\Big)B_n(s)e^{\alpha_n(s)x} + \\ \Big(r\beta_n(s)M_x + (\frac{sr}{a} + jnM_\theta)\Big)C_n(s)e^{\beta_n(s)x} \end{bmatrix} e^{jn\theta} \tag{2.8}$$

$$\frac{\delta \rho}{\rho}(x,\theta,s) = \sum_{n=-\infty}^{\infty} \begin{bmatrix} \Big(r\alpha_n(s)M_x + (\frac{sr}{a} + jnM_\theta)\Big)B_n(s)e^{\alpha_n(s)x} + \\ \Big(r\beta_n(s)M_x + (\frac{sr}{a} + jnM_\theta)\Big)C_n(s)e^{\beta_n(s)x} + E_n(s)e^{\chi_n(s)x} \end{bmatrix} e^{jn\theta} \tag{2.9}$$

$$\frac{\delta V_x}{a}(x,\theta,s) = \sum_{n=-\infty}^{\infty} \left[-r\alpha_n(s)B_n(s)e^{\alpha_n(s)x} - r\beta_n(s)C_n(s)e^{\beta_n(s)x} + jnM_x D_n(s)e^{\chi_n(s)x}\right] e^{jn\theta} \tag{2.10}$$

$$\frac{\delta V_\theta}{a}(x,\theta,s) = \sum_{n=-\infty}^{\infty} \left[-jnB_n(s)e^{\alpha_n(s)x} - jnC_n(s)e^{\beta_n(s)x} + \left(\frac{sr}{a} + jnM_\theta\right) D_n(s)e^{\chi_n(s)x}\right] e^{jn\theta} \tag{2.11}$$

where:

$$\chi_n(s) = \frac{-\left(\frac{sr}{a} + jnM_\theta\right)}{rM_x} \tag{2.12}$$

$$\alpha_n, \beta_n(s) = \frac{M_x\left(\frac{sr}{a} + jnM_\theta\right) \pm \sqrt{n^2(1 - M_x^2) + \left(\frac{sr}{a} + jnM_\theta\right)^2}}{r(1 - M_x^2)} \tag{2.13}$$

with $\alpha_n(s)$ taking the positive sign.

The coefficients $B_n(s)$ and $C_n(s)$ represent the upstream and downstream potential waves respectively, while $D_n(s)$ is the contribution from the vortical disturbances and $E_n(s)$, from the entropic disturbances.

Blade row dynamics and matching conditions with the ducts/gaps

The blade rows are allowed to support only one-dimensional flow in their relative reference frame by modeling the blade passages as 1-D ducts, as shown in Figure 2-2. The flow inside the blade passages is considered inviscid and can be represented by the linearized continuity, momentum and energy equations in the relative frame. The perturbations then have the

form:

$$\frac{\delta P}{P}(x,\theta,s) = \sum_{n=-\infty}^{\infty} \gamma\left[\tilde{B}_n(s)e^{\tilde{\alpha}_n(s)x} + \tilde{C}_n(s)e^{\tilde{\beta}_n(s)x}\right] e^{jn\theta} \tag{2.14}$$

$$\frac{\delta \rho}{\rho}(x,\theta,s) = \sum_{n=-\infty}^{\infty} \left[\tilde{B}_n(s)e^{\tilde{\alpha}_n(s)x} + \tilde{C}_n(s)e^{\tilde{\beta}_n(s)x} + \tilde{E}_n(s)e^{\tilde{\chi}_n(s)x}\right] e^{jn\theta} \tag{2.15}$$

$$\frac{\delta W}{a}(x,\theta,s) = \sum_{n=-\infty}^{\infty} \left[-\tilde{B}_n(s)e^{\tilde{\alpha}_n(s)x} + \tilde{C}_n(s)e^{\tilde{\beta}_n(s)x}\right] e^{jn\theta} \tag{2.16}$$

where:

$$\tilde{\alpha}_n(s) = \frac{1}{cos\xi}\left(-jn\frac{sin\xi}{r} + \frac{s+jn\Omega}{a-W}\right) \tag{2.17}$$

$$\tilde{\beta}_n(s) = \frac{1}{cos\xi}\left(-jn\frac{sin\xi}{r} - \frac{s+jn\Omega}{a+W}\right) \tag{2.18}$$

$$\tilde{\chi}_n(s) = \frac{1}{cos\xi}\left(-jn\frac{sin\xi}{r} - \frac{s+jn\Omega}{W}\right) \tag{2.19}$$

The performance characteristics of the blade rows are included in the leading edge and trailing edge matching conditions. To relate the perturbations in the blade rows ($\frac{\delta P}{P}$, $\frac{\delta \rho}{\rho}$, $\frac{\delta W}{a}$) to those in the adjacent gaps or ducts ($\frac{\delta P}{P}$, $\frac{\delta \rho}{\rho}$, $\frac{\delta V_x}{a}$, $\frac{\delta V_\theta}{a}$), the following conditions are applied:

- Leading edge matching conditions
  1. Mass conservation;
  2. Relative total temperature conservation[6];
  3. Relative total pressure loss is given by the pressure loss coefficient $\left(\omega_l' = \frac{P'_{t,1}-P'_{t,2}}{P'_{t,1}-P_1}\right)$;
  4. Turning of the flow to follow the stagger angle.
- Trailing edge matching conditions
  1. Mass conservation;
  2. Relative total temperature conservation;
  3. Relative total pressure conservation;

[6]Rothalpy conservation should be applied if there is a change in radius between the upstream gap or duct and the blade row. This also applies at the trailing edge.

4. Turning of the flow at the deviation angle (i.e. exit flow angle).

These matching conditions can be viewed as actuator disks. At the leading edge, turning and pressure loss occurs while at the trailing edge, positive or negative turning can occur depending the deviation. Since the matching conditions include loss and deviation functions, the linearization will make the slopes of these functions appear in the model. The loss coefficient and the deviation of high-speed blade rows can depend on the Reynolds number, the incidence angle and the relative leading edge Mach number. As stated by Kerrebrock [25], for most compressor operating conditions, the Reynolds number is high enough that the cascade performance is insensitive to the actual value and this parameter can be suppressed[7]. Flow angle and Mach number disturbances then lead to perturbations in the loss coefficient and deviation, according the partial derivatives of the loss and deviation functions:

$$\delta\omega_l' = \frac{\partial\omega_l'}{\partial\tan\beta_1}\delta\tan\beta_1 + \frac{\partial\omega_l'}{\partial M_1'}\delta M_1' \tag{2.20}$$

$$\delta\tan\beta_2 = \frac{\partial\tan\beta_2}{\partial\tan\beta_1}\delta\tan\beta_1 + \frac{\partial\tan\beta_2}{\partial M_1'}\delta M_1' \tag{2.21}$$

The partial derivatives ($\frac{\partial\omega_l'}{\partial\tan\beta_1}$, $\frac{\partial\omega_l'}{\partial M_1'}$, $\frac{\partial\tan\beta_2}{\partial\tan\beta_1}$, $\frac{\partial\tan\beta_2}{\partial M_1'}$) are the *blade row performance slopes* relevant for 2-D compressible rotating stall inception modeling[8]. As in the incompressible model, where blade row performance slopes combine to give the overall total-to-static pressure rise slope (Section 2.1), these compressible blade row performance slopes are important factors in the stability of high-speed axial compressors.

Loss and deviation lags

The unsteady response of the total pressure loss and deviation of each blade row are modeled by using first order time lags on these quantities, as with the incompressible model. Applying the Laplace transform to a first order rate equation (2.7) results in a relative total

[7]More precisely, the Reynolds number doesn't affect the loss or deviation of a cascade if it is above a threshold, in the range of about 2×10^5. There is a rapid rise in both deviation and loss below this value [22]

[8]The *tangents* of the flow angles are used since they simplify the formulation of the model. The tangents can be converted to angles using the chain rule for differentiation. Also, the slopes can be expressed as a function of incidence and deviation angle instead of flow angle by simply changing the sign according to the *2DCompSIM* convention (angles are positive in the rotor rotation direction).

pressure drop perturbation across the leading edge actuator disk expressed as:

$$\begin{aligned}\delta P'_{t,1} - \delta P'_{t,2} &= \frac{1}{1+s\tau_p}\Big[(\delta P'_{t,1} - \delta P_1)\omega'_l + (P'_{t,1} - P_1)\delta\omega'_l\Big] \\ &= \frac{1}{1+s\tau_p}\Big[(\delta P'_{t,1} - \delta P_1)\omega'_l + (P'_{t,1} - P_1)\Big(\frac{\partial\omega'_l}{\partial\tan\beta_1}\delta\tan\beta_1 + \frac{\partial\omega'_l}{\partial M'_1}\delta M'_1\Big)\Big]\end{aligned} \tag{2.22}$$

and an exit relative flow angle perturbation expressed as:

$$\delta\tan\beta_2 = \frac{1}{1+s\tau_d}\Big[\frac{\partial\tan\beta_2}{\partial\tan\beta_1}\delta\tan\beta_1 + \frac{\partial\tan\beta_2}{\partial M'_1}\delta M'_1\Big] \tag{2.23}$$

with τ_p and τ_d representing the time constants associated with the viscous pressure loss and deviation respectively.

Inlet and exit boundary conditions

To completely define the problem, four more conditions need to be specified: three inlet boundary conditions and one exit boundary condition. The inlet boundary conditions correspond to uniform incoming flow:

$$\begin{aligned}\delta P_t &= 0 \\ \delta\omega_{vor} &= 0 \quad \text{(all at the inlet plane)} \\ \delta s &= 0\end{aligned} \tag{2.24}$$

The first boundary condition acts as an impedance for the downstream potential mode, while the two others specify the incoming values for the convecting vortical and entropic disturbances. The inlet total pressure perturbation condition is appropriate for the case when the duct is fitted with an ideal bell-mouth of very large area ratio, as shown by Whitehead [48].

The last condition needed to close the problem will be the boundary condition at the end of the exit duct, specifying the impedance for the upstream potential waves. In general, the impedance is determined by modeling the downstream components, as was illustrated in Figure 2-1. The surge modes ($n = 0$) generally see the downstream components differently

from the rotating stall modes ($n \neq 0$) since the area averaged pressure pulsation is zero for the non-zero harmonics. For the surge modes, the combustion chamber is modeled as a plenum and the turbines, as a throttle (see Bonnaure [1] for the details). For the rotating stall modes, the combustor is modeled as a large plenum of uniform pressure. The exit boundary condition is then $\delta P = 0$ at the exit plane[9]. Since compressor testing installations may be terminated by a throttle without a large plenum, the exit boundary condition may be different from $\delta P = 0$. Feulner's version of the model was generalized in order to allow for the exit boundary condition to be changed, as described by Weigl and Fréchette [46].

State-space formulation (*2DCompSIM*)

Feulner [10] combines polynomial transfer functions of the blade row, gap, and duct dynamics with the time lags and boundary conditions into a state-space representation. He also includes sensors and jet injection actuators at the leading edge of each blade row, resulting in the following system, for each harmonic:

$$\begin{aligned} \dot{\vec{x}} &= [A]\,\vec{x} + [B]\,\vec{u} \\ \vec{y} &= [C]\,\vec{x} + [D]\,\vec{u} \end{aligned} \tag{2.25}$$

where $\vec{u}$ are the inputs (jet actuation), $\vec{x}$ are the states of the system and $\vec{y}$ are the sensed outputs ($\frac{\delta P}{P}$, $\frac{\delta V_x}{a}$, ...). Two version of the model were created by Feulner: with and without inter-blade row gaps. The inclusion of gap fluid dynamics allows for circumferential redistribution and decay of evanescent potential disturbances between blade rows. It was shown by Feulner that both formulations are basically equivalent for modes within the frequency range of interest. Since the inclusion of gap dynamics approximately doubles the size of the system and therefore largely increases the computing time for a multistage compressor, the version without gaps will be used throughout this thesis.

The homogeneous system dynamics (without actuation) are represented by the eigenvalues

[9]The exit duct feeding into the combustor can be compared to a flow ejecting into a large plenum. Since the streamlines are generally straight at the exit of the jet, the pressure is uniform across the exit plane. Thus, harmonic pressure disturbances are not likely at the exit ($\delta P_{ex} = 0$ for $n \neq 0$)

and eigenvectors of $[A]$. Each eigenmode (an eigenvalue of $[A]$ and the corresponding eigenvector) has a pre-stall flow field which will grow (or decay) and rotate around the annulus. The entire system 2.25 can be used to simulate the compressor's response to actuation and to design compensators to control the inception of rotating stall.

Non-linear formulation

A non-linear version of this model has also been developed by Hendricks [18]. Essentially the same modeling assumptions are used although the equations are not linearized, but numerically integrated in time. Extra dynamics are also included, such as bleed port Helmholtz response. The advantage of the linearized model (*2DCompSIM*) is mainly the speed, since it executes in seconds rather than in hours for the non-linear simulation. It is therefore useful for sensitivity studies as will be done here.

3D formulation

A linear, three-dimensional formulation very similar to *2DCompSIM* has been developed by Sun [41]. Radial modes are represented by spanwise cosine functions, which are modified to allow for hub and casing impedance-type boundary conditions. The 2D linearized fluid equations used in *2DCompSIM* are generalized to three dimensions and matched across each leading edge and trailing edge. Overall stability equations are formed and solved in a similar fashion as Bonnaure did for the 2D pre-stall modes [1].

2.2.2 Using the compressible model (*2DCompSIM*)

The first step towards using the rotating stall model is to generate the required inputs, consisting of parameters representing both the steady and unsteady operation of the compressor:

- Steady Parameters:
  - mean geometry;
  - mean flow field in each blade row, gap and duct;

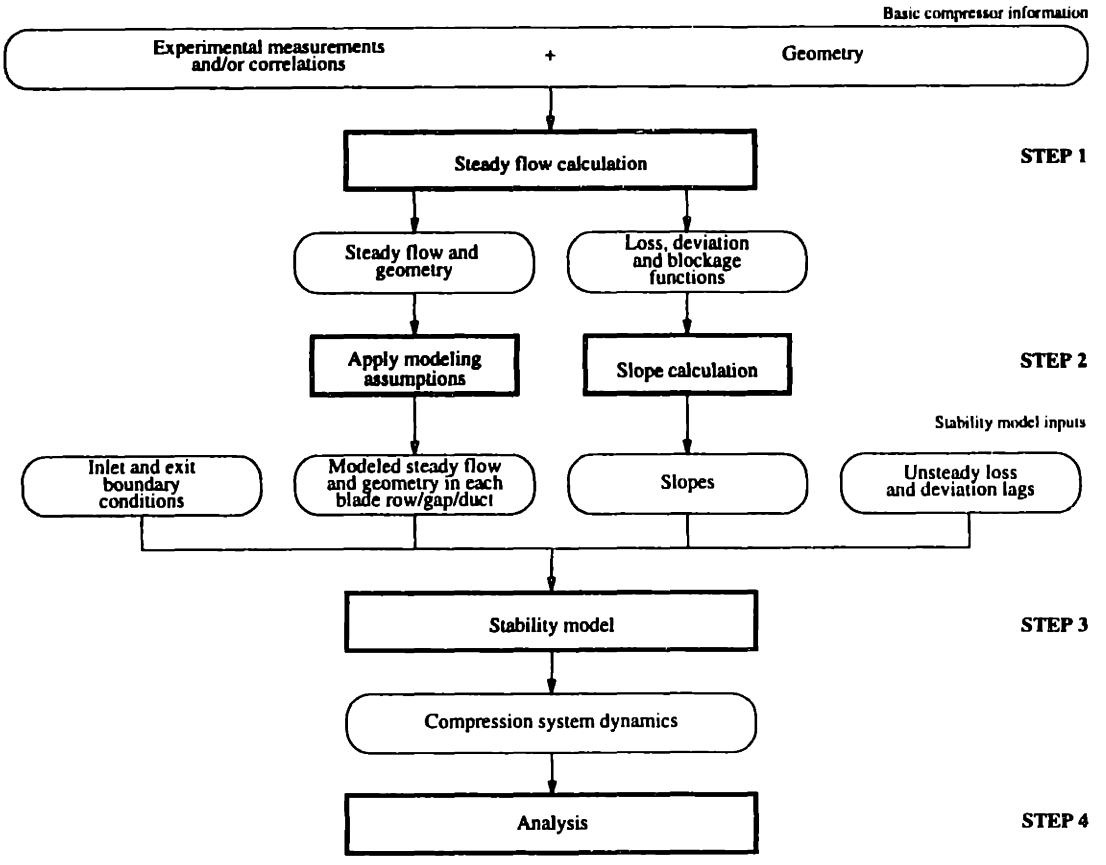

Figure 2-3: Procedure to analyze compression system dynamics.

  - blade row performance slopes (slopes of the loss and deviation characteristics);

- Unsteady parameters:

  - inlet and exit boundary conditions (impedances);
  - time lags for loss and deviation in each blade row.

The basic compressor information available usually consists of the compressor geometry along with some performance characteristics. The performance either comes from correlations (giving losses, deviation and blockage) or experimental measurements (such as total pressure, static pressure and total temperature). From this information, the Steady Parameters are derived.

The overall process of analyzing the compression system dynamics from the basic compressor information is depicted in Figure 2-3. The process can be separated in four steps:

- STEP 1: Calculate the Steady Flow - The steady flow field throughout the compressor can be determined using:
  - mean-line calculation;
  - streamline curvature calculation;
  - computational fluid dynamics;
  - experimental measurements;

  or a combination of the above. The detailed flow fields are reduced to representative circumferentially and radially uniform flow fields. The losses, deviations and blockages are also determined at various operating points.
- STEP 2: Prepare the Stability Model Inputs - The steady flow fields are reduced to mean, uniform flows in each blade row, duct and gap by applying relations consistent with the stability modeling assumptions. A mean geometry is also defined for each blade row, duct and gap. The slopes of the loss and deviation with respect to incidence and relative Mach number ($\frac{\partial \tan\beta_2}{\partial \tan\beta_1}$, $\frac{\partial \tan\beta_2}{\partial M_1'}$, $\frac{\partial \omega_1'}{\partial \tan\beta_1}$, $\frac{\partial \omega_1'}{\partial M_1'}$) are derived from the knowledge of loss, deviation and blockage at different operating points along speedlines. The set of Stability Model Inputs is formed of the modeled flow field and geometry, the slopes, the boundary conditions and the blade row performance lags.
- STEP 3: Run the Stability Model - The state-space representation of the compression system dynamics is created, i.e. matrices $[A]$, $[B]$, $[C]$, and $[D]$ in Eqn 2.25.
- STEP 4: Analyze the Dynamics - Various aspects of the pre-stall dynamics can be analyzed: the stability and rotational frequency of the modes are given by the system's eigenvalues, the pre-stall flow field of each mode is given by the eigenvectors, the dynamic response of the compression system to noise or excitation can be simulated and also, control laws can be designed.

This procedure has been implemented in Matlab as a toolbox: the *2DSIM Toolbox* ("2DSIM" stands for: 2-D Stall/Surge Inception Modeling). It includes a mean line code for the steady flow calculation (STEP 1), routines for the preparation of the stability model inputs (STEP 2), both the compressible and incompressible models (STEP 3) and a suite of functions for analysis of the results (STEP 4). A description of this toolbox is given in Appendix B.

2.3 Main features of the pre-stall dynamics

Throughout the evolution of the rotating stall models, both incompressible and compressible, a main focus has been on developing the equations and using them for active control. This section highlights the main features of the small amplitude pre-stall dynamics as viewed from a system (control) point of view and from a fluid dynamics point of view. These views complement each other in understanding the pre-stall behavior of axial compressors.

2.3.1 From a system dynamics point of view

The dynamic characteristics of small amplitude perturbations in compression systems can be completely defined by a set of eigenmodes (independent modes). Each mode has an eigenvalue, describing the time evolution of the mode; and an eigenvector, describing the structure of the mode. The stability of the system depends on the decay rate (real part) of the least stable eigenvalue: if the real part of one eigenvalue becomes positive, this mode will grow in time and the system will be unstable [10]. The rotation rate (imaginary part of the eigenvalue) specifies the frequency at which the mode will rotate around the annulus.

Each circumferential harmonic, n, gives rise to a set of modes. Since each mode in this set corresponds to a different axial structure, the modes will be identified by the pair $[n, m]$, where n is the circumferential harmonic mode number and m is the axial mode number. The model gives all the axial modes corresponding to one circumferential harmonic in one calculation. The pre-stall behavior is given by the sum of all the modes (circumferential and axial) weighted depending on the initial conditions and their eigenvalue: $a_{n,m}e^{(\sigma_{n,m}-jn\omega_{n,m})t}$.

A plot of the main first, second, and third harmonic eigenvalues as the mass flow through the compressor is decreased at constant rotational speed (root locus) is shown in Figure 2-4 (p. 50). The compressor is an 11 stage, high-speed axial compressor representative of modern core compressors, described in Section 1.3. It will be used as a test case for illustrating the main features of pre-stall dynamics. As the mass flow changes through the compressor, the mean flow field, the blade row performance slopes and the lags change, so

[10] As the amplitude of the perturbations become large, the linearized equations are no longer valid. Modes of the system will interact and a non-linear model is needed to simulate the formation of the rotating stall cell.

the dynamic system (Eqn 2.25) also changes. The eigenvalues are identified by their axial and circumferential harmonic numbers, $[n, m]$. The main points to note are:

- Considering the first harmonic only (Figure 2-4 (a)), the [1,0] mode goes unstable first, followed by the [1,2] and [1,-1] modes as the mass flow is reduced.
- Considering all harmonics, the [1,0] mode goes unstable first, followed by the [2,0], [1,2], [1,-1], and [3,0] modes:

Mode [n,m]	$M_{in,stall}$
$[1,0]$	0.438
$[2,0]$	0.423
$[1,2]$	0.411
$[3,0]$	0.399
$[1,-1]$	0.398

Table 2.1: Neutral stability points of the pre-stall modes for the 11 stage compressor at design speed.

- Higher axial modes are increasingly more stable than the [n,0] modes;
- The largest sensitivity of the stability to change in operating point is seen by the [n,0] modes, and decreases for higher axial modes;
- The frequency (rotation rate) of the modes are less sensitive to the operating point than stability (growth rate).

Even though the [1,0] mode dictates the stability of this system, different operating conditions, or a different compressor may lead one of the compressible modes (such as [1,1]) to become unstable before the incompressible mode ([1,0]), as suggested by Tryfonidis et al.[42].

2.3.2 From a fluid dynamics point of view

Each mode of the system has a pre-stall flow field described by a circumferential and axial structure of $\{\delta P(x,\theta),\ \delta\rho(x,\theta),\ \delta\vec{V}(x,\theta)\}$ or equivalently $\{\delta\varphi(x,\theta),\ \delta\omega_{vor}(x,\theta),\ \delta s(x,\theta)\}$. The circumferential structure is a n-lobed sine wave ($sin(n\theta)$), while the axial structure is

more complex and needs to be solved for by the model. Referring to the formulation of the compressible model in Section 2.2.1, the potential perturbations evolve as $e^{\alpha_n(s)x}$ and $e^{\beta_n(s)x}$ while the convected vortical and entropic modes evolve as $e^{\chi_n(s)x}$. The eigenvalues found by the model are such that once inserted into $\alpha_n(s)$, $\beta_n(s)$ and $\chi_n(s)$, will generate a structure that satisfies the end boundary conditions and the matching conditions between the elements (ducts/gaps and blade rows). For the incompressible model, only one type of axial structure is allowed, reducing the number of axial modes from an infinite number in the compressible case, to a single axial mode. This incompressible mode, that rotates at a fraction of the rotor frequency, will be defined as the zeroth axial mode: $[n, 0]$ for the n^{th} circumferential harmonic. The axial mode number, m, of the other modes increase with eigenvalue frequency, taking the positive or negative sign when the mode travels with or against the rotor respectively. For example, the $[1, 1]$ mode is the first 'compressible' mode traveling in the same direction as the rotor.

The structure of flow perturbations and the phase between each one of them is completely defined by the mode's eigenvector and eigenvalue. The time evolution of these perturbations follow that of the eigenmode, so they all rotate at a frequency ω around the annulus and their amplitude grows or decays at a rate σ. Understanding the pre-stall flow field is important since it will be used in Chapter 3 to analyze the stability of the compression system from an energy point of view.

View of the pre-stall flow field

Various views of the mass flow perturbation are shown in Figures 2-5, 2-6, and 2-7 (p. 51-53) for the 11 stage high-speed compressor modes $[1, 0]$, $[1, 2]$, and $[1, -1]$ respectively. The first plot of each figure is a 3-D view showing the amplitude and phase of the mass flow perturbation in θ and x. The circumferential shape is a simple sine wave, while the axial shape is more complex. The second plot is a top view of the previous 3-D plot; the magnitude of the perturbation is shown by the shading instead of the third dimension. The white lines are contours of zero amplitude (nodal lines), illustrating the swirl in the perturbation structure. The information shown in these 3-D and 2-D plots is represented by the two 1-D plots of the magnitude and phase of the sine wave along the compressor. In these plots, the vertical dotted lines delimit the location of rotors and stators, with the

first blade row starting at $x/r_o = 0$.

[1,0] mode - Figure 2-5 We note that the amplitude of the [1,0] mode mass flow perturbation is *constant* along the compressor. For this reason, it may be referred to as the "incompressible-like" mode, even though it is formed of a non-zero density perturbation. This is the fundamental Moore-Greitzer mode of a compression system.

[1,2] mode - Figure 2-6 The higher frequency modes, such as the [1,2] mode shown, have a more complex axial structure than the incompressible-like mode.

[1,-1] mode - Figure 2-7 Modes rotating against the rotor direction are characterized by an opposite swirl angle in the perturbation mode shape when compared to the positive frequency modes[11].

Potential disturbances

The potential disturbances contribute to δP, $\delta\rho$, and $\delta\vec{V}$ through the $B(s)e^{\alpha_n(s)x}$ and $C(s)e^{\beta_n(s)x}$ terms in Eqns 2.8 to 2.11 (or Eqns 2.14 to 2.16 in the blade rows). The coefficients α_n and β_n therefore describe the structure of the upstream and downstream potential waves respectively. The imaginary part of these coefficients specifies the swirl, while the real part guides the axial growth or decay. The propagating (acoustic) or decaying (evanescent) nature of the potential disturbances is therefore given by the coefficients α_n and β_n. Taking, for example, the upstream potential perturbations at neutral stability, and with no mean swirl, Eqn 2.13 for β_n states that these perturbations will be of decaying nature if $n^2(1-M_x^2) > (\frac{n\omega r}{a})$ or of propagating nature if $n^2(1-M_x^2) < (\frac{n\omega r}{a})$. The rotation rate of the modes therefore dictate their propagating or decaying nature: higher frequency modes will propagate while lower frequency modes will decay. The upstream duct mode shape of higher frequency modes (such as the [1,2] mode) are characterized by an axial wave-like structure, as shown in the magnitude and phase plots of Figure 2-6. This structure results from the superposition of the upstream and downstream traveling potential disturbances.

[11]The sign convention in *2DCompSIM* is positive angles in the rotor direction. Therefore, negative frequency modes rotate against tne rotor direction and positive frequency mode rotate in the rotor direction.

The upstream component originates from the compressor face and travels upstream at a velocity $a - \bar{V}_x$ (speed of sound relative to the mean flow). Part of it is reflected by the inlet boundary condition, creating the downstream potential disturbance in the inlet duct. This disturbance travels downstream at a velocity $a + \bar{V}_x$. The swirl angle of these potential disturbances is a function of the ratio of their tangential and axial velocities $\left(\frac{n\omega r}{a-\bar{V}_x} \text{ and } \frac{n\omega r}{a+\bar{V}_x}\right)$, where the tangential velocity of the potential disturbance is simply the rotation rate of the mode. The swirl angle is therefore greater for the upstream potential disturbance than the downstream one. The sum of two circumferential harmonic structure with different axial swirl angles can be shown mathematically to result in the final magnitude and phase shown in the upstream duct of higher-frequency (propagating) modes (Figure 2-6).

In the incompressible case, the speed of sound goes to infinity (and the Mach number goes to zero), so there is no swirling of the potential field in the ducts or gaps. Furthermore, the pressure perturbation structure decays exponentially upstream and downstream, as shown in Figure 2-8 (p. 54), where the pressure field was calculated from the incompressible equations of Appendix A. The compressor in an actuator disk at $x = 0$, creating a discontinuity of the pressure perturbation magnitude and phase.

Vortical and Entropic disturbances

The vortical disturbances contribute to velocity perturbation ($\delta\vec{V}$, in the ducts/gaps only) through the $D(s)e^{\chi_n(s)x}$ term, while the entropic disturbances create density perturbations ($\delta\rho$) only through the $E(s)e^{\chi_n(s)x}$ term. The structures of both $\delta\omega_{vor}$ and δs are defined by $\chi_n(s)$, which is a convective term. Since the inlet boundary condition prescribes no incoming $\delta\omega_{vor}$ nor δs, the entire upstream duct will be free of vortical and entropic disturbances. The rest of the flow field sees convected perturbations created through the coupling of $\delta\varphi$, $\delta\omega_{vor}$, and δs at the blade row leading and trailing edge matching conditions.

It is instructive to look at the effect of the growth rate (real part of the eigenvalue) on the flow field structure. Figure 2-9 (p. 55) shows the magnitude and phase of the vorticity perturbation along the axis of a low speed compressor (incompressible [1,0] mode) for three values of $\frac{\partial\Psi^{ts}}{\partial\phi}$: stable ($\frac{\partial\Psi^{ts}}{\partial\phi} < 0$), neutrally stable ($\frac{\partial\Psi^{ts}}{\partial\phi} = 0$), and unstable ($\frac{\partial\Psi^{ts}}{\partial\phi} > 0$). These slopes correspond to different operating points along a speedline. The 2-D structure,

(x, θ), can be viewed as a time evolving 1-D process (t, θ). In the stable case for example, the perturbations at the compressor will be damped, so the magnitude of $\delta\omega_{vor}$ created by the compressor will diminish in time. The axial structure of $\delta\omega_{vor}$ in the downstream duct shows a larger $\delta\omega_{vor}$ the further we go downstream. This is so because of the convective nature of these disturbances: the disturbances far downstream have been created earlier, when the production of $\delta\omega_{vor}$ was greater. Figure 2-10 illustrates this argument. The long dashed line represents the convection of $\delta\omega_{vor}$ created at an earlier time $t - 2\Delta t$, while the shorter dashed line is the convection of $\delta\omega_{vor}$ created at $t - \Delta t$. The magnitude of $\delta\omega_{vor}$ decreased during the time Δt (for a stable system), so higher levels of $\delta\omega_{vor}$ have been convected further downstream. We note in Figure 2-9 that the magnitude of $\delta\omega_{vor}$ is constant along the exit duct at neutral stability. Swirling of vortical and entropic disturbances can be explained by similar arguments.

2.3.3 Classification of the modes

The harmonic number, n, defines two main classes of modes: the surge modes ($n = 0$) and the rotating stall modes ($n \neq 0$).

The modes corresponding to a harmonic number, n can be decomposed into subsets, or families of modes. The first distinction is between the pre-stall *fluid dynamic modes* and the *lag modes*. Introducing the first order time lags for loss and deviation increases the order of the system by two times the number of blade rows. The root locus then contains more poles than for a model without lags. The new poles can be classified as *lag modes*.

The lag modes are characterized by strong elements in their eigenvector which correspond to the lag states. Plotting the pre-stall flow field for the lag modes results in non-intuitive structures. Fortunately, since the elements in the eigenvector corresponding to the duct, gap, and blade row fluid states ($B_n(s)$, $C_n(s)$, $D_n(s)$, ...) are small relative to the lag elements, the contribution of these modes to the final flow field ($\frac{\delta P}{P}$, $\frac{\delta \rho}{\rho}$, ...) is minor. Furthermore, the lag modes are usually more damped than the fluid modes.

The fluid modes present themselves as lightly damped poles aligned along the imaginary axis of the root locus plot. The main components of their eigenvector correspond to the duct, gap and blade coefficients ($B_n(s)$, $C_n(s)$, ...). The main fluid mode is the Moore-

Greitzer or [1,0] mode since it is classically the mode that goes unstable first, at least in low speed compressors. In high-speed compressors, the higher frequency modes, such as the [1,1] mode, become as important.

2.3.4 Influence of higher order modeling

In order to assess the effects of adding dynamics to the basic Moore-Greitzer first order model of rotating stall (such as loss and deviation lags, compressibility, radial modes, non-linearities, downstream component dynamics, bleed port Helmholtz response, etc.), we can include them in the simpler model and compare the results between the augmented and simpler model. The effects can be seen at two levels:

1. improvement in the prediction accuracy of the neutral stability point of the Moore-Greitzer mode;
2. introduction of *new* modes that may be less stable than the Moore-Greitzer mode, further reducing the stable operating range of the compressor.

Loss and deviation lags

The effect of the lag dynamics is not to add critical modes, but to affect the stability (and frequency) of the fluid modes that existed without these lags and that are responsible for rotating stall. Lags have been shown to usually stabilize the fluid modes, especially for higher harmonics.

Compressibility

Adding compressibility has a different effect however. It not only modifies the $[1,0]$ mode, but creates new modes (such as the $[1,1]$ mode) that may go unstable first. The $[1,0]$ mode is affected by compressibility through non-uniform axial velocity and density, and also through the existence of density perturbations. These aspects are therefore important for the accuracy of eigenvalue predictions, i.e. the surge margin prediction.

Since the higher frequency modes appear when the flow field is compressible, the other effect

of compressibility is to transform a single mode system (in the incompressible case) into a multi-mode system. These compressible modes were conjectured by Tryfonidis [42] to be important for the inception of rotating stall. The compressible model predicted the $[1,1]$ mode in a 4-stage high-speed compresssor to become unstable at a higher mass flow than the $[1,0]$ mode. The natural frequency of this mode was near rotor frequency. Signal processing of open-loop pressure measurements from that compressor then showed increasing traveling wave energy at rotor frequency as it approached stall. This increase could result from the lightly damped $[1,1]$ mode with a natural frequency near rotor frequency, therefore validating the modeling results. This second effect of compressibility leads to the conclusion that modeling high-speed compressors with incompressible perturbations is inappropriate since we may be leaving out the mode that actually leads to instability. The $[1,0]$ mode is always of great interest however, since it is the first mode to go unstable in many compressors.

The other effects of compressibility are to:

- make the loss and deviation functions of incidence *and* inlet relative Mach number;
- make the importance of each blade row on overall stability a function axial position, as will be shown by the energy-based analysis in the next chapter.

Having described the physical basis for modeling stability in axial compressors and the method to predict pre-stall compression system dynamics, the next chapter will explain compressor stability from an energy-based analysis.

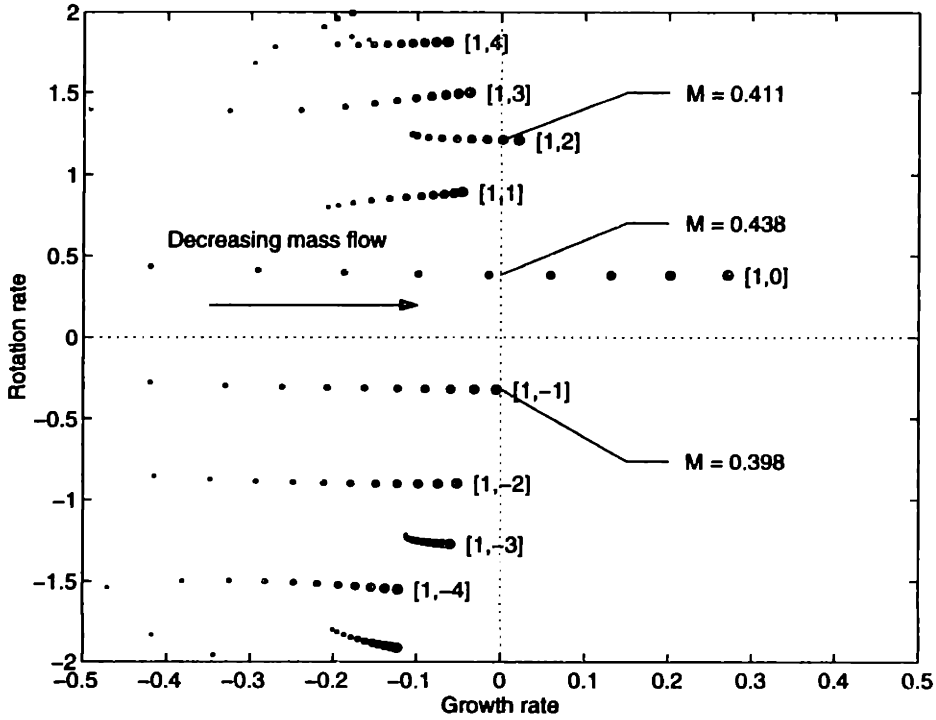

(a) First harmonic ($n = 1$)

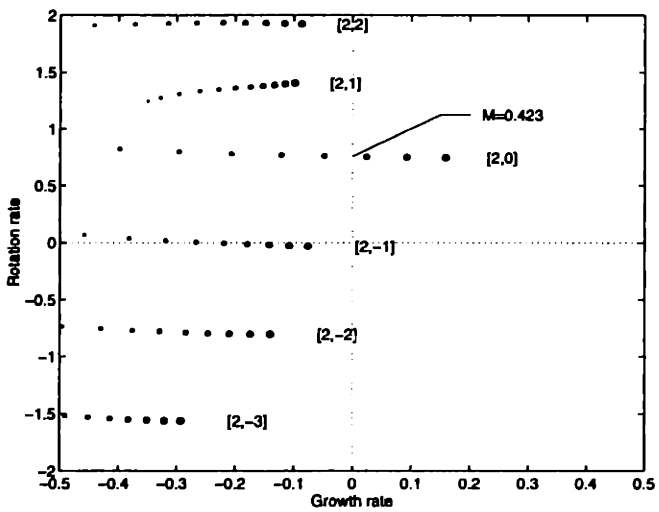

(b) Second harmonic ($n = 2$)

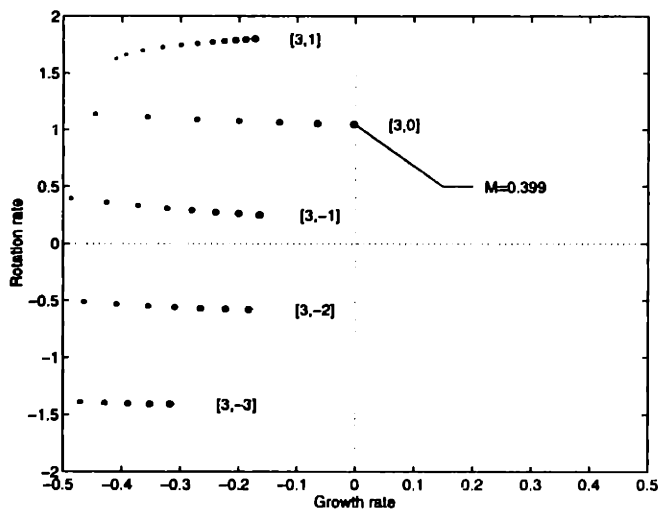

(c) Third harmonic ($n = 3$)

Figure 2-4: Root locus of the first three harmonics for the 11 stage high-speed compressor at design speed. Dot size increases approaching stall, from an inlet Mach number of 0.50 to 0.40 by increments of 0.01;

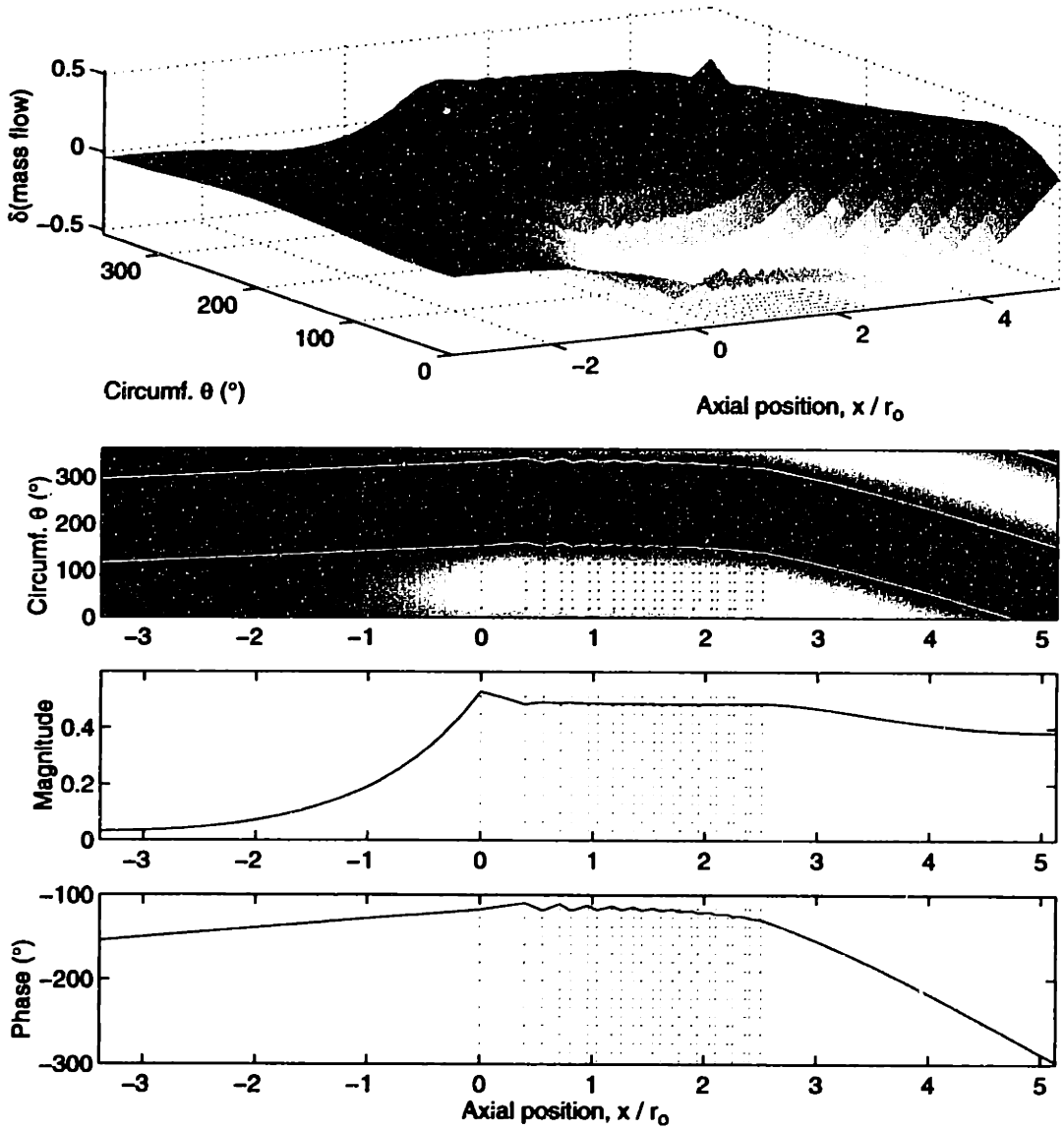

Figure 2-5: Multiple views of the pre-stall mass flow perturbation for the neutrally stable [1,0] mode of the 11 stage high-speed compressor (design speed, inlet Mach number of 0.438). Shading indicates the magnitude of the perturbation. Dotted lines delimit the location of rotors and stators, with the first blade row starting at $x/r_o = 0$.

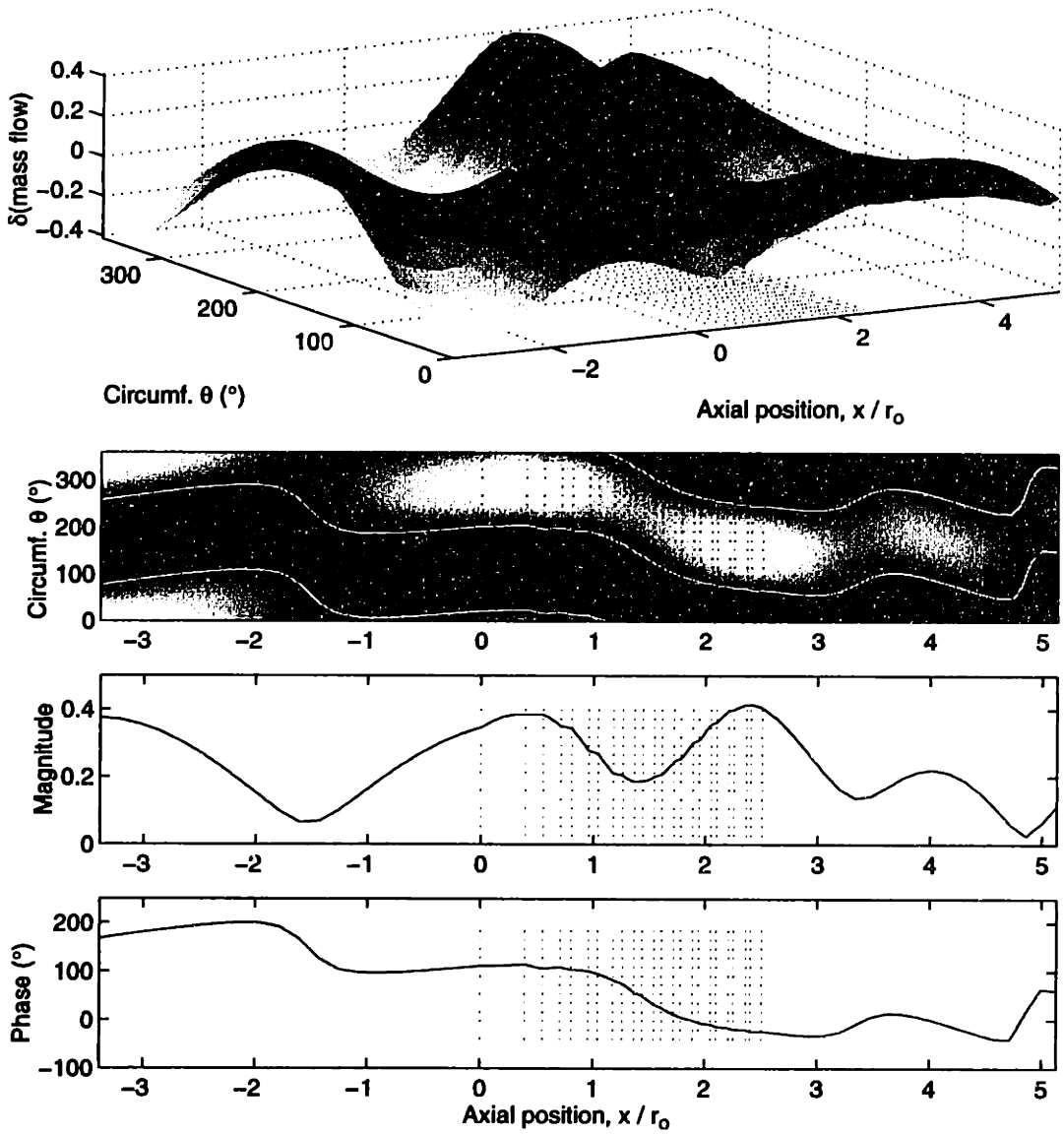

Figure 2-6: Multiple views of the pre-stall mass flow perturbation for the stable [1,2] mode of the 11 stage high-speed compressor (design speed, inlet Mach number of 0.438).

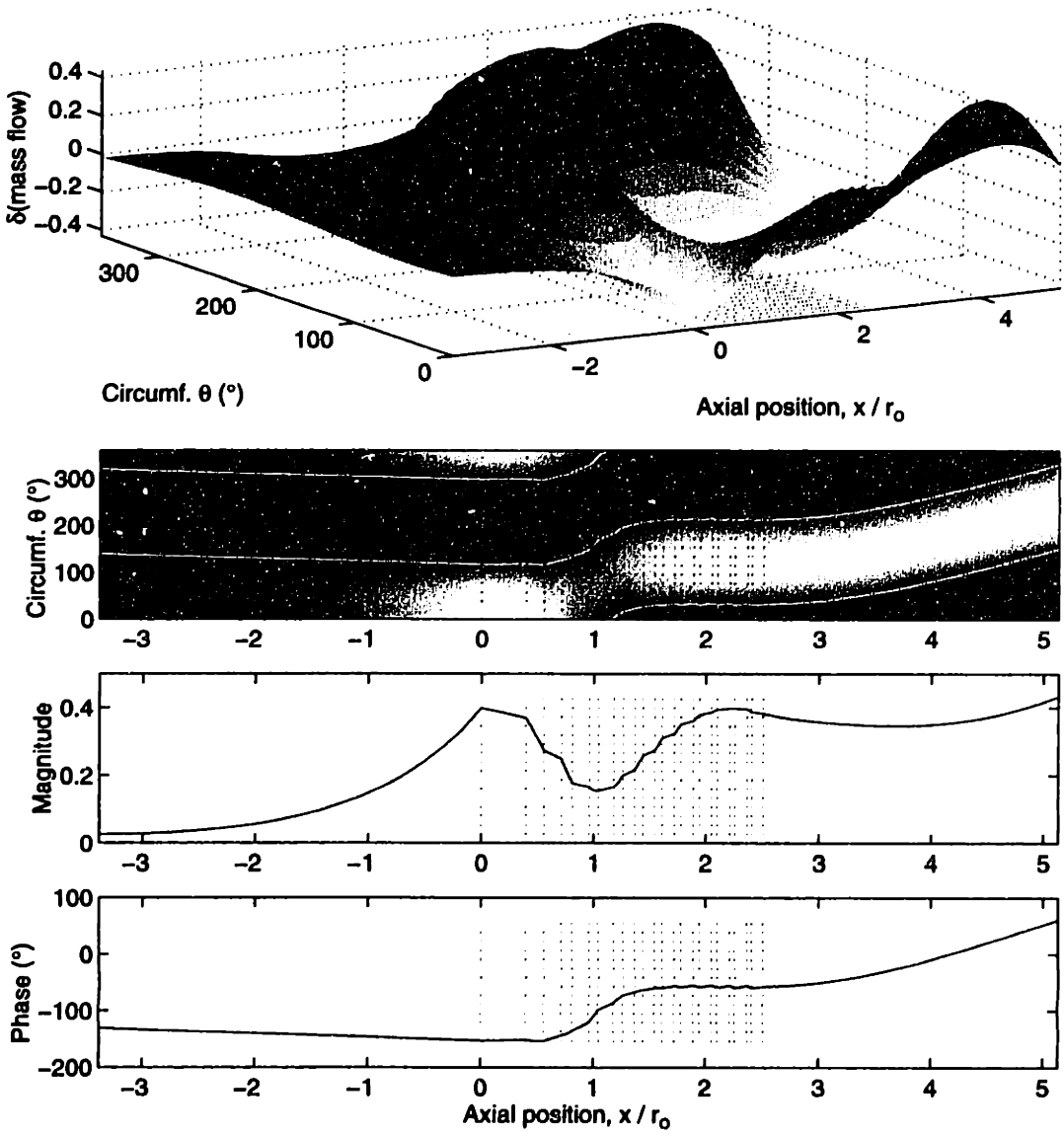

Figure 2-7: Multiple views of the pre-stall mass flow perturbation for the stable [1,-1] mode of the 11 stage high-speed compressor (design speed, inlet Mach number of 0.438).

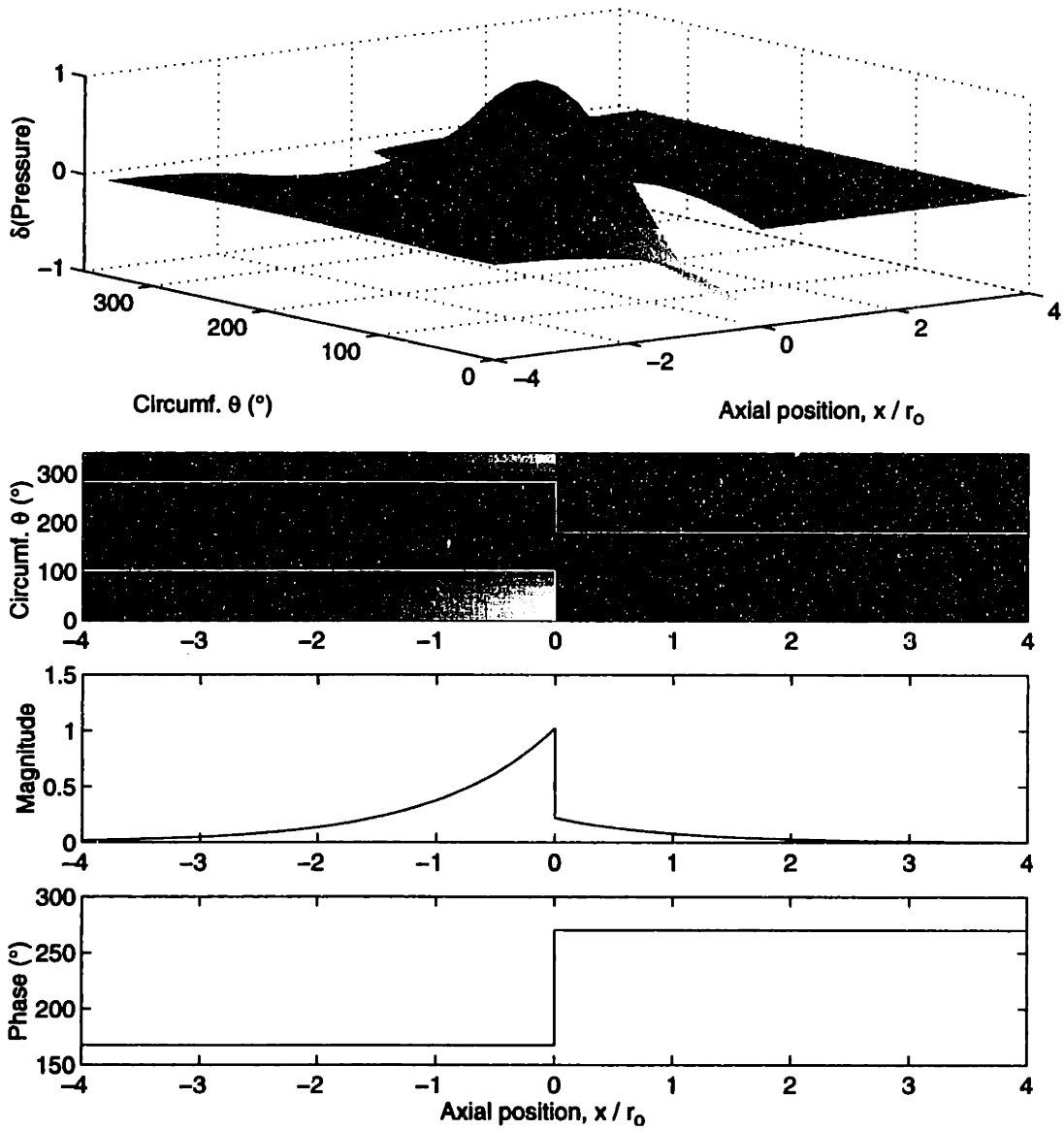

Figure 2-8: Multiple views of the pressure perturbation from the incompressible model: Generic compressor at neutral stability.

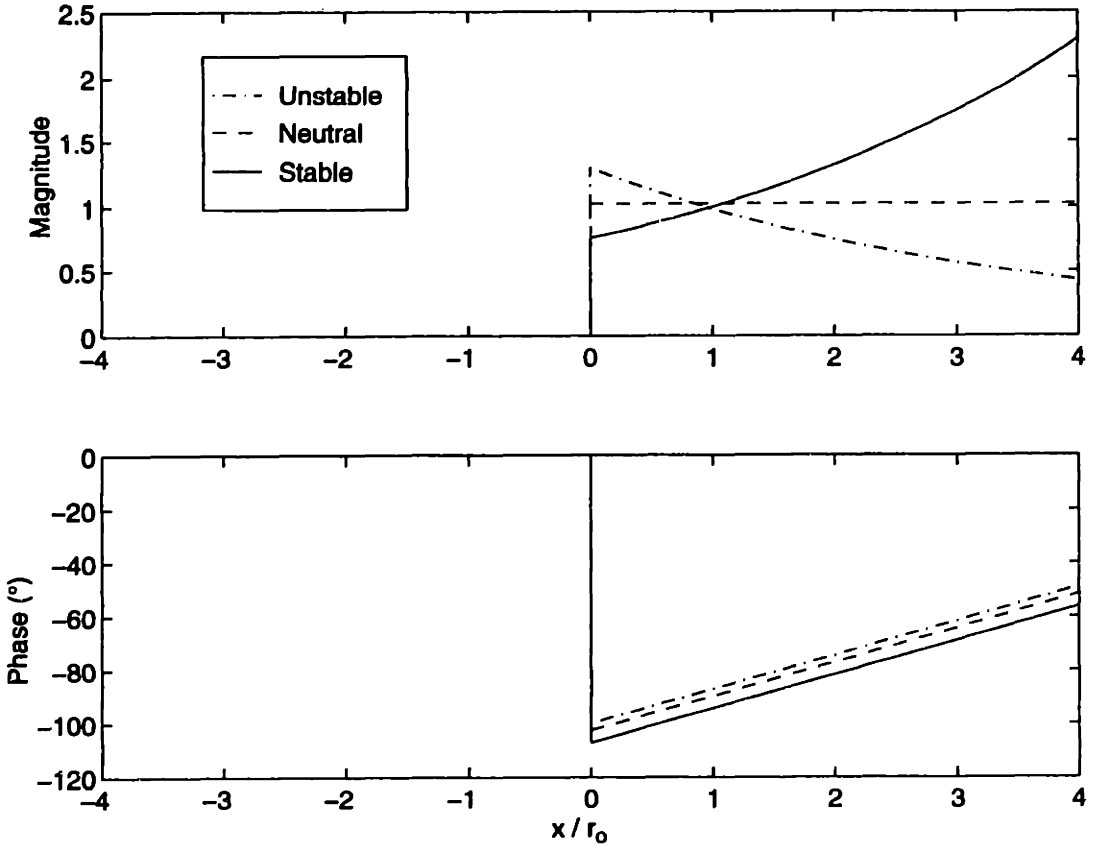

Figure 2-9: Vortical perturbation structure as a function of stability. The three levels of stability correspond to different operating points on a speedline.

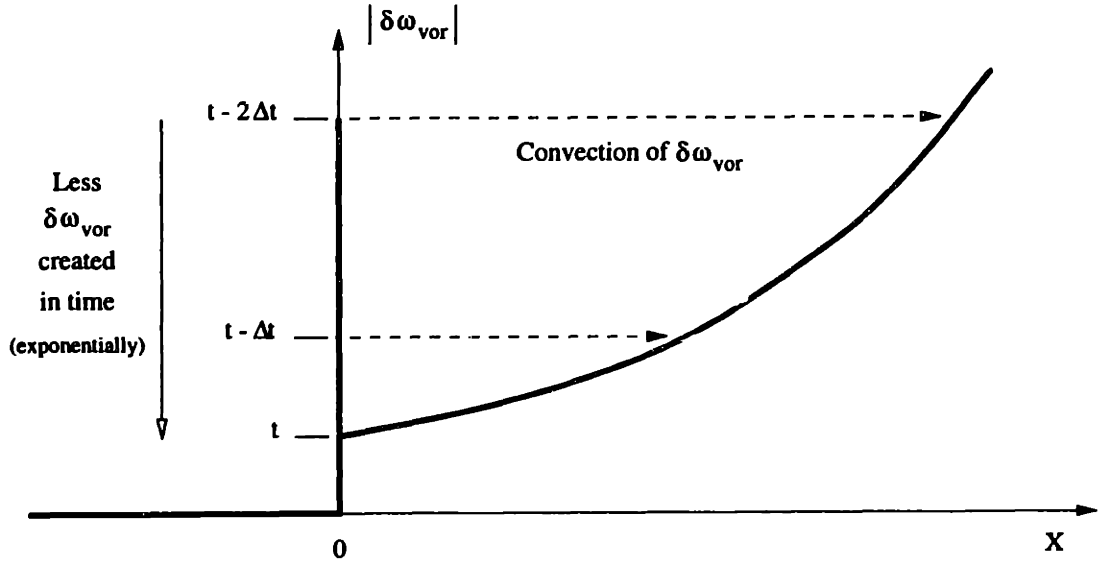

Figure 2-10: Time explanation of the $\delta\omega_{vor}$ structure for a stable mode.

CHAPTER 3

ENERGY-BASED ANALYSIS OF ROTATING STALL INCEPTION

Mechanical systems in general can be analyzed from two points of view:

1. the equations of motion, or
2. conservation of energy.

While both of these approaches are essentially equivalent, one may be more appropriate for solving the system dynamics whereas the other may lead to a better physical understanding of those dynamics. For stability analyses, the equations of motion lead to eigenvalues, and therefore the stability of the system. The energy balance can help build a better physical understanding of pre-stall dynamics: if the total fluid energy in the system increases in time ($\frac{\partial E}{\partial t} > 0$), the oscillations will grow and the system is unstable.

The pre-stall dynamics of high-speed multistage axial compressors are fairly complex since the blade rows do not all operate under the same conditions. A tool helping to understand how the different blade rows contribute to the overall stability would be useful in proposing design modifications to improve the compression system stability. This Chapter proposes an energy-based analysis that can identify the relative importance of the different blade rows and their individual contribution to overall system stability. First, a conservation equation of an energy-type quantity is presented in Section 3.1. This conservation equation will be referred to as the *Disturbance-Energy Corollary*, or simply the Corollary. Then, a method for understanding the role of each blade row on the overall stability of high-speed

compressors is expressed based on an integral form of the Corollary (Section 3.2). As will be shown, the rate of change of disturbance-energy in compressors results from the balance between the disturbance-energy put in the pre-stall flow field by the compressor and that convected in and out through the ducts. Finally, the last section summarizes the chapter and discusses the application of this concept to other types of stability models and flow fields.

3.1 Formulation of the Disturbance-Energy Corollary

The Disturbance-Energy Corollary is first derived from the simplest possible approach. To confirm the direct correspondence between total fluid energy conservation and the Corollary, another approach for developing the Corollary will be reviewed in the following section.

3.1.1 Simple Formulation

A clever approach for deriving the Corollary is to manipulate the linearized mass, momentum and energy equations. This is a classic approach used in analytical acoustics to derive what is referred to as the *Acoustic-Energy Corollary* (first derived by Kirchhoff [26] in 1876). This Corollary is a conservation equation, used to analyze the transport of 'acoustic-energy' emanating from an acoustic 'power source'. Pierce ([39], Chapters 1 and 10) is a good reference for such developments. We will derive a similar Corollary that takes into account a non-zero mean flow (unlike in acoustics), making it applicable to compressors.

The first step is to linearize the fluid dynamic equations to first order perturbations. Each fluid quantity is expressed as $q(\vec{x},t) = \bar{q} + \delta q(\vec{x},t)$, where the mean background flow field will be considered steady ($\frac{\partial \bar{q}}{\partial t} = 0$) and uniform ($\frac{\partial \bar{q}}{\partial x_i} = 0$), as in *2DCompSIM*. The first order linearized Euler equations (mass, inviscid momentum, and non-conductive entropy conservation equations) are then:

$$\frac{\partial \delta\rho}{\partial t} + \bar{\rho}\vec{\nabla}\cdot\delta\vec{V} + \vec{\bar{V}}\cdot\vec{\nabla}\delta\rho = 0 \tag{3.1}$$

$$\bar{\rho}\frac{\partial \delta\vec{V}}{\partial t} + \bar{\rho}(\vec{\bar{V}} \cdot \vec{\nabla})\delta\vec{V} = -\vec{\nabla}\delta P \tag{3.2}$$

$$\frac{\partial \delta s}{\partial t} + \vec{\bar{V}} \cdot \vec{\nabla}\delta s = 0 \tag{3.3}$$

To obtain the Corollary, we first take the dot product of the momentum equation (3.2) with $\delta\vec{V}$. Since $\delta\vec{V} \cdot \frac{\partial}{\partial t}(\delta\vec{V}) = \frac{\partial}{\partial t}\left(\frac{1}{2}\delta V^2\right)$, we obtain:

$$\bar{\rho}\frac{\partial}{\partial t}\left(\frac{1}{2}\delta V^2\right) + \bar{\rho}\,\delta\vec{V} \cdot (\vec{\bar{V}} \cdot \vec{\nabla})\delta\vec{V} = -\delta\vec{V} \cdot \vec{\nabla}\delta P \tag{3.4}$$

We then rewrite the entropy conservation equation (3.3) in terms of δP and $\delta\rho$ instead of δs, using the following thermodynamic relation [39]:

$$\left(\frac{\bar{\rho}\beta\bar{T}}{c_p}\right)\delta s = \frac{1}{\bar{a}^2}\delta P - \delta\rho \tag{3.5}$$

where β is the coefficient of thermal expansion[1] and c_p is the specific heat at constant pressure. The alternate form of Eqn 3.3 is then:

$$\frac{\partial \delta\rho}{\partial t} + \vec{\bar{V}} \cdot \vec{\nabla}\delta\rho = \frac{1}{\bar{a}^2}\left(\frac{\partial \delta P}{\partial t} + \vec{\bar{V}} \cdot \vec{\nabla}\delta P\right) \tag{3.3'}$$

which once subtracted from the linearized mass conservation equation (3.1), results in:

$$\frac{1}{\bar{a}^2}\left(\frac{\partial \delta P}{\partial t} + \vec{\bar{V}} \cdot \vec{\nabla}\delta P\right) + \bar{\rho}\vec{\nabla} \cdot \delta\vec{V} = 0 \tag{3.6}$$

Then, multiplying this equation by $\delta P/\bar{\rho}$ gives:

$$\frac{\partial}{\partial t}\left(\frac{1}{2}\frac{\delta P^2}{\bar{\rho}\bar{a}^2}\right) + \vec{\bar{V}} \cdot \vec{\nabla}\left(\frac{\delta P^2}{2\bar{\rho}\bar{a}^2}\right) + \delta P\vec{\nabla} \cdot \delta\vec{V} = 0 \tag{3.7}$$

since $\delta P\frac{\partial \delta P}{\partial t} = \frac{\partial}{\partial t}\left(\frac{1}{2}\delta P^2\right)$ and $\delta P\vec{\nabla}\delta P = \vec{\nabla}\left(\frac{1}{2}\delta P^2\right)$. Adding this last equation (3.7) with

[1] For an ideal gas, $p = \rho RT$ implies $\beta = 1/T$, so βT can be replaced by 1.

Eqn 3.4, and noting that $\delta P\vec{\nabla}\cdot\delta\vec{V}+\delta\vec{V}\cdot\vec{\nabla}\delta P=\vec{\nabla}\cdot(\delta P\delta\vec{V})$ leads to:

$$\frac{\partial}{\partial t}\left(\frac{1}{2}\bar{\rho}(\delta V)^2+\frac{1}{2}\frac{\delta P^2}{\bar{\rho}\bar{a}^2}\right)+\vec{\nabla}\cdot\left(\delta P\delta\vec{V}\right)+\vec{\bar{V}}\cdot\vec{\nabla}\left(\frac{1}{2}\frac{\delta P^2}{\bar{\rho}\bar{a}^2}\right)+\bar{\rho}\,\delta\vec{V}\cdot(\vec{\bar{V}}\cdot\vec{\nabla})\delta\vec{V}=0 \tag{3.8}$$

Finally, using the vector relation: $\delta\vec{V}\cdot(\vec{\bar{V}}\cdot\vec{\nabla})\delta\vec{V}=\vec{\bar{V}}\cdot\vec{\nabla}\left(\frac{1}{2}\delta V^2\right)$, we can express the previous equation as:

$$\frac{\partial}{\partial t}\left(\frac{1}{2}\bar{\rho}(\delta V)^2+\frac{1}{2}\frac{\delta P^2}{\bar{\rho}\bar{a}^2}\right)+\vec{\nabla}\cdot\left(\delta P\delta\vec{V}\right)+\vec{\nabla}\left(\vec{\bar{V}}\cdot\frac{1}{2}\frac{\delta P^2}{\bar{\rho}\bar{a}^2}\right)+\vec{\nabla}\left(\vec{\bar{V}}\cdot\frac{1}{2}\delta V^2\right)=0 \tag{3.9}$$

The *Disturbance-Energy Corollary* is then:

$$\boxed{\frac{\partial\mathcal{E}}{\partial t}+\vec{\nabla}\cdot(\vec{\mathcal{I}}+\mathcal{E}\vec{\bar{V}})=0} \tag{3.10}$$

with:

$$\vec{\mathcal{I}}=\delta P\delta\vec{V} \tag{3.10a}$$

$$\mathcal{E}=\frac{\delta P^2}{2\bar{\rho}\bar{a}^2}+\frac{\bar{\rho}(\delta V)^2}{2} \tag{3.10b}$$

This relation holds for inviscid, adiabatic, small amplitude disturbances on a uniform steady background flow[2]. The vector $\vec{\mathcal{I}}$ will be referred to as *disturbance-intensity*, and represents the time rate of disturbance-pressure-work per unit area. The quantity $\mathcal{E}$ will be referred to as *disturbance-energy density*, and its terms are respectively the *internal* and *kinetic* disturbance-energy per unit volume. Even though these are not the exact internal and kinetic energies, they are the relevant components of the total fluid energy for the dynamics, i.e. stability. It's to be emphasized that $\mathcal{E}$ is *not* total fluid energy. The term "disturbance-energy" is used because $\mathcal{E}$ is an energy-type quantity relevant to the small amplitude disturbances and not the total energy of the disturbances.

As will be shown in the next section, the Disturbance-Energy Corollary presented above

[2]For a stationary background flow field ($\vec{\bar{V}}=0$), this Corollary is identical to the *Acoustic-Energy Corollary*.

(Eqn 3.10) is an exact representation of the total fluid energy conservation to second order in perturbations.

3.1.2 Energy-based Formulation

The work of Morfey [36] is a comprehensive analysis of the energetics of disturbances in general fluid flows, but the rigorous derivation of a corollary directly from the energy equation is best shown by Myers [37]. His work results in an exact equation governing the transport of energy associated to disturbances in a steady background flow. This relation, shown later, will be referred to as *Myers' Corollary.* It holds for non-uniform steady background flow with viscous, heat conducting, unsteady disturbances. It is derived directly from the energy equation linearized to second order, unlike the development of the Disturbance-Energy Corollary presented above (Eqn 3.10), which resulted from a simple manipulation of the first order linearized fluid equations.

Since the energy basis of corollaries developed by simple equation manipulation is not self-evident and has often been questioned, Myers' approach will be summarized here, and the Disturbance-Energy Corollary will be shown to be equivalent. This will therefore confirm that the simple Disturbance-Energy Corollary in an exact representation of total fluid energy conservation for disturbances in our fluid system.

Myers' Corollary

For the development of Myers' Corollary, each fluid quantity will be represented by the expansion:

$$q(\vec{x},t) = q_o(\vec{x}) + \delta q_1(\vec{x},t) + \delta^2 q_2(\vec{x},t) + \mathcal{O}(\delta^3) \tag{3.11}$$

in which δ is a small parameter and q_i's are of order unity. Relating this to the nomenclature in the rest of this thesis: q_o is the mean background flow ($\bar{q}$); δq_1 is the first order perturbation (δq); and $\delta^2 q_2$ is a perturbation of an order less than δq_1. Since energy is formed by the multiplication of flow quantities (such as $V^2/2$ for kinetic energy), it is intrinsically a second order quantity. The expression of energy to second order contains first order squared

terms ($V_1^2/2$) and zeroth times second order terms ($V_0 V_2$):

$$\begin{aligned}\frac{V^2}{2} &= \frac{1}{2}(V_0 + \delta V_1 + \delta^2 V_2 + \mathcal{O}(\delta^3))^2 \\ &= \frac{V_o^2}{2} + \delta\left(V_o V_1\right) + \delta^2\left(\frac{V_1^2}{2} + V_0 V_2\right) + \mathcal{O}(\delta^3)\end{aligned}$$

Therefore, the second order perturbations need to be calculated in order to exactly determine the total fluid energy. Since the linearized stability models (Moore-Greitzer, *2DCompSIM*) only calculate the first order perturbations (δq_1), we cannot determine the second order energy from them. However, Myers presents a *second order* conservation equation based on total fluid energy conservation containing only *first order* perturbation quantities. The main steps to develop Myers' Corollary are summarized here, simplified for inviscid, non-conducting flow.

Expansion 3.11 is substituted for each fluid quantity in the energy equation. Since the energy equation must be satisfied independently for each order of magnitude, we obtain a set of three energy equations: zeroth order (mean), first order (δ), and second order(δ^2) by combining the terms of the energy equation of each order together.

The same type of expansion is applied to the mass, momentum, and entropy conservation equations[3]. These relations are substituted into the energy equations for each order. The zeroth and first order energy equations reduce to $0 = 0$, but the second order energy equation leads to Myers' Corollary:

$$\frac{\partial E_2}{\partial t} + \vec{\nabla} \cdot \vec{W}_2 = -D_2 \tag{3.12}$$

with, for inviscid and adiabatic flow and no body forces:

$$E_2 = \frac{P_1^2}{2\rho_0 a_0^2} + \frac{\rho_0 V_1^2}{2} + \rho_1 \vec{V}_0 \cdot \vec{V}_1 + \frac{\rho_0 T_0 s_1^2}{2c_{p_0}} \tag{3.12a}$$

$$\vec{W}_2 = \vec{m}_1(h_{t,1} - T_0 s_1) + \vec{m}_0 T_1 s_1 \tag{3.12b}$$

$$D_2 = -\rho_0 \vec{V}_0 \cdot (\vec{\omega}_1 \times \vec{V}_1) - \rho_1 \vec{V}_1 \cdot (\vec{\omega}_0 \times \vec{V}_0) + s_1 \vec{m}_1 \cdot \vec{\nabla} T_0 - s_1 \vec{m}_0 \cdot \vec{\nabla} T_1 \tag{3.12c}$$

[3]The entropy conservation equation is analogue to the energy conservation equation. It doesn't add any new information, but it is useful in the development of the corollary.

where mass flux is $\vec{m} = \rho\vec{V}$, vorticity is $\vec{\omega} = \vec{\nabla} \times \vec{V}$, and total enthalpy is $h_t = h + \frac{V^2}{2}$. The E_2, $\vec{W}_2$, and D_2 quantities represent respectively Myers' disturbance-energy *density*, *flux vector*, and *diffusion* (per unit volume). Once again, this disturbance energy is not total fluid energy, but a similar quadratic quantity (relevant to the flow dynamics) that is conserved following Eqn 3.12. Comparing Myers' Corollary to that developed in Section 3.1.1, we notice similarities, but Myers' Corollary contains many more terms. In particular, Myers' Corollary has a diffusion-type term of the right hand side of Eqn 3.12. Such a term makes the relation difficult to use and understand. Furthermore, the terms composing Myers' disturbance-energy, E_2, cannot all be identified as terms forming the total fluid energy, leading his corollary to be more of a numerical tool than one for understanding the stability of disturbances in fluid systems. The Disturbance-Energy Corollary (Eqn 3.10) is of far greater simplicity and leads itself more readily to numerical, analytical, and possibly experimental use for understanding stability in complex fluid systems.

The Disturbance-Energy Corollary will now be shown to exactly represent the transport of second order total fluid energy by deriving it from Myers' Corollary.

Disturbance-Energy Corollary from Myers' Corollary

The transformation of Myers' Corollary into Eqn 3.10 can be done in three main steps; each step consists of replacing a few terms in Myers' Corollary by an equivalent expression. Before doing so, let's express the first term in $\vec{W}_2$ (Eqn 3.12*b*) as a function of δP and $\delta\rho$. From the definition of stagnation enthalpy, $\vec{W}_2$ can be expressed as:

$$\vec{W}_2 = \rho_0\vec{V}_1(\vec{V}_0 \cdot \vec{V}_1) + \rho_0\vec{V}_1(\vec{V}_0 \cdot \vec{V}_1) + P_1\vec{V}_1 + \frac{\rho_1}{\rho_0}P_1\vec{V}_0 + \vec{m}_0 T_1 s_1 \tag{3.12b'}$$

1 The first step is to substitute the entropy terms in Eqns 3.12*a*, *b'*, and *c*. Using the thermodynamic relations given by Eqn 3.5 and the following:

$$c_{p_0}\delta T = \bar{T}\delta s + \frac{\beta\bar{T}}{\bar{\rho}}\delta P \tag{3.13}$$

along with the entropy equation 3.3, we can be express the entropy terms as:

$$\frac{\partial}{\partial t}\left(\frac{\rho_0 T_0 s_1^2}{2Cp_0}\right) + \vec{\nabla}\cdot(\vec{m}_0 T_1 s_1) - s_1 \vec{m}_0 \cdot \vec{\nabla} T_1 = \vec{\nabla}\cdot\left(\vec{V}_0 \frac{P_1^2}{2\rho_0 a_0^2}\right) - \frac{P_1}{\rho_0}\vec{V}_0 \cdot \vec{\nabla}\rho_1 \tag{3.14}$$

where the background flow was considered uniform.

2 This second step will eliminate the vortical terms of D_2 using vector identities. The gradient of the first two terms in $3.12b'$ and the vortical terms of D_2 can be expressed, for a uniform background flow, as:

$$\begin{aligned}\vec{\nabla}\cdot\Big(\rho_0(\vec{V}_0\cdot\vec{V}_1)\vec{V}_1 + \rho_1(\vec{V}_0\cdot\vec{V}_1)\vec{V}_0\Big) - \rho_0\vec{V}_0\cdot(\vec{\omega}_1\times\vec{V}_1) - \rho_1\vec{V}_1\cdot(\vec{\omega}_0\times\vec{V}_0)\\ = \vec{\nabla}\cdot\left(\vec{V}_0\frac{\rho_0 V_1^2}{2}\right) + \rho_0(\vec{V}_0\cdot\vec{V}_1)\vec{\nabla}\cdot\vec{V}_1 + (\vec{V}_0\cdot\vec{V}_1)\vec{V}_0\cdot\vec{\nabla}\rho_1 + \rho_1\vec{V}_0\cdot(\vec{V}_0\cdot\vec{\nabla})\vec{V}_1\end{aligned} \tag{3.15}$$

where we have used the following vector identities:

$$\vec{\nabla}\left(\frac{V_1^2}{2}\right) = (\vec{V}_1\cdot\vec{\nabla})\vec{V}_1 + \vec{V}_1\times(\vec{\nabla}\times\vec{V}_1) \tag{3.16}$$

$$\vec{\nabla}\left(\vec{V}_0\cdot\vec{V}_1\right) = (\vec{V}_0\cdot\vec{\nabla})\vec{V}_1 + (\vec{V}_1\cdot\vec{\nabla})\vec{V}_0 + \vec{V}_0\times(\vec{\nabla}\times\vec{V}_1) + \vec{V}_1\times(\vec{\nabla}\times\vec{V}_0) \tag{3.17}$$

3 The third term of E_2 along with the third term of W_2 in Eqn $3.12b'$ will be expanded and reformulated using the linearized continuity and momentum equations. Multiplying Eqn 3.1 by $(\vec{V}_0\cdot\vec{V}_1)$ and taking the dot product of Eqn 3.2 with $\rho_1\vec{V}_0$ leads to the following reformulation:

$$\begin{aligned}\frac{\partial}{\partial t}(\rho_1(\vec{V}_0\cdot\vec{V}_1)) + \vec{\nabla}\cdot\Big(p_1\vec{V}_1\Big)\\ = -\rho_0(\vec{V}_0\cdot\vec{V}_1)\vec{\nabla}\cdot\vec{V}_1 - (\vec{V}_0\cdot\vec{V}_1)\vec{V}_0\cdot\vec{\nabla}\rho_1 - \rho_1\vec{V}_0\cdot(\vec{V}_0\cdot\vec{\nabla})\vec{V}_1 + \frac{P_1}{\rho_0}\vec{V}_0\cdot\vec{\nabla}\rho_1\end{aligned} \tag{3.18}$$

Comparing the right hand side terms of this last equation (3.18) to those of Eqns 3.14 and 3.15, we notice that they practically all vanish, leaving only the divergence terms in 3.14 and 3.15. Replacing these equivalent expressions into Myers' Corollary (Eqns $3.12a$, b', c)

leads to:

$$\frac{\partial}{\partial t}\left(\frac{P_1^2}{2\rho_0 a_0^2}+\frac{\rho_0 V_1^2}{2}\right)+\vec{\nabla}\left(P_1\vec{V}_1+\vec{V}_0\frac{P_1^2}{2\rho_0 a_0^2}+\vec{V}_0\frac{\rho_0 V_1^2}{2}\right)=0 \tag{3.19}$$

This is nothing else than the Disturbance-Energy Corollary derived in Section 3.1.1! This simple Corollary has therefore been proven to exactly represent the transport of total fluid energy associated with disturbances in a steady, uniform background flow. Although the flow must be isentropic (inviscid and non-conducting) for the Disturbance-Energy Corollary to be valid, vortical and entropic disturbances *can* be convected. In other words, the steady flow field must be irrotational and homentropic (uniform entropy), but not the perturbations. Since this is how the flows in the gaps and ducts are represented in the stability models, the Disturbance-Energy Corollary is an exact expression for the transport of energy associated to the pre-stall flow field predicted by these models. As the complexity of the stability models increases, so will the corresponding disturbance-energy corollary. The form developed in Section 3.1.1 is however exact when applied to the Moore-Greitzer model or to *2DCompSIM*. Now that the Corollary has been justified, its use for the analysis of compressor stability will be presented in the next section.

3.2 Application to rotating stall inception

Since the Corollary derived previously describes the transport of energy associated with disturbances without the presence of blade rows, an extra step is necessary in order to apply it to compressor pre-stall flow fields, as will be shown in the following section.

3.2.1 Integral form of the Corollary

The interpretation of the Disturbance-Energy Corollary (Eqn 3.10) as a conservation law follows if we integrate it over some fixed control volume, $\mathcal{V}$. Expressing the volume integral of $\vec{\nabla} \cdot \left(\vec{\mathcal{I}} + \mathcal{E}\vec{V}\right)$ as a surface integral by means of Gauss' theorem gives:

$$\frac{\partial}{\partial t} \iiint_{\mathcal{V}} \mathcal{E} d\mathcal{V} + \iint_{\mathcal{S}} (\vec{\mathcal{I}} + \mathcal{E}\vec{V}) \cdot \hat{n}\, d\mathcal{A} = 0$$

$$\frac{\partial}{\partial t} \iiint_{\mathcal{V}} \left(\frac{\delta P^2}{2\bar{\rho}\bar{a}^2} + \frac{\bar{\rho}(\delta V)^2}{2} \right) d\mathcal{V} + \iint_{\mathcal{S}} \left(\delta P \delta \vec{V} + \left(\frac{\delta P^2}{2\bar{\rho}\bar{a}^2} + \frac{\bar{\rho}(\delta V)^2}{2} \right) \vec{\bar{V}} \right) \cdot \hat{n}\, d\mathcal{A} = 0 \tag{3.20}$$

where $\hat{n}$ is the unit normal vector pointing out of the surface $\mathcal{S}$ enclosing $\mathcal{V}$. We note a resemblance to the control volume equation for total fluid energy:

$$\frac{\partial}{\partial t} \iiint_{\mathcal{V}} \left(e + \frac{\rho V^2}{2} \right) d\mathcal{V} + \iint_{\mathcal{S}} \left(\frac{P}{\rho} + e + \frac{\rho V^2}{2} \right) (\vec{V} \cdot \hat{n})\, d\mathcal{A} = \dot{Q} - \dot{W}; \tag{3.21}$$

where e is internal energy, $\dot{Q}$ is rate of heat transfer to the fluid and $-\dot{W}$ the rate of shaft and viscous work done on the fluid. Of main interest is the flux quantity inside the surface integral. For total fluid energy, this integral is composed of pressure work done by the fluid on its surroundings, and convection of internal and kinetic energy through the surface. This adds up to the flux of total (or stagnation) enthalpy. Similarly for Eqn 3.20, the surface integral is the sum of the pressure work done by the pressure perturbations on the surrounding disturbances, and convection of internal and kinetic disturbance-energy by the mean flow. This sum could therefore be referred to as *stagnation disturbance-enthalpy flux*, $\mathcal{F}$.

If the volume is chosen to cover the entire annulus, extending from one axial position to

another within a duct (or gap), the corollary's integral is simply expressed as:

$$\boxed{\frac{\partial}{\partial t}\iiint_{\mathcal{V}} \mathcal{E}\, d\mathcal{V} + \mathcal{F}_{out} - \mathcal{F}_{in} = 0} \tag{3.22}$$

where $\mathcal{F}$ is the stagnation disturbance-enthalpy flux at a specific axial location of annulus area A:

$$\begin{aligned}\mathcal{F} &= \iint_A \left(\delta P \delta \vec{V} + \left(\frac{\delta P^2}{2\bar{\rho}\bar{a}^2} + \frac{\bar{\rho}(\delta V)^2}{2}\right)\vec{\bar{V}}\right)\cdot \hat{n}\, dA \\ &= \iint_A \left(\delta P \delta V_x + \left(\frac{\delta P^2}{2\bar{\rho}\bar{a}^2} + \frac{\bar{\rho}(\delta V)^2}{2}\right)\bar{V}_x\right) dA\end{aligned} \tag{3.23}$$

Relation 3.22 therefore states that the rate of change of disturbance-energy within the volume results from the net flux of stagnation disturbance-enthalpy through its surface: $\mathcal{F}_{out} - \mathcal{F}_{in}$.

Although the flux $\mathcal{F}$ is the quantity of main interest, it leads to the definition of an interesting new quantity: *stagnation (or total) disturbance-enthalpy, f*. In order the express the flux $\mathcal{F}$ as stagnation disturbance-enthalpy convected by the mean flow, we will define f as:

$$f = \frac{\delta P}{\bar{\rho}}\frac{(\delta\vec{V}\cdot\vec{\bar{V}})}{\bar{V}^2} + \frac{\delta P^2}{2\bar{\rho}\bar{a}^2} + \frac{\bar{\rho}(\delta V)^2}{2} \tag{3.24}$$

Defining its area average as:

$$\langle f\rangle = \frac{1}{A}\iint_A \left(\frac{\delta P}{\bar{\rho}}\frac{(\delta\vec{V}\cdot\vec{\bar{V}})}{\bar{V}^2} + \frac{\delta P^2}{2\bar{\rho}\bar{a}^2} + \frac{\bar{\rho}(\delta V)^2}{2}\right) dA \tag{3.25}$$

we can then express the flux of stagnation disturbance-enthalpy, $\mathcal{F}$, as:

$$\mathcal{F} = \langle f\rangle\, \dot{m} \tag{3.26}$$

A major difference between enthalpy and disturbance-enthalpy is the pressure work term. Since this term in $\mathcal{F}$ is not convected by the mean velocity, but rather follows the sign of the velocity perturbation, it may be negative when expressed as in Eqn 3.24. The flux $\mathcal{F}$ is therefore not necessarily positive in the direction of mean flow, as is the case for the usual

stagnation enthalpy flux. This difference arises since potential disturbances can propagate upstream and therefore so can the disturbance-energy associated with these perturbations.

3.2.2 Stagnation disturbance-enthalpy source

Although the Disturbance-Energy Corollary adds nothing beyond what is already contained in the fundamental fluid dynamic equations, its existence enables the description of *disturbance-energy sources*. If an element, such as a blade row, is included in the flow field, the integral relation 3.22 does not hold, so instead we write:

$$\boxed{\frac{\partial}{\partial t}\iiint_{\mathcal{V}} \mathcal{E}\, d\mathcal{V} + \mathcal{F}_{out} - \mathcal{F}_{in} = \mathcal{P}} \tag{3.27}$$

where $\mathcal{P}$ is the disturbance-power of the element. This power source is analogous to $\dot{Q} - \dot{W}$ in the energy equation (3.21). The rotors and stators can therefore be considered as sources of stagnation disturbance-enthalpy of power $\mathcal{P}$. This power can either be positive or negative depending on whether the blade row is putting energy into the perturbations or dissipating it. Integrating the Corollary over the entire compressor flow field (inlet duct, compressor and exit duct) leads to the overall system stability:

$$\frac{\partial}{\partial t}\iiint_{\mathcal{V}_{comp}} \mathcal{E}\, d\mathcal{V} = (\mathcal{F}_{inlet} - \mathcal{F}_{exit}) + \sum_{all\ rows} \mathcal{P} \tag{3.28}$$

This expression states that the stability depends on the balance between the net flux of stagnation disturbance-enthalpy and the total disturbance-power of all the blade rows. This concept of disturbance-power is very similar to acoustic power. Therefore, a stator can produce disturbance-energy just as it can radiate noise.

Although we have no closed form expression for the disturbance-power at this point, it can be evaluated using the Corollary's integral and knowledge of the pre-stall flow field. To evaluate the disturbance-power of the k^{th} blade row, we apply the control volume across it, following these steps:

1. Determine the disturbance flow field ($\delta P(\vec{x},t)$, $\delta \vec{V}(\vec{x},t)$), using *2DCompSIM* or another compressor stability model;

2. Calculate the time derivative of the disturbance-energy density terms and integrate them over the blade row;

3. Calculate the fluxes, $\mathcal{F}$, at the leading and trailing edge;

4. The blade row's source power is then given by:

$$\mathcal{P}_k = \iiint_{\mathcal{V}_{row}} \frac{\partial \mathcal{E}}{\partial t} d\mathcal{V} + \mathcal{F}_2 - \mathcal{F}_1 \tag{3.29}$$

At neutral stability, the time derivative term is zero so the source power is simply the difference in fluxes.

The numerical evaluation of the disturbance-energy terms is fairly simple because they are all products of two first order perturbations. Since the circumferential shape of the perturbations is a sinusoid, the integral of their product over the annulus reduces to, using trigonometric identities, the product of their amplitudes and the cosine of their phase difference. For example, the pressure work term in $\mathcal{F}$ is evaluated as:

$$\iint_{\mathcal{A}} \left(\delta P \delta \vec{V}\right) \cdot \hat{n} \, d\mathcal{A} = A \times |\delta P||\delta V_x| cos(\angle \delta P - \angle \delta V_x) \tag{3.30}$$

For harmonic perturbations, the flux $\mathcal{F}$ is therefore proportional to the magnitude of each perturbation and the cosine of their relative phase. The ability of a blade row to change the phase between static pressure and axial velocity perturbations is thus representative of its power. The flux $\mathcal{F}$ due to the internal and kinetic energy terms however, is only proportional to the magnitude of the perturbations since it results from first order perturbations squared: δP^2 and δV^2. The power of a blade row is therefore proportional to the increase in kinetic and internal disturbance-energy across it.

This energy analysis is applied to each mode individually since they are uncoupled and evolve independently. The stability of one mode is not affected by the others, which is also true for the disturbance-energy balance. A more detailed description of blade row disturbance-power will be given is Section 3.3. Beforehand, applications of the Corollary will be discussed for incompressible and compressible flow fields.

3.2.3 Incompressible flow field

To illustrate the application of this approach, it will first be applied to an incompressible pre-stall flow field, derived from the Moore-Greitzer model. For incompressible flow, the Corollary drops the internal energy term, leaving the disturbance-energy defined only as kinetic disturbance-energy. The incompressible form of the Corollary is then:

$$\frac{\partial \mathcal{E}_{inc}}{\partial t} + \vec{\nabla} \cdot \left(\vec{\mathcal{I}} + \mathcal{E}_{inc} \vec{V} \right) = 0 \tag{3.31}$$

$$\mathcal{E}_{inc} = \rho \frac{\vec{V}_1^2}{2} \tag{3.31a}$$

$$\vec{\mathcal{I}} = \delta P \delta \vec{V} \tag{3.31b}$$

and the flux $\mathcal{F}_{inc}$ follows to be :

$$\mathcal{F}_{inc} = \iint_A \left(\delta P \delta V_x + \frac{\bar{\rho}(\delta V)^2}{2} \bar{V}_x \right) dA \tag{3.32}$$

This flux quantity was identified by Gysling ([15], Appendix D) as a governing parameter in stall inception. He also applied the control volume approach, stating in our terms, that the production rate of disturbance-energy by the compressor is equal to the net flow rate of disturbance-energy in and out the ducts at neutral stability. Gysling then goes further and analytically proves that this disturbance-energy balance at neutral stability is exactly equivalent to the neutral stability criteria resulting from the Moore-Greitzer model: $\frac{\partial \Psi^{ts}}{\partial \phi} = 0$.

An example of the relevant disturbance-energy terms is plotted in Figure 3-1 for the incompressible Moore-Greitzer mode at three levels of stability (unstable: $\frac{\partial \Psi^{ts}}{\partial \phi} > 0$, neutral: $\frac{\partial \Psi^{ts}}{\partial \phi} = 0$, stable: $\frac{\partial \Psi^{ts}}{\partial \phi} < 0$). The compressor is an actuator disk located at $x = 0$ and along its axis are plotted the flux $\mathcal{F}_{inc}$ in part (a) of the figure. The jump in $\mathcal{F}_{inc}$ across the compressor is a measure of the disturbance-energy created by the compressor. The flux at the exit is largest at stable operation because the amplitudes of the flow perturbations are larger downstream for a stable mode (see Figure 2-10).

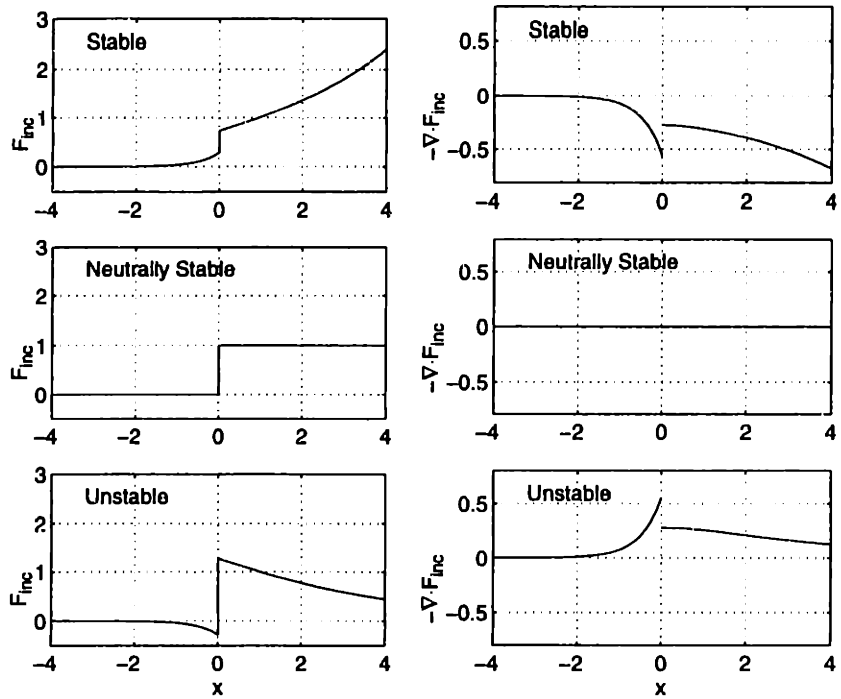

(a) Flux, $\mathcal{F}_{inc}$

(b) Rate of disturbance-energy change per unit length: $\iint_{\mathcal{A}} \frac{\partial \mathcal{E}_{inc}}{\partial t} d\mathcal{A}$

Figure 3-1: Disturbance-energy analysis of the Moore-Greitzer mode.

A first step in using the Corollary is to validate it with respect to our model of the flow field. Once we have solved for the eigenvalues and mode shapes (perturbation flow field structure), we can evaluate both terms of the Corollary (3.31): the time derivative term and the divergence term. The annulus integrated disturbance-energy density, $\iint_{\mathcal{A}} \frac{\partial \mathcal{E}_{inc}}{\partial t} d\mathcal{A}$, is plotted in part (b) of the figure. This is essentially the change of disturbance-energy in time per unit length along the compressor. From the Corollary, this term is equal to $-\iint_{\mathcal{A}} \left(\delta P \delta V_x + \rho \frac{\bar{V}^2}{2} \bar{V}_x \right) d\mathcal{A}$. Since these two terms should overlay when plotted together, this type of plot is useful in validating the Corollary. It confirms the direct relation between the time evolution (eigenvalues) and the spatial structure (mode shapes) of the pre-stall flow field. This validation method will also be used in the next section for compressible flow. This plot is also a direct illustration of the stability of the mode since the sign determines stability: negative is stable and positive is unstable. We notice that the entire mode shape is either stable, neutrally stable or unstable; one axial portion of the mode can't be unstable while the rest is stable.

3.2.4 Compressible flow field

To validate the Disturbance-Energy Corollary (Eqn 3.10) with *2DCompSIM*, we can plot the annulus integrated values of $\frac{\partial \mathcal{E}}{\partial t}$ and $-\vec{\nabla} \cdot \left(\vec{\mathcal{I}} + \mathcal{E}\vec{V}\right)$ versus axial distance on the same plot, and they should coincide. Figure 3-2 shows this agreement in the ducts and gaps for the 11 stage [1,0] mode for three levels of stability: stable, neutrally stable, and unstable.

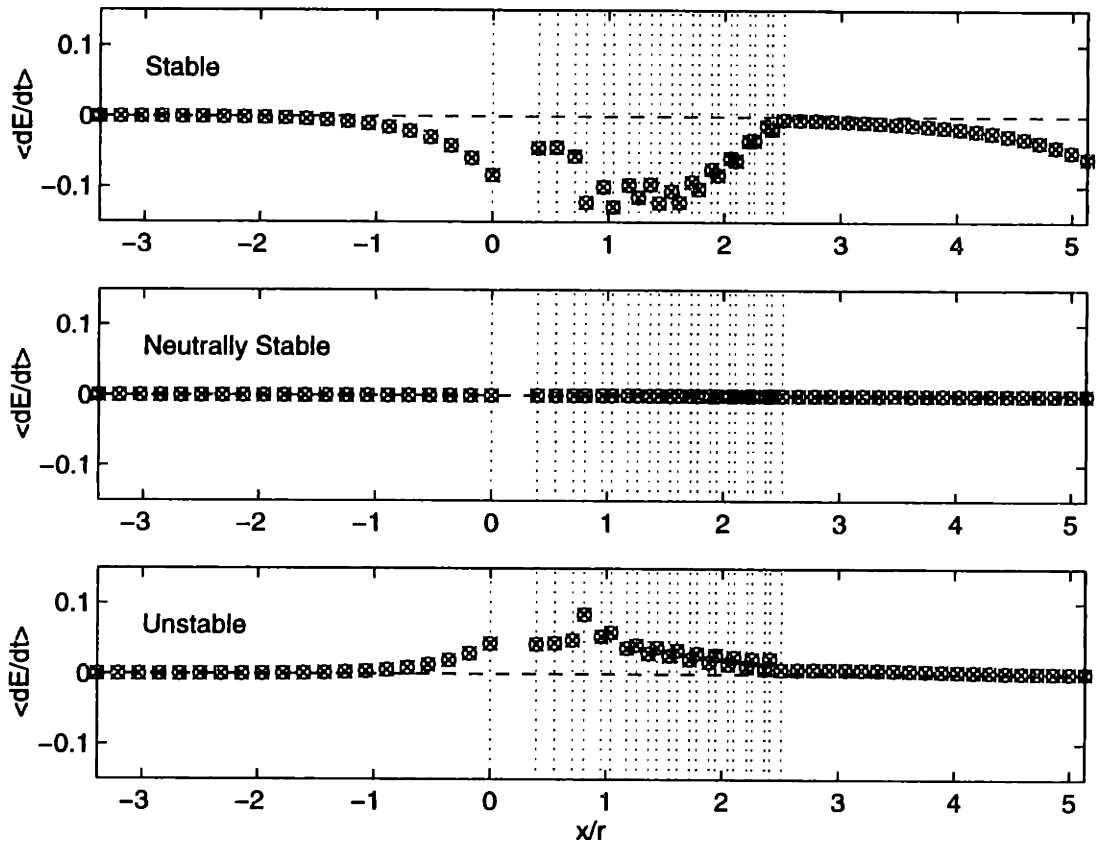

Figure 3-2: Annulus integrated terms of the Disturbance-Energy Corollary evaluated at various axial locations (11 stage, design speed, inlet Mach number of 0.447). Overlying of the × and o symbols demonstrates the consistency of the Disturbance-Energy Corollary with the compressible model *2DCompSIM*. $< dE/dt >$ is the area integrated rate of change of disturbance-energy.

Figure 3-3 (a) presents the flux, $\mathcal{F}$ along the ducts and within the gaps for the neutrally stable [1,2] mode of the 11 stage compressor. The source power of each blade row is then calculated by taking the difference between the trailing edge and leading edge fluxes. This is shown in part (b) of the same figure. From the integral of the Corrolary over the entire compression system (Eqn 3.28), the sum of disturbance-powers of all blade rows should be equal to the disturbance-enthalpy flux out minus the disturbance-enthalpy flux in, which it can be shown to be.

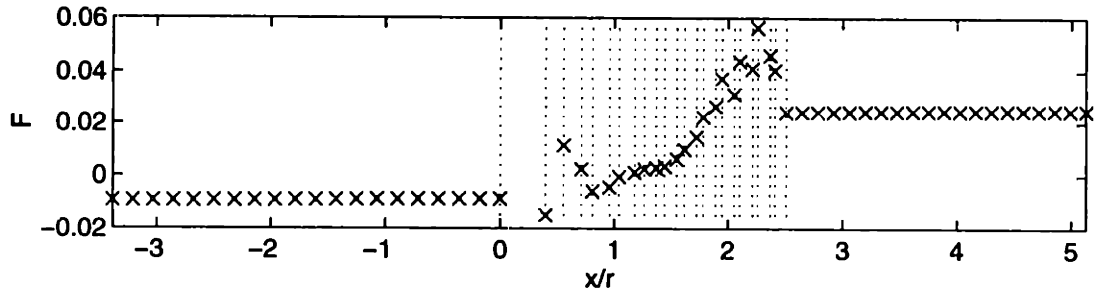

(a) Flux, $\mathcal{F}_{inc}$

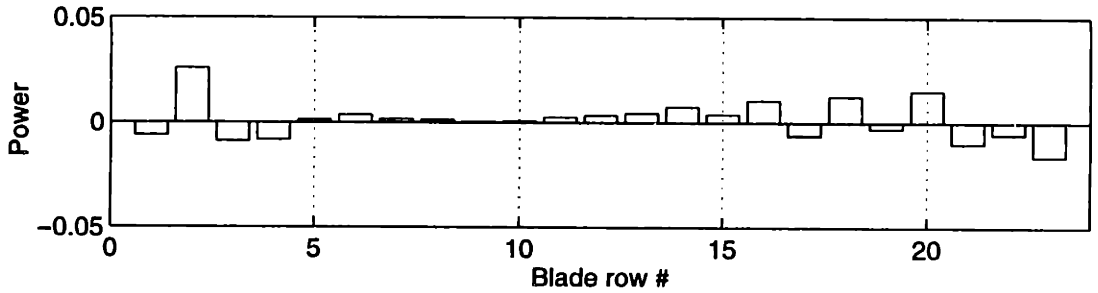

(b) Source Power, $\mathcal{P}$

Figure 3-3: Disturbance-energy analysis of the [1,2] mode from *2DCompSIM* (11stage, design speed, M=0.4120, near neutral stability, -0.0010 + 1.2177i).

The relative importance of the blade rows is determined by comparing their powers. We notice for example, the higher power in the front and rear stages compared to the mid-stages. Also, the rotors mostly act as sources while the stators tend to dissipate energy. A description of disturbance-power is presented in the following section, explaining the mechanisms of disturbance-energy creation.

3.3 Disturbance-power of compressor blade rows

As stated previously, the level of stability is given by the balance between disturbance-power of the blade rows and net flux of stagnation disturbance-enthalpy flowing out of the compression system. The power of a blade row was shown to be equal to its ability to emit disturbance-intensity and create kinetic and internal disturbance-energy (Eqn 3.29). We can express the three main parts of $\mathcal{F}_2 - \mathcal{F}_1$ ($\Delta\mathcal{F}$) as:

$$\Delta\mathcal{F}_I = \iint_{A_2} \delta P \delta V_x \, dA - \iint_{A_1} \delta P \delta V_x \, dA \tag{3.33a}$$

$$\Delta\mathcal{F}_{KE} = \iint_{A_2} \frac{\bar{\rho}(\delta V)^2}{2} \bar{V}_x \, dA - \iint_{A_{l.e}} \frac{\bar{\rho}(\delta V)^2}{2} \bar{V}_x \, dA \tag{3.33b}$$

$$\Delta\mathcal{F}_{PE} = \iint_{A_2} \frac{\delta P^2}{2\bar{\rho}\bar{a}^2} \bar{V}_x \, dA - \iint_{A_1} \frac{\delta P^2}{2\bar{\rho}\bar{a}^2} \bar{V}_x \, dA \tag{3.33c}$$

with:

$$\mathcal{F} = \mathcal{F}_I + \mathcal{F}_{KE} + \mathcal{F}_{PE} \tag{3.33}$$

An increase in either one of these fluxes is equivalent to an increase in blade row power (for the same level of stability). The power could also be decomposed into three parts:

$$\mathcal{P} = \mathcal{P}_I + \mathcal{P}_{KE} + \mathcal{P}_{PE} \tag{3.34}$$

Although these powers are not independent, its useful to consider them separately in order to understand the mechanisms that increase of stagnation disturbance-enthalpy flux across a blade row.

3.3.1 Mechanisms of stagnation disturbance-enthalpy creation

The presence of a blade row in a flow field with small amplitude perturbations will generate pressure disturbances propagating upstream and downstream along with vortical and entropic disturbances convecting downstream. These created disturbances may carry along disturbance-energy or intensity (i.e. stagnation disturbance-enthalpy, f). The abil-

ity of a blade row to increase the disturbance-energy or intensity fluxes represents its power. In the stability models, this information is contained within the blade row model adopted. The relations used to represent the blade row, such as actuator disk relations, semi-actuator disk relations, distributed body forces or CFD, describe the mechanisms of stagnation disturbance-enthalpy creation. Whereas Section 3.2.2 described how to calculate the blade row disturbance-power, this section will present the basic mechanisms of stagnation disturbance-enthalpy creation, yielding a physical understanding of disturbance-power.

Disturbance-intensity flux, $\Delta\mathcal{F}_I$

As discussed in Section 3.2, a change in disturbance-intensity flux is characterized by a change in *magnitudes* of pressure or axial velocity perturbations across the blade row, or a change in their relative *phase*. This mechanism can be illustrated using the pressure matching relation across the blade row. Recalling Eqn A.33 developed in Section A.1.4 for a simple actuator disk representation of the compressor:

$$\frac{\delta P_{ex} - \delta P_{in}}{\rho_o {U_o}^2} = \delta\Psi^{ss} - \mu\frac{\partial\delta\phi}{\partial\tau} - \lambda\frac{\partial\delta\phi}{\partial\theta} \tag{A.33}$$

we can multiply it by $\delta V_x/U_o$ an integrate over the annulus area to obtain $\Delta\mathcal{F}_I$ on the left hand side:

$$\iint\limits_A \left(\frac{\delta P_{ex} - \delta P_{in}}{\rho_o {U_o}^2}\right)\frac{\delta V_x}{U_o}d\mathcal{A} = \iint\limits_A (\delta\Psi^{ss}\delta\phi)d\mathcal{A} - \iint\limits_A \left(\mu\frac{\partial\delta\phi}{\partial\tau}\delta\phi\right)d\mathcal{A} - \iint\limits_A \left(\lambda\frac{\partial\delta\phi}{\partial\theta}\delta\phi\right)d\mathcal{A} \tag{3.35}$$

$$\frac{1}{\rho_o U_o^3}\Delta\mathcal{F}_I = \iint\limits_A (\delta\Psi^{ss}\delta\phi)d\mathcal{A} - \iint\limits_A \left(\mu\frac{\partial(\delta\phi^2/2)}{\partial\tau}\right)d\mathcal{A} \tag{3.36}$$

where the last term integrated to zero. Noting that the integral of the time derivative is the rate of change of kinetic disturbance-energy for incompressible flow (Section 3.2.3), the blade row power due to its ability to increase disturbance-intensity flux is therefore:

$$\frac{\mathcal{P}_I}{\rho_o U_o^3} = \iint\limits_A (\delta\Psi^{ss}\delta\phi)d\mathcal{A} \tag{3.37}$$

The steady-state static-to-static pressure rise perturbation, $\delta\Psi^{ss}$, is given by the constitutive relations modeling the blade row. In this simple derivation of $\mathcal{P}_I$, we considered $\delta V_{x,1} = \delta V_{x,2}$. A larger trailing edge axial velocity perturbation would *increase* the intensity-power, $\mathcal{P}_I$.

Kinetic disturbance-energy flux, $\Delta\mathcal{F}_{KE}$

From Eqn 3.33*b*, the power of a blade row will increase if the magnitude the velocity perturbation increases. In our 2D representation: $\delta V^2 = \delta V_x^2 + \delta V_\theta^2$. The axial component of velocity is guided by mass conservation, while the tangential component depends on mass conservation and turning. As illustrated in Figure 3-4 (a), larger trailing edge δV_x results in larger δV_θ. This can result from an area reduction (blockage) or a decrease in density. Also, increased exit flow angle results in increased δV_θ for the same δV_x, as shown in Figure 3-4 (b). The exit flow angle will increase if the deviation or the stagger angle are increased.

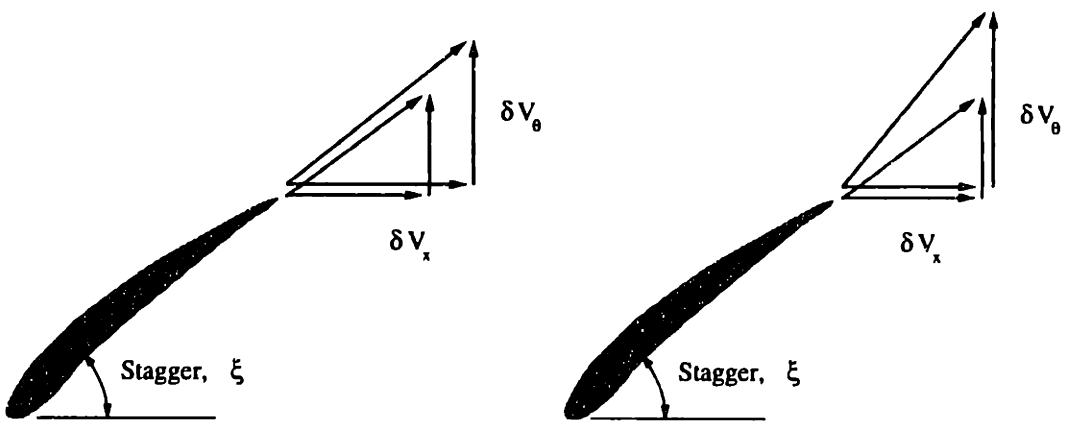

(a) Effect of larger exit axial velocity perturbation

(b) Effect of larger exit flow angle

Figure 3-4: Changes in kinetic disturbance-energy flux.

Internal disturbance-energy flux, $\Delta\mathcal{F}_{PE}$

From Eqn 3.33*c*, the power of a blade row will increase if the magnitude of δP_2 increases. The exit pressure perturbation depends mainly on the blade row pressure matching relation,

as discussed above.

3.3.2 Application to blade row models

Applying the above mechanisms to simple blade row models will reveal the links between the parameters describing the blade rows and their disturbance-power.

Moore-Greitzer compressor model

The steady-state static-to-static pressure rise perturbation, $\delta\Psi^{ss}$, is represented in the Moore-Greitzer model as the slope of the static-to-static characteristic times the axial velocity perturbation: $\frac{\partial\Psi^{ss}}{\partial\phi}\delta\phi$. In this case, the intensity component of the power (Eqn 3.37) becomes:

$$\frac{\mathcal{P}_I}{\rho_o U_o^3} = \iint_A \left(\frac{\partial\Psi^{ss}}{\partial\phi}\delta\phi^2\right) d\mathcal{A} \tag{3.38}$$

$$= \frac{\partial\Psi^{ss}}{\partial\phi} \iint_A \delta\phi^2 d\mathcal{A} \tag{3.39}$$

Since the area integral of a perturbation squared is always positive, the intensity-power scales with the slope of the static-to-static characteristic, $\frac{\partial\Psi^{ss}}{\partial\phi}$, and *takes its sign.* The intensity-power also scales with $|\delta V_x|^2$.

In the Moore-Greitzer model, the other matching relations across the compressor are given by continuity and no exit swirl:

$$\delta V_{x,1} = \delta V_{x,2} \tag{3.40}$$

$$\delta V_{\theta,2} = 0 \tag{3.41}$$

The kinetic-power, $\mathcal{P}_{KE}$, is therefore, for constant area and density:

$$\mathcal{P}_{KE} = \iint_A \frac{\bar{\rho}}{2}(\delta V_{x,2}^2)\bar{V}_x - \frac{\bar{\rho}}{2}(\delta V_{x,1}^2 + \delta V_{\theta,1}^2)\bar{V}_x \, d\mathcal{A} \tag{3.42}$$

$$\mathcal{P}_{KE} = -\frac{\bar{\rho}\bar{V}_x}{2} \iint_A \delta V_{\theta,1}^2 \, d\mathcal{A} \tag{3.43}$$

To first order, a stage with no exit swirl acts as a sink of kinetic disturbance-energy. Physically, the incoming tangential velocity perturbations are eliminated since the blade passages do not allow cross-flow. A non-zero exit flow angle would allow tangential velocity perturbations and therefore reduce the damping effect of the blade row.

Since incompressible flow does not have internal disturbance-energy, the blade row power is $\mathcal{P}_I + \mathcal{P}_{KE}$. At neutral stability, the power will be equal to the net flux of stagnation disturbance-enthalpy:

$$\mathcal{P}_{inc} = \iint_A \frac{\partial \Psi^{ss}}{\partial \phi} \delta\phi^2 - \frac{\bar{\rho}(\delta V_{\theta,1}^2)}{2} \bar{V}_x \, dA \tag{3.44}$$

At neutral stability, the power will be equal to the net flux of stagnation disturbance-enthalpy. Using the exit duct relations in Appendix A to define the inlet and exit duct fluxes, we can derive the neutral stability criteria: $\frac{\partial \Psi^{ts}}{\partial \phi} = 0$.

2DCompSIM blade row model

The semi-actuator disk approach used in *2DCompSIM* is relatively more complex than the simple incompressible actuator disk since the perturbations evolve along the 1D ducts representing the blade passages (see Figure 2-2 for the semi-actuator disk description). Also, each blade row operates with different inlet velocity and pressure disturbances, so the blade rows cannot be collapsed into a single actuator disk. Therefore, this model does not lead to the formulation of an overall stability parameter such as $\frac{\partial \Psi^{ts}}{\partial \phi}$, which came from the Moore-Greitzer model.

These mechanisms definitely deserve a thorough investigation since they are the heart of disturbance-power and therefore of compressor stability. However, the mechanisms presented here will enable us to identify parameters guiding disturbance-power generation, explain their effect on stability and therefore redesign a compressor with enhanced stability.

3.4 Summary and general application

In this chapter, a stability analysis based on total fluid energy was presented, stating that the pre-stall modal waves will grow if the blade rows produce more *disturbance-energy* then the net flux of *disturbance-energy and intensity* out of the compression system. This conservation law was derived by integrating a corollary for second order energy over the entire compressor. The disturbance-power of each blade row can be determined by integrating the Corollary across the individual blade rows. It was found that the blade row power is a function of the blade row's ability to increase the pressure and velocity disturbances, and also related to the phase change of pressure and axial velocity it creates. For simple blade row models (Moore-Greitzer), this is represented by the slope of the static-to-static pressure rise characteristic and the magnitude of the incoming tangential velocity perturbations. More detailed blade row models propose that the disturbance-power is also a function of the axial velocity ratio across the blade row, the exit flow angle and its sensitivity to inlet flow conditions (such as incidence).

Although the focus of this chapter was on instability inception of 2D, linear pre-stall modes in high-speed axial compressors, this energy-based analysis is general and applicable to many types of compressor flows: linear or non-linear, 2-D or 3-D:

3-D Modes The stability of radial modes could be investigated by determining the spanwise distribution of 'source power' and relating it to the radial variations in airfoil geometry (or other design parameters).

Non-Linear As shown by Myers [37], his Corollary 3.12 can be generalized for disturbances that are not necessarily of small amplitude, making this approach applicable to non-linear models of instability inception. The presence of a diffusion term in Myers' Corollary may however limit its usefulness in understanding this non-linear dynamic behavior. Another approach would be to rewrite the Corrolary based on the non-linear equations and collect the non-linear terms on the right hand side. This procedure makes the non-linearities in the fluid motion appear as source of disturbance-energy, which is the essence of aerodynamic sound production such as jet noise (See Dowling and Ffowcs-Williams for more

details [6])

Other Blade Row Models Also, the Corollary can be useful for models that replace the turning and loss across the blade rows by distributed body-forces. An expression for the source power, $\mathcal{P}$, can then be directly determined since it would appear naturally as a body-force term if the Corollary were reformulated with body forces.

Active Control This energy-based approach may also allow a better understanding and design of active control schemes for stabilizing fluid systems. Electro-mechanical and aero-mechanical feedback schemes can be evaluated by determining the disturbance-power of the actuator or the effect of actuation on the power of the other system components. Such an approach was actually used by Epstein, Ffowcs Williams and Greitzer in their pioneer work on active control of compressor instabilities [9]. The effectiveness of various actuator designs and their location can be analyzed from a physical stand point, complementing methods developed in control theory. Also, the expression disturbance-energy could be used as a candidate Lyapunov function for the design of non-linear controllers.

Finally, the stability of unsteady flows other than pre-stall flow fields in compressors could also be analyzed using this approach, with examples such as flutter instabilities and combustion instabilities. The concept of disturbance-energy and power deserves further investigation on theoretical aspects, to develop a better understanding, and on application aspects, to exploit the uses of this concept.

CHAPTER 4

SURGE LINE PREDICTIVE CAPABILITY OF THE COMPRESSIBLE STABILITY MODEL

The compression system stability modeling tools presented up to now, can be used to predict the point of instability inception, and therefore the surge line of a compressor. This chapter will assess the expected uncertainty on this prediction, given errors on the input values to the mean flow and stability calculations. The first two sections describes the approach and methodology used to address this issue. The following sections present the prediction uncertainties, first on the eigenvalues and then on surge margin.

4.1 Approach

Current surge line prediction in gas turbine engine companies relies on empirical correlations and experimental results from previously designed compressors. An example is the diffuser-based procedure for estimating the maximum pressure rise potential of axial flow compressor stages presented by Koch [27]. The more recent compressor stability models offer the possibility of predicting the modal stall part of the surge line from basic principles, using knowledge of the steady flow and a few unsteady flow parameters. The accuracy of this prediction depends on:

1. the underlying model: Do the constitutive relations and modeling assumptions capture all the necessary physics of rotating stall inception?
2. the input parameters to the model: Are the inputs precise enough to accurately represent the compressor's dynamics near stall?

This Chapter will focus mainly on this second point. The first point has been assessed by many through the past decade, since it is the main concern while developing the models. As shown by Haynes [16], the linearized Moore-Greitzer (incompressible) model with unsteady blade row performance (lags) compared well with experiments for a low-speed axial compressor. The compressible model was shown by Tryfonidis et al. [42] to capture part of the multi-modal behavior of a 4-stage high speed compressor. While closing the throttle at constant design speed, the compressible model predicted the [1,1] mode becoming unstable before the [1,0] mode and the experimental measurements showed growing traveling wave energy at rotor frequency. Since the natural frequency of the [1,1] mode was close to the rotor frequency, it was conjectured that rotating stall was initiated by this lightly damped [1,1] mode. Furthermore, Hendricks et al. [18] also offered some validation of the compressible modeling assumptions by showing stall/surge events from a non-linear formulation of Bonnaure's model that matched well with experimental data for an 11-stage high-speed compressor. This model, however, included additional and different dynamics than the compressible model used in this thesis (*2DCompSIM*): interstage bleed ports modeled by the Euler equations and a plenum-throttle type exit boundary condition common for all harmonics.

More rigorous was the system identification on a high-speed single stage compressor presented by Weigl et al. [47]. The modes with frequencies between -2 and 2 times rotor frequency where experimentally identified by measuring the response of the compression system to circumferentially distributed air injection. The frequencies of the identified modes agreed with those predicted by the compressible model, but the damping coefficients (and thus the mass flow at stall) did not relate very well. The necessary constitutive relations describing these modes seem to be included in the compressible model, but the accuracy of the prediction is fairly poor. A first step towards the accurate prediction of compressor dynamics is to know the effect of input uncertainties on the prediction. This will be the main focus of this chapter. The second step would consist of assessing the effect of additional

dynamics and is proposed as future work to be done.

Since, the mass flow at neutral stability is reached when the growth rate of the least stable eigenvalue becomes zero, the uncertainty on the surge line prediction is determined by our ability to predict the position of the eigenvalues. As shown in figure 2-3, the process to calculate the system dynamics is composed of many steps, each of which propagates the uncertainties on the inputs and can also introduce new ones. The goal of this chapter is to characterize the propagation of uncertainty and quantify how well the various inputs need to be known in order to get an accurate prediction of the stalling mass flow and system dynamics.

The approach is to first determine the sensitivity of the eigenvalues with respect to the various inputs. This sensitivity study method is described in the next section. For given errors on the inputs, the uncertainties on the eigenvalues are determined according to their respective sensitivities. Section 4.3 shows results for the inputs related to the *steady flow*, while section 4.4 focuses on the *unsteady flow* parameters. Since additional errors may be introduced due to our modeling of the steady flow and mean geometry (STEP 2 in Figure 2-3), section 4.5 will present the effect of these modeling assumptions on the eigenvalues. Finally, section 4.6 combines the effect of all input uncertainties on the eigenvalues and relates it to the predicted surge line uncertainty. This chapter focuses *magnitudes* of the effects of input parameter errors, while Chapter 5 will discuss the *trends* of stability with respect to changes in the input parameters.

To be relevant, the modern 11-stage high-speed compressor described in Section 1.3 which is representative of current designs for gas turbine engines is chosen for this study. Leakage out of the main flow path occurs through the gaps between each rotating and non-rotating part. The amount of air removed from the main flow path affects the operation of the downstream blade rows and will therefore be considered as a performance parameter along with loss, deviation and blockage. Both leakage and compressor bleed air will be referred to as "bleeds" and expressed in percentage of the inlet mass flow.

4.2 Sensitivity analysis methodology

Two main groups of inputs are considered individually:

- the steady flow parameters: inputs that are needed for the steady background flow calculation, such as geometry, losses, deviations, blockages, bleeds and the slopes;
- the unsteady flow parameters: inputs that are needed to characterize the unsteady flow behavior in the compression system, such as time lag constants for loss and deviation, and boundary conditions.

The method to calculate these sensitivities can either be analytical or numerical. For low-speed compressors, the steady flow calculation as well as the stability model are fairly simple and can be solved for analytically (without unsteady losses nor deviation), as done in Appendix A. The sensitivity coefficients can therefore be found by differentiating the analytical expressions for the eigenvalue. The sensitivity of an output "Y" to changes of an input "X" is then expressed as:

$$S_X^Y = \frac{\partial Y}{\partial X} \tag{4.1}$$

For high-speed compressors, the sensitivity coefficients are solved numerically using the procedures presented in Figure 4-1, for the steady and unsteady flow parameters.

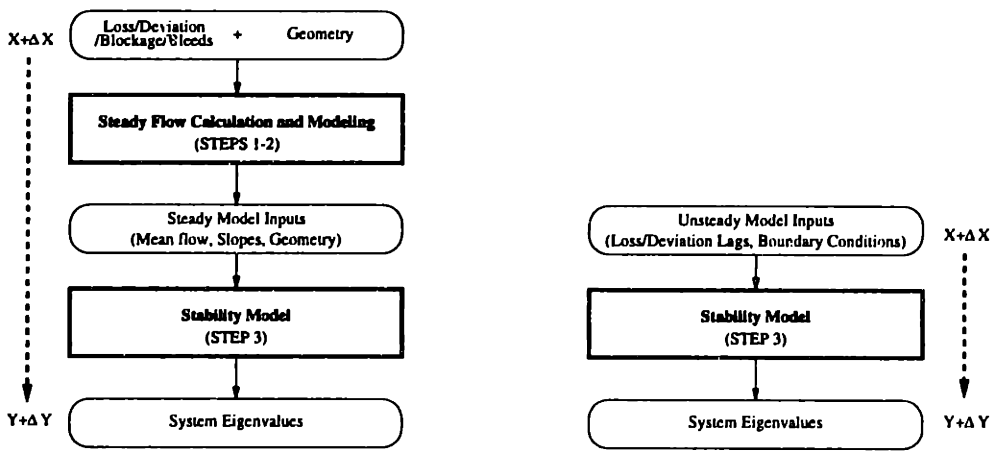

(a) Steady flow parameters

(b) Unsteady flow parameters

Figure 4-1: Sensitivity coefficient calculation procedure for high-speed compressors.

The sensitivity of the eigenvalues to an input is determined through the following steps:

1. Calculate the unperturbed output: Y (eigenvalue calculation with the unperturbed input, X);
2. Perturb one input: $X + \Delta X$ ($\Delta X \ll X$);
3. Calculate the perturbed output: $Y + \Delta Y$ (eigenvalue calculation with the perturbed input, $X + \Delta X$);
4. Sensitivity coefficient is then:

$$S_X^Y = \frac{\Delta Y}{\Delta X} \quad \left(\approx \frac{\partial Y}{\partial X}\right) \tag{4.2}$$

The overall output uncertainty results from combining the effect of all input uncertainties and errors.

Combination of uncertainties for random-type variables

The loss, deviation, and blockage are determined from correlations mainly based on experimental results. This type of input is characterized by a *random error*, or *uncertainty* that can be defined by a Gaussian distribution of mean, $mean(X)$, and variance, $var(X)$. As detailed by Brown [2], the output will then also be characterized by a normal distribution $(mean(Y), var(Y))$. For a linear system[1], the variance of the random output is related to that of the input by the square of the sensitivity of the output to the input:

$$var(Y) = \left(\frac{\partial Y}{\partial X}\right)^2 var(X) \tag{4.3}$$

Finally, since the output, Y, is a function of many inputs, X_k, the combined effect of the input uncertainties on the eigenvalues is expressed as:

$$var(Y) = \sum_{k=inputs} \left(\frac{\partial Y}{\partial X_k}\right)^2 var(X_k) \tag{4.4}$$

[1]Our entire computation procedure can be considered linear (even though the mean flow calculation is a set of non-linear equations) since the inputs will only be *perturbed*, i.e. varied by a small quantity ΔX.

The 95% confidence range on the output is then:

$$\Delta Y = 2 * \sqrt{var(Y)} \tag{4.5}$$

Combination of uncertainties for deterministic-type variables

The other type of variables is mostly characterized by a *bias-error*: the value of the parameter is likely to be over or underestimated, as opposed to being randomly located in a certain range. This method results in larger output error than the statistical method described above.

For small input perturbations, the error on the output is simply the linear combination of the input errors, weighted by the output's sensitivity to each input:

$$\Delta Y = \sum_{k=inputs} \frac{\partial Y}{\partial X_k} \Delta X_k \tag{4.6}$$

This linear combination is also used to combine the effects of random-type variables with those of deterministic-type variables. Using this approach, the range of confidence on our predicted eigenvalues will be the sum of uncertainties due to input parameter errors (steady and unsteady) and modeling introduced errors.

Regions of uncertainty

A graphical method will be used to present the uncertainties on the eigenvalues. The prediction of an eigenvalue is actually the prediction of two outputs: the real and imaginary parts of the eigenvalue. The region in the complex plane where an eigenvalue can lie to 95% confidence will be referred to as the *region of uncertainty*[2]. In order to conserve directionality of the eigenvalue motion, this region will not be determined along the real and imaginary axes, but along the main direction of eigenvalue motion and normal to that direction. The resulting region will be an ellipse with the major axis aligned with the main direction of eigenvalue motion. An example is shown in Figure 4-2.

[2]The terms "uncertainty" is used for both deterministic and random errors, even though it should be restricted to random errors only.

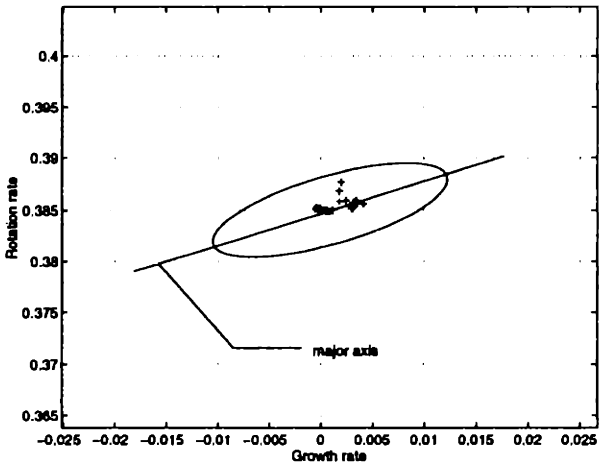

Figure 4-2: Example of an uncertainty region enclosing the possible locations of the eigenvalues to 95% confidence.

4.3 Effect of steady flow parameter uncertainties

This section presents how the eigenvalue prediction accuracy is affected by uncertainties on the steady flow parameters. This effect is calculated by the process shown in Figure 4-1 (a). The effects of loss, deviation, blockage and bleed are first presented, followed by the slopes of loss and deviation.

4.3.1 Values of loss, deviation, blockage, and bleed

For each blade row, the amount of loss, deviation, and blockage is determined from correlations and experimental measurements, giving these values random-type properties. In the calculations, a small value is applied as a bias on the loss, deviation, or blockage characteristic for each blade row individually. The steady flow and the eigenvalues are then calculated, leading to the sensitivities (Eqn 4.2). The uncertainty on the prediction due to uncertainties on the losses for example, is then determined by combining the sensitivities with the actual uncertainties for all the blade rows, as defined in Eqn 4.3. The effect of bleed uncertainty is calculated similarly, except that the change in bleed mass flow at one station affects the mass flow in all the following stages.

Typical input uncertainties

Table 4.1 shows the range of uncertainty (to 95% confidence) on the steady flow input values, for both near stall operation and the design operating conditions. The uncertainties near stall are greater than at design conditions. These values are representative of uncertainties encountered with mean-line calculation procedures used in the aircraft gas turbine industry [29, 8]. Loss, deviation, and blockage uncertainties were determined by comparing predicted with measured speedlines and distributing the error between the two among the empirical parameters. Further discussion of these uncertainties is deferred till Section 4.3.3.

	loss, ω_l'	deviation, $\delta°$	l.e. blockage, $\bar{k}_1$	t.e. blockage, $\bar{k}_2$	bleed
Design	0.005	0.2°	0.5%	0.5%	0.1%
Near Stall	0.01	0.3°	0.5%	0.5%	0.1%

Table 4.1: Uncertainties on the steady flow input values.

Individual effects The regions of uncertainty due to each steady flow performance parameters are presented in Figures 4-4 for loss, deviation, and blockage and 4-5 for bleeds. The [1,0] mode is the most affected by these uncertainties, and the loss coefficient propagates the most uncertainty on the eigenvalue.

Combined effect The combined effect of all these steady flow performance uncertainties is presented in Figure 4-6. The resulting uncertainty is considerable in a practical engineering sense, as we will conclude in Section 4.6.

4.3.2 Slopes of loss and deviation

The uncertainty on the slopes of loss or deviation directly relate the uncertainties of the values, as shown in Figure 4-3. The error on the loss coefficient, for example, allows the loss bucket to lie within a certain range. The uncertainty on the slope is then the given by the maximum and minimum slope curves within the uncertainty range. Evaluating such slope uncertainties is not trivial. A simplified approach would consist of fitting a straight line within appropriate bounds. The expressions in Table 4.2 represent the slope uncertainty

estimation given the uncertainties on loss and deviation along with the ranges of leading edge Mach number ($M_1'^+ - M_1'^-$), leading edge relative flow angle ($\beta_1^+ - \beta_1^-$) and loss coefficient ($\omega_l'^+ - \omega_l'^-$). These ranges where chosen based on the loss and deviation characteristics of the 11 stage compressor.

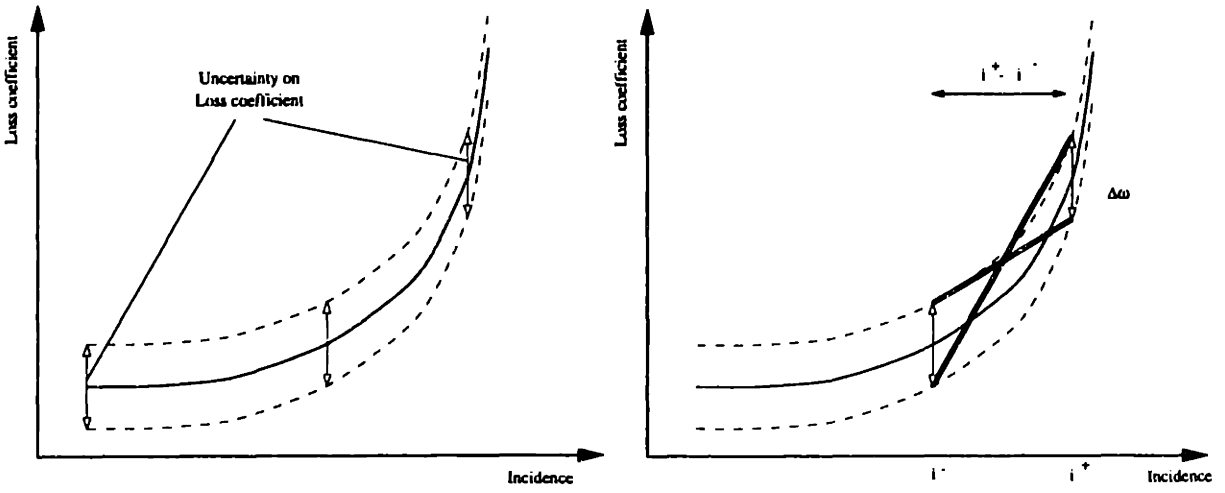

(a) Error

(b) Estimation of the slope uncertainty

Figure 4-3: Slope uncertainty determination from the error on the values.

Typical input uncertainties

From the uncertainties listed in Table 4.1, those on the slopes are:

	$\frac{\partial \omega_l'}{\partial inc}$	$\frac{\partial \omega_l'}{\partial M_1'}$	$\frac{\partial dev}{\partial inc}$	$\frac{\partial dev}{\partial M_1'}$
Uncertainty expression	$2\frac{\partial \omega_l'}{\partial inc}\frac{\Delta\omega_l'}{\omega_l'^+ - \omega_l'^-}$	$2\frac{\Delta\omega_l'}{M_1'^+ - M_1'^-}$	$2\frac{\Delta\beta_2}{\beta_1^+ - \beta_1^-}$	$\frac{0.5°\pi/180}{0.07}$
Average uncertainty	0.02	0.4	0.06	0.12

Table 4.2: Uncertainties on the performance slopes.

Individual effects The regions of uncertainty resulting from each these slopes are shown in Figure 4-7. We note the larger uncertainty on the eigenvalues for the slopes of loss. As for the steady flow values, the slopes affect the [1,0] mode more than others.

Combined effect Figure 4-8 combines the effect of these uncertainties. We note a dominant [1,0] mode uncertainty and a distinguishable frequency uncertainty.

4.3.3 Notes on steady flow parameter uncertainties

The Moore-Greitzer model has two parameters that can effect the real part of the eigenvalue: the total-to-static slope and the inertias (see Eqn 2.5). However, only *one* parameter determines stability: the total-to-static slope. As we approach neutral stability, the sensitivity with respect to inertias decreases since the slope goes to zero. Applying the sensitivity study at neutral stability therefore filters out the parameters that are not directly responsible for stability.

As shown in Appendix A, the total-to-static slope is the combination of loss, deviation and blockage and their slopes. Since measuring the total-to-static pressure rise gives directly the stability (in low-speed compressors), this single measurement should lead to a prediction with less uncertainty, than that from the combination multiple inputs. When we wish to predict the dynamics from basic principles and correlations, such as during the design process, we must deal with the combination of uncertainties on the numerous inputs. From this we can conclude that an overall parameter governing stability in high-speed compressors (such as the total-to-static slope for low-speed compressors, or disturbance-energy) would be useful for practical applications such monitoring the surge margin of a compressor, but may not improve the surge line prediction accuracy during the initial design process. As will be discussed in the last section of this chapter, the prediction uncertainty could be reduced by lowering the error on the inputs through CFD or by completely removing these inputs through the use of more detailed stability models that would not require the empirical loss, deviation, and blockage parameters.

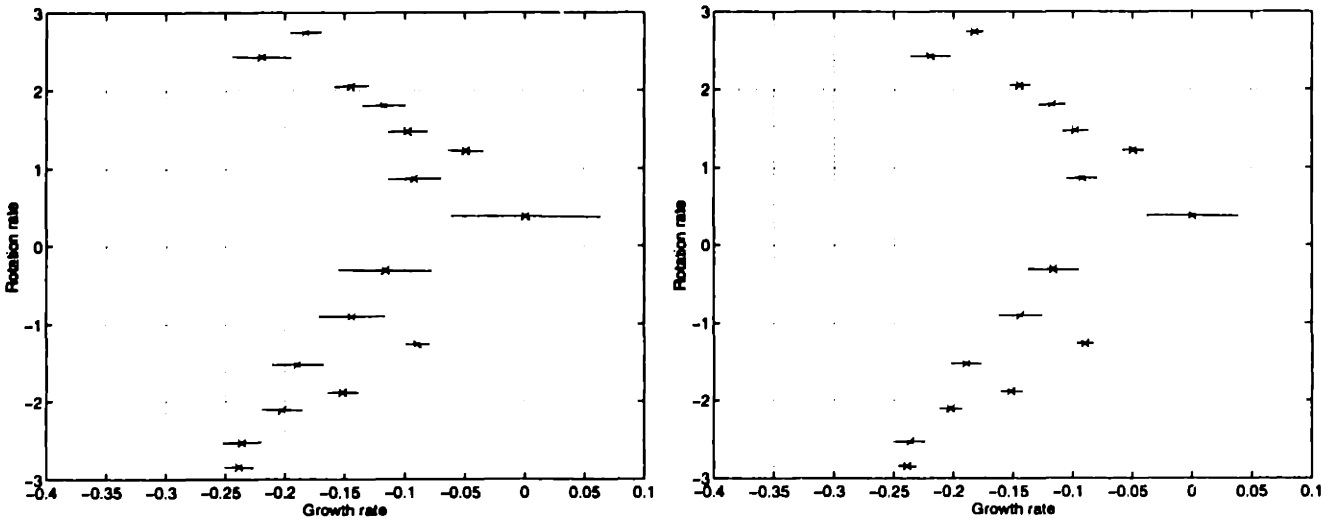

(a) Effect of $\Delta\omega_l'$

(b) Effect of $\Delta\delta^\circ$

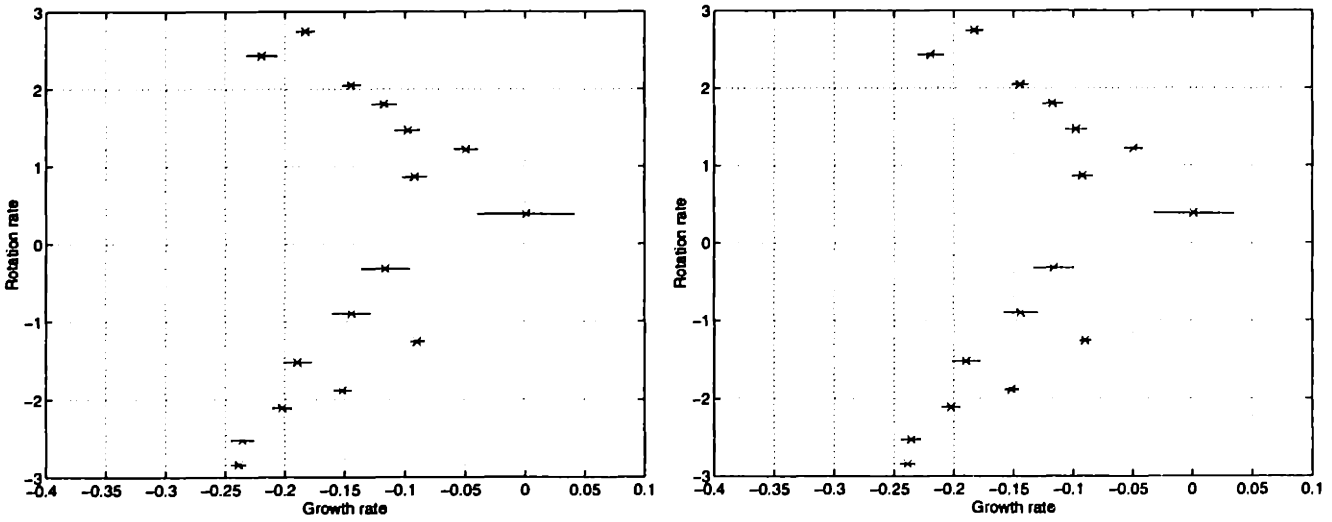

(c) Effect of $\Delta\bar{k}_1$

(d) Effect of $\Delta\bar{k}_2$

Figure 4-4: Individual uncertainty regions for the steady flow parameter values. The ellipses enclose the region of 95% confidence on the eigenvalues ($\times$ are the nominal eigenvalues for the 11 stage at design speed, inlet Mach number of 0.438)

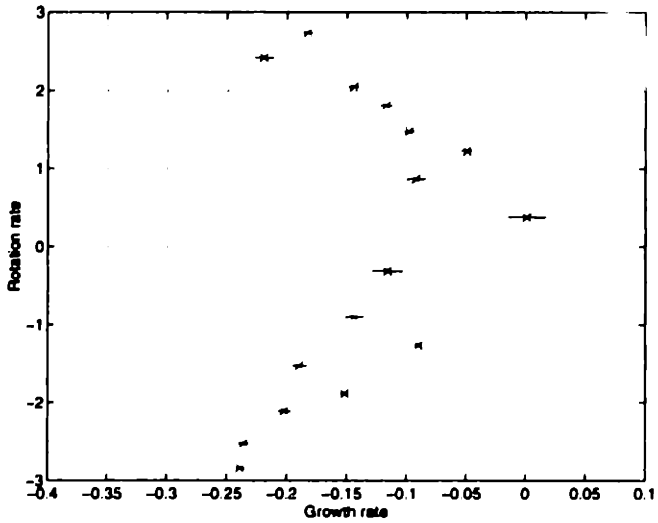

(a) Effect of Δ(bleed)

Figure 4-5: Individual uncertainty regions for bleeds. The ellipses enclose the region of 95% confidence on the eigenvalues (× are the nominal eigenvalues for the 11 stage at design speed, inlet Mach number of 0.438)

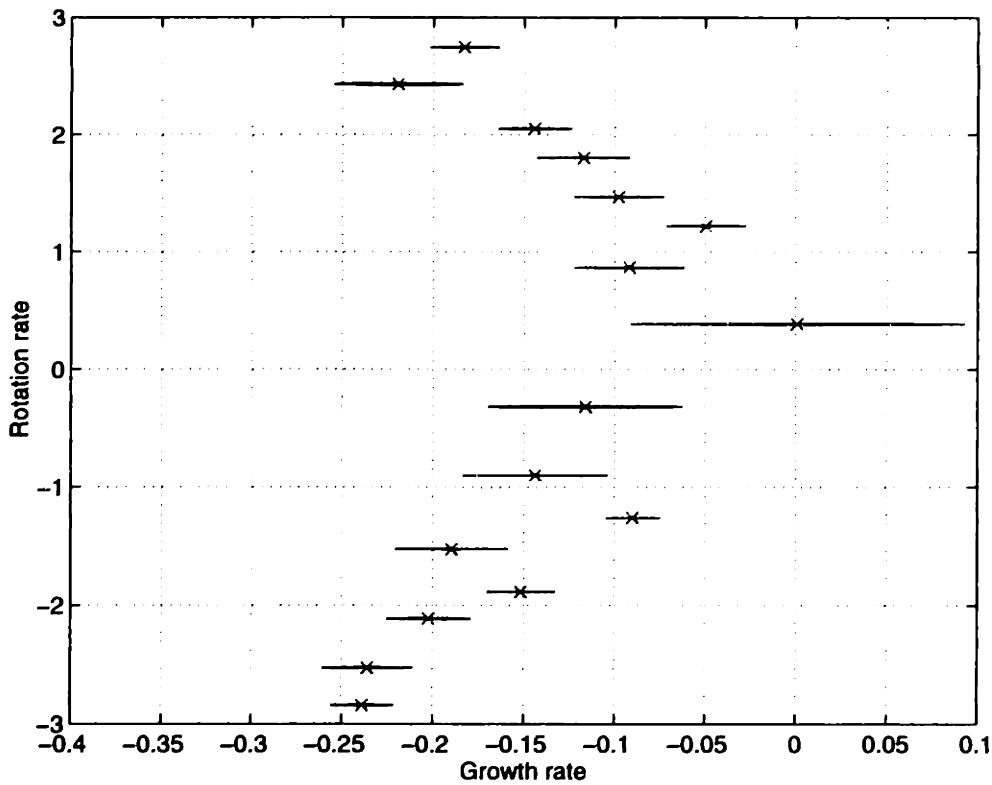

Figure 4-6: Combined uncertainty regions for the steady flow parameter values. The ellipses enclose the region of 95% confidence on the eigenvalues (× are the nominal eigenvalues for the 11 stage at design speed, inlet Mach number of 0.438)

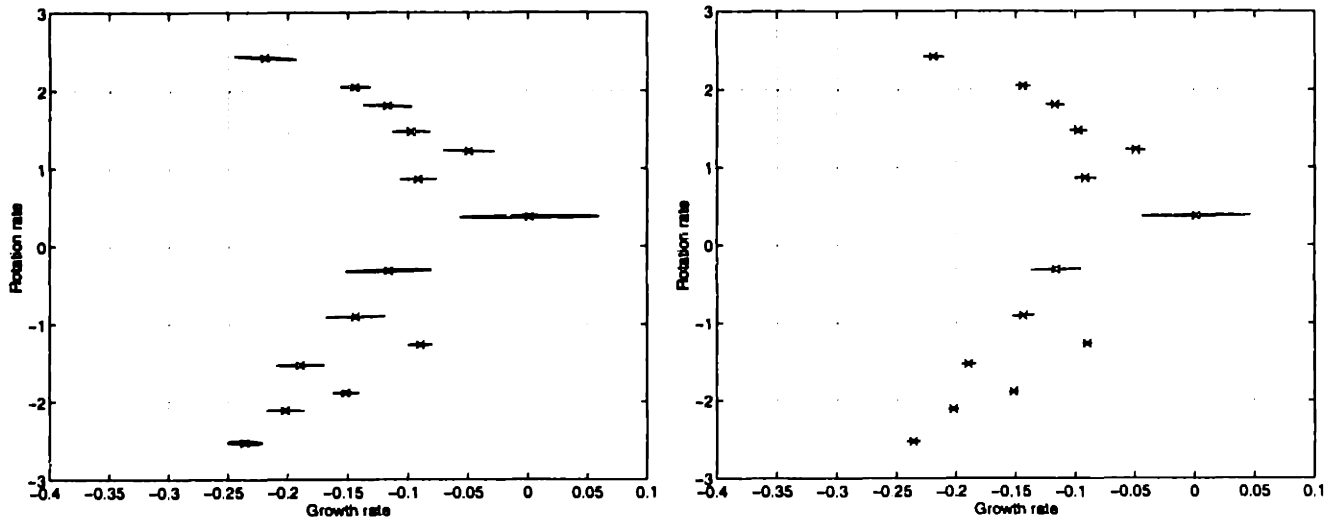

(a) Effect of $\frac{\partial \omega_i'}{\partial inc}$

(b) Effect of $\frac{\partial \omega_i'}{\partial M_1'}$

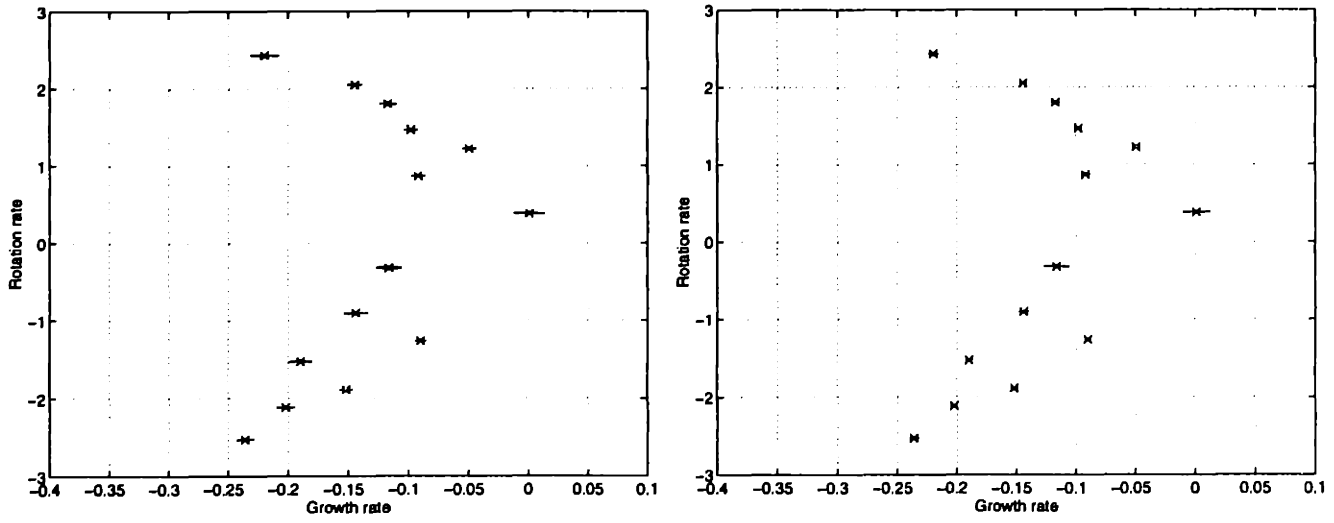

(c) Effect of $\frac{\partial dev}{\partial inc}$

(d) Effect of $\frac{\partial dev}{\partial M_1'}$

Figure 4-7: Individual uncertainty regions for the performance slopes. The ellipses enclose the region of 95% confidence on the eigenvalues (× are the nominal eigenvalues for the 11 stage at design speed, inlet Mach number of 0.438)

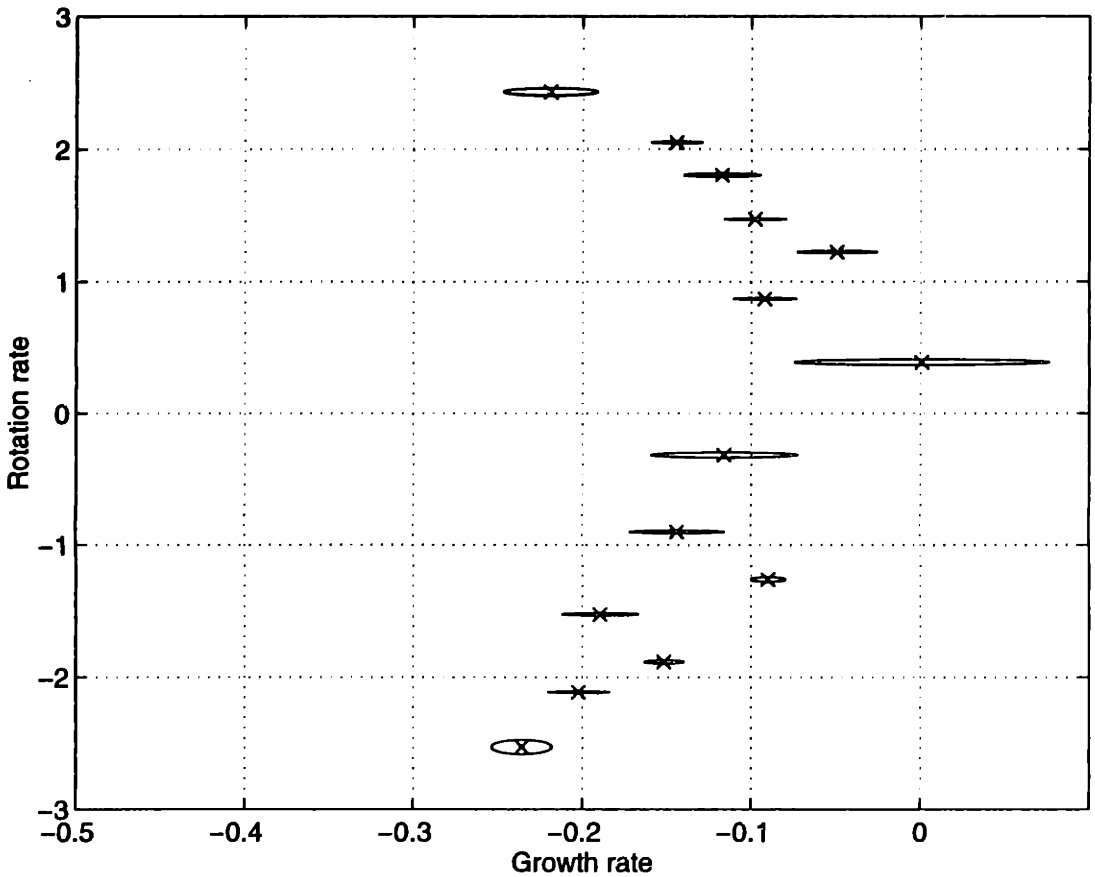

Figure 4-8: Combined uncertainty regions for the performance slopes. The ellipses enclose the region of 95% confidence on the eigenvalues (× are the nominal eigenvalues for the 11 stage at design speed, inlet Mach number of 0.438)

4.4 Effect of unsteady flow parameter errors

The stability calculation requires parameters that are irrelevant to performance calculations such as the time lags of loss and deviation and the impedances at the inlet and exit planes. The effect of uncertainties on these unsteady flow parameters will be calculated using the process shown in Figure 4-1 (b), and presented in the following sections.

4.4.1 Loss and deviation time lag constants

Typical input errors The time taken for a change in inlet flow to a blade row to be seen at its exit as total pressure loss or deviation is not very well defined. Table 4.3 summarizes measured or calculated values of these lags by three researchers, and the chosen time lag errors for the sensitivity analysis in the last column.

Lag constant	Mazzawy [33]	Hoying [19]	Haynes [16]	error
τ_p (loss)	1	0.45	1.5	± 0.5
τ_d (deviation)	$0 to 3$	1	1.5	± 1.5

Table 4.3: Errors on the time lag constants.

The uncertainties on the eigenvalue predictions due to these errors are presented separately in Figure 4-9 and combined in Figure 4-10. Even though the τ_d error is relatively large ($\pm 100\%$!), it doesn't affect the eigenvalue prediction significantly. The time lag constant for losses, however has an important role in prediction accuracy, for both stability and frequency. The higher frequency modes are the most affected.

4.4.2 Boundary conditions

The inlet and exit boundary conditions consist of a specific impedance relation modeling the upstream and downstream components and an axial location where these impedances are to be applied. For a compression system feed by a bell-mouth and discharging into a plenum, the impedances were defined in Chapter 2. Other types of boundary conditions may not be as well defined (such as a downstream throttle) and may introduce errors. To limit the

scope of this study, we will focus on the location where these impedances are to be applied. The inlet and exit planes are not exactly defined since they result from a varying geometry, such as a bell-mouth. The errors on the inlet and exit plane locations will be assumed of the order of $\frac{1}{4}$ radii. The resulting uncertainties on the eigenvalues are shown in Figure 4-11. Generally, higher frequency modes are most sensitive to the boundary conditions. We note the insensitivity of the [1,0] mode, and also the low sensitivity of some higher frequency modes versus others. Figure 4-11 (a) therefore suggests that two types of higher frequency modes exist, characterized by the sensitivity to boundary conditions. Further discussion on boundary conditions is reported to Section 5.2.4.

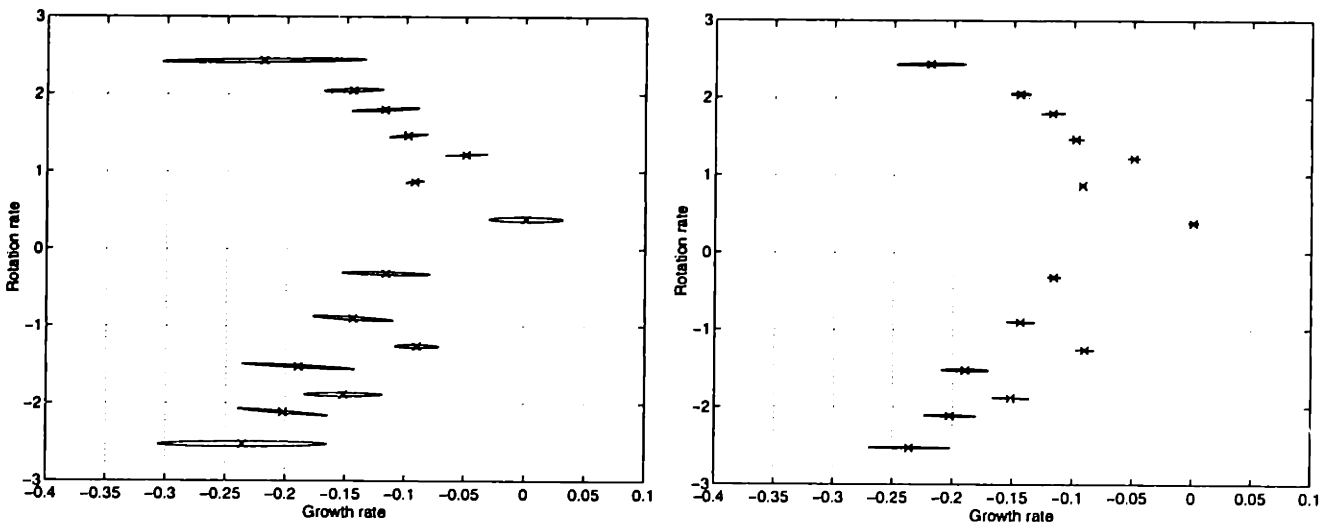

(a) Effect of τ_p

(b) Effect of τ_d

Figure 4-9: Individual uncertainty regions for the time lag constants. The ellipses enclose the region of 95% confidence on the eigenvalues (× are the nominal eigenvalues for the 11 stage at design speed, inlet Mach number of 0.438)

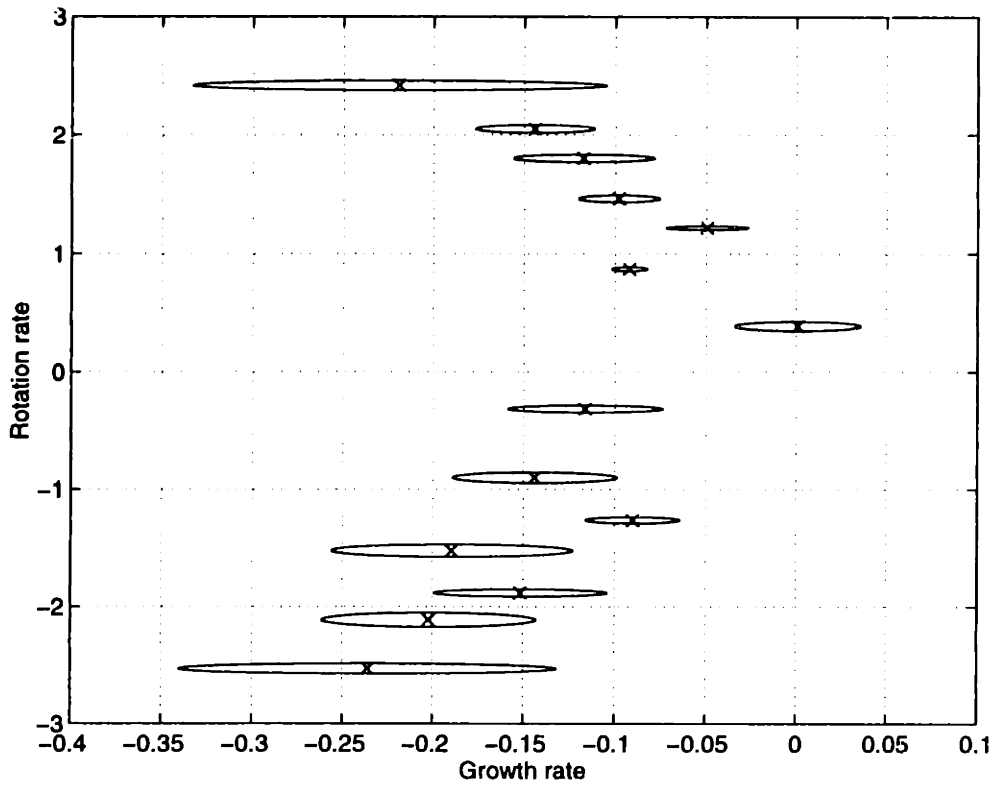

Figure 4-10: Combined uncertainty regions for the time lag constants. The ellipses enclose the region of 95% confidence on the eigenvalues (× are the nominal eigenvalues for the 11 stage at design speed, inlet Mach number of 0.438)

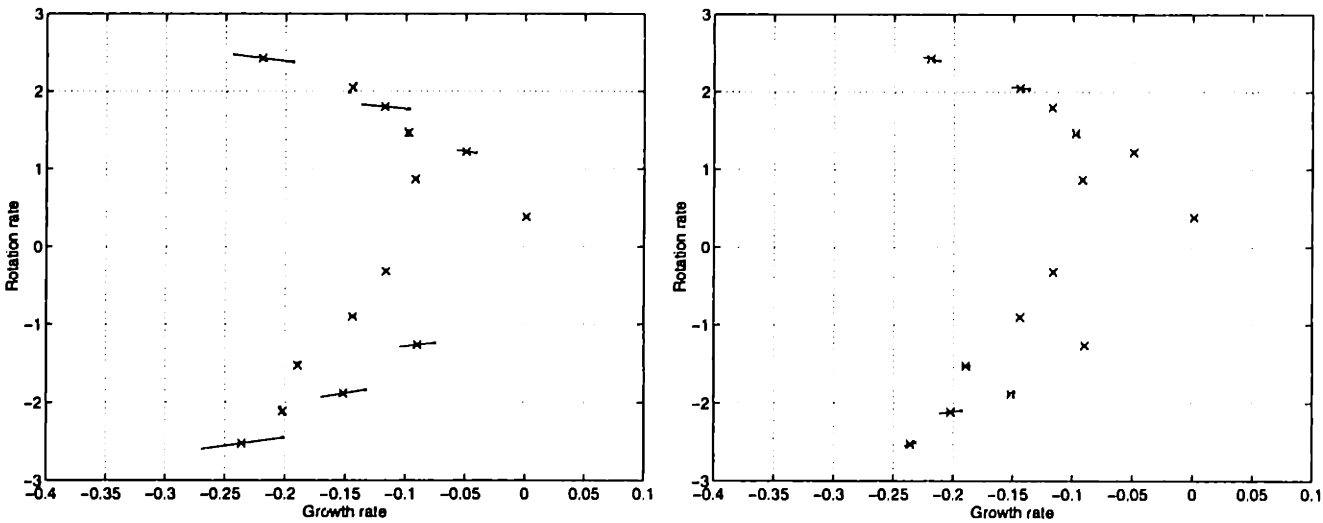

(a) Effect of inlet boundary condition location

(b) Effect of exit boundary condition location

Figure 4-11: Uncertainty regions for the inlet and exit boundary condition locations. The ellipses enclose the region of 95% confidence on the eigenvalues (× are the nominal eigenvalues for the 11 stage at design speed, inlet Mach number of 0.438)

4.5 Effect of blade row modeling errors

Uncertainties on the prediction are not only due to input errors but also to the errors introduced by the calculations and modeling procedure. As described in Chapter 2, the compressible stability model considers the blade rows as 1D inviscid ducts at the stagger angle with actuator disks at the leading edge and trailing edge. The effects of uncertainties on the actuator disk parameters (slopes, ω_l', $\delta°$, ...) have been assessed in the previous sections, but the 1D inviscid duct parameters have not been considered. These parameters are the 1D mean flow in the blade passages and its inclination, which is nominally chosen to be the stagger angle.

1D duct mean flow

The mean flow in the 1D ducts should ideally be determined from the leading edge and trailing edge actuator disk relations. However, since all the loss is modeled to occur at the leading edge, the mean flow in the 1D duct will differ by a bias error from the actual blade passage mean flow. This has the effect of changing the density of the fluid in the modeled blade passage. The effective area in the blade passage is another source of modeling error. Assuming a different blockage within the blade passage results in a different velocity along the 1D duct. The effects of these errors are presented in Figure 4-12, where the nominal eigenvalues ($\times$) are plotted along with the eigenvalues for the blade passage density taken as the average across the blade row ($\circ$) and the eigenvalues for blockage increased by 10% ($+$). We note that these errors mostly affect the higher frequency modes, which is expected since the parameters varied (ρ and $\vec{W}$) are acoustic type quantities and not those of the actuator disk.

Stagger angle

Nominally, the angle chosen for the 1D ducts has been the stagger angle. Since the flow enters the blade row at an incidence and exits with deviation, the average flow angle is different from the stagger angle. The effect of these modeling errors is assessed by plotting, in Figure 4-13, the eigenvalues for the nominal case ($\times$) and for the 1D duct inclination

angle chosen to be the average of the leading edge and trailing edge *mean flow angles* (o). The effect is mostly felt by the higher frequency modes, while the [1,0] and [1,2] modes is also slightly affected.

In conclusion to these sensitivity studies, other parameters than the pressure rise and turning characteristics of a blade row are important to model accurately higher frequency modes. The blade row model should therefore be revised along with the method used to determine the 1D duct parameters.

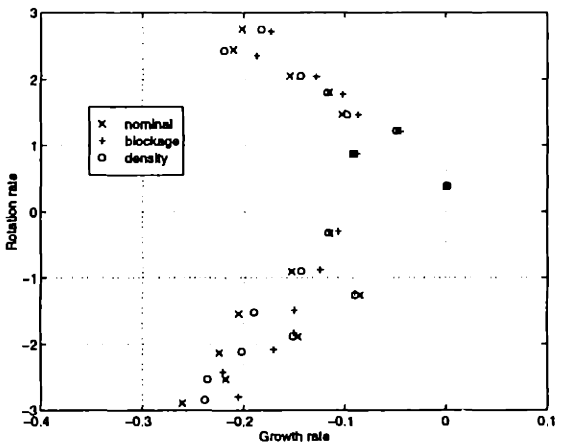

Figure 4-12: Effect of blade passage mean flow. o: blade passage density is the average density, +: blade passage area reduced by 10% ,×: nominal eigenvalues.

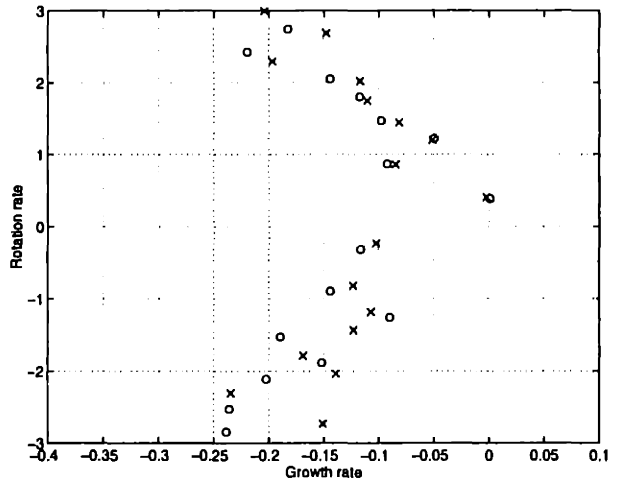

Figure 4-13: Effect of blade passage angle. o: blade passage angle is the average of the relative flow angles ,×: nominal eigenvalues, blade passage angle is the stagger angle.

4.6 Surge margin prediction uncertainty

The uncertainty on the surge margin can be estimated from the uncertainty regions. Since the stability of the 11 stage compressor considered here is given by the [1,0] mode, we will relate uncertainty on surge margin to that of the [1,0] mode eigenvalue.

Since the [1,0] eigenvalue started at neutral stability, the motion of the [1,0] eigenvalue can be compensated by throttling the compressor until neutral stability is regained. The mass flow range corresponding to the eigenvalue motion is given by the [1,0] mode sensitivity to mass flow (or inlet Mach number). From the root locus as a function of mass flow shown in Figure 2-4, the sensitivity of [1,0] mode stability with respect to inlet Mach number can be calculated as:

$$S^{\sigma}_{M_{in}} = \frac{\Delta\sigma_{[1,0]}}{\Delta M_{in}} = -7.6 \tag{4.7}$$

The inlet Mach number uncertainty is estimated by dividing the eigenvalue real part uncertainty by this sensitivity. Table 4.4 presents the stalling mass flow uncertainties (as inlet Mach number uncertainty, ΔM_{in}), broken down into the various sources of error.

Source of uncertainty	$\Delta\sigma_{[1,0]}$	ΔM_{in}	% of total
$\omega_l', \delta^\circ, \bar{k}_1, \bar{k}_2$, bleeds	0.0918	−0.0121	
Slopes	0.0754	−0.0099	
Steady flow	0.1188	−0.0156	74.8%
Lags (τ_p, τ_d)	0.0348	−0.0046	
Boundary Conditions	0	0	
Unsteady flow	0.0348	−0.0046	21.9%
Blade row modeling	0.0053	−0.0007	3.3%
Total	0.1589	−0.0209	100.0%

Table 4.4: Detailed contributions of the input parameter errors on the stall point prediction uncertainty for the 11 stage compressor at design speed.

The last column is the relative contribution of each type on uncertainty. We note that the steady flow uncertainties dominate, followed by the lag uncertainties. The modeling

and boundary condition uncertainties are small for the incompressible mode so they don't contribute much to the total stalling inlet Mach number uncertainty. Figure 4-14 presents this stall point uncertainty on the speedline.

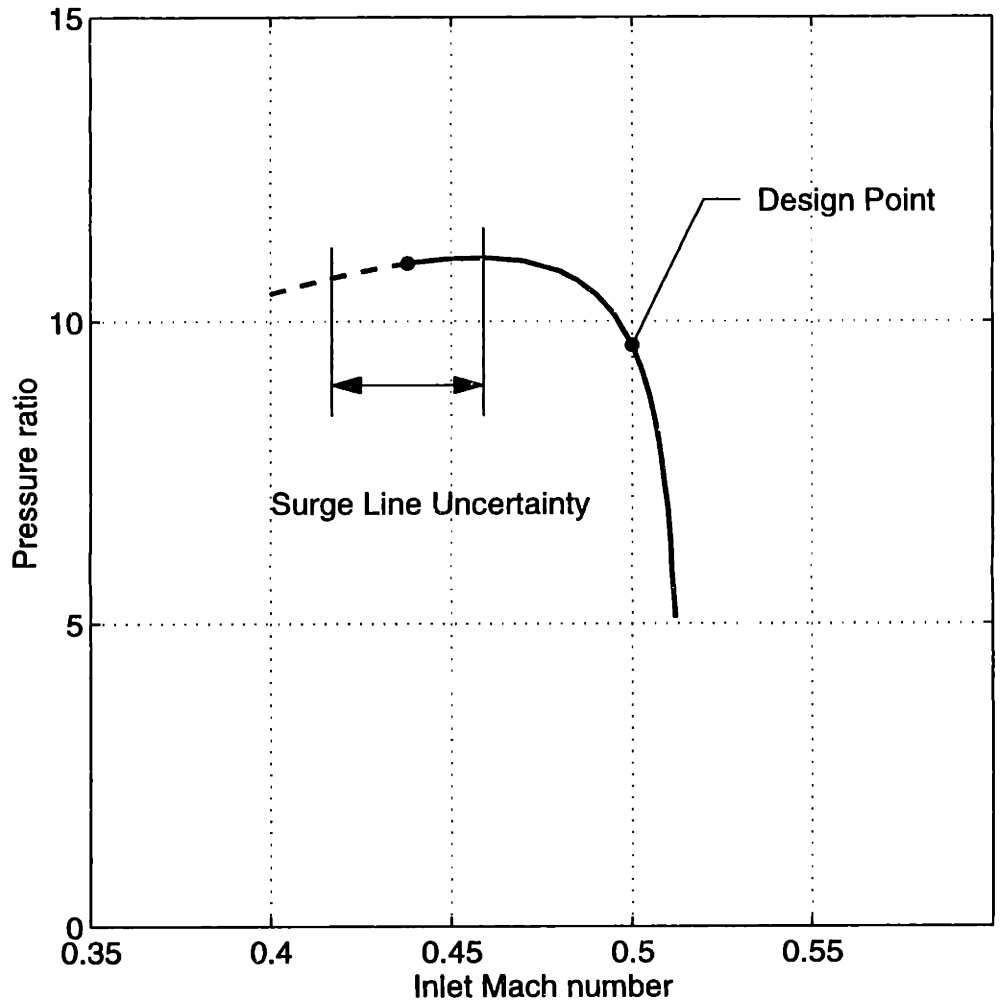

Figure 4-14: Surge line prediction uncertainty for the 11 stage compressor at design speed.

To quantify the uncertainty on *surge margin*, the design point is set at maximum efficiency and the following definition of surge margin is adopted [3]:

$$SM = 1 - \left(\frac{PR_{design}}{PR_{surge}} \times \frac{\mathcal{D}(M_{surge})}{\mathcal{D}(M_{design})} \right) \tag{4.8}$$

where PR is the total pressure ratio across the compressor, and $\mathcal{D}(M)$, the Mach number

function representing mass flow:

$$\mathcal{D}(M) = \frac{M}{\left(1 + \frac{\gamma-1}{2}M^2\right)^{\frac{\gamma+1}{2(\gamma-1)}}} = \frac{\dot{m}\sqrt{T_t}}{AP_t}\sqrt{\frac{R}{\gamma}} \tag{4.9}$$

Table 4.5 shows four operating points of interest: design point, nominal stall point, minimum mass flow stall point (overestimated surge margin) and maximum mass flow stall point (underestimated surge margin). The surge margin is shown in the third column (SM), and the uncertainty on surge margin in the forth column (ΔSM). The surge margin, as defined by Eqn 4.8, is predicted within a total range of 3.6%.

Point	M_{in}	PR	SM	ΔSM
Design	0.500	9.48	–	–
Nominal	0.438	10.88	21.1%	–
overestimated	0.417	10.64	22.4%	1.3%
underestimated	0.460	10.97	18.8%	−2.3%

Table 4.5: Surge margin prediction uncertainty for the 11 stage compressor at design speed.

4.7 Summary of most important parameters for stability prediction and discussion

The main source of prediction uncertainty is the steady flow input errors, contributing 75% of the overall surge margin uncertainty. The loss, deviation and blockage empiricism used to characterize the performance of the compressor introduce errors through their values and their slopes. Completely removing these errors would reduce the surge margin prediction uncertainty from a total range of 3.6% to ≈1%. Removing the errors on the time lag constants practically nullifies the surge margin prediction uncertainty. The modeling errors then limit the prediction accuracy.

Steady flow input errors

Two approaches can reduce the effect of steady flow parameter errors. The first, is to improve the knowledge of these parameters. Figure 4-15 presents the relative contributions of values of the slopes, loss, deviation, blockage, and bleed. The most important parameter is the loss coefficient, because its value and slopes sum to 52% of the uncertainty due to the steady flow parameters. Blockage is then shown to be of relatively similar importance then deviation, with 23% and 20% respectively. Finally, the bleed contributes 5% of the prediction uncertainty. Reducing the error on the losses is most important, but improvements in the knowledge of the other parameters is also desirable.

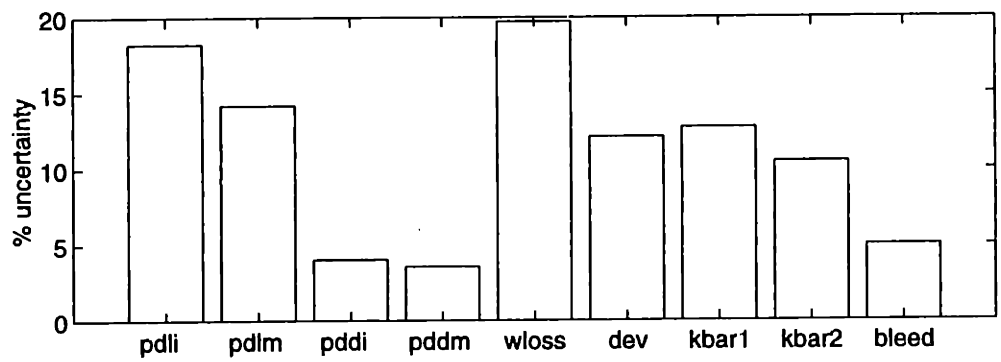

Figure 4-15: Relative contributions of the steady flow parameters on surge line prediction uncertainty for the 11 stage compressor at design speed.

The second approach to reduce the effect of steady flow input errors is to *remove* these

parameters as inputs. If the loss, deviation and blockage phenomena could be taken into account without the use of their respective mean-line coefficients, the prediction uncertainty due to errors on these coefficients would be removed. The alternate method for including the loss, deviation and blockage phenomena would however introduce new prediction uncertainties. If the new uncertainties are less then those related to the mean-line coefficients, the uncertainty on the surge margin prediction would be reduced.

Therefore, both more detailed models and better knowledge of the steady flow parameters are desired for respective uses in accurate surge line prediction and design optimization for enhanced stability.

Time lag constants

The time lag constant for losses also limits the prediction confidence, contributing 22% of the total surge margin uncertainty. The time lag constant for deviation did not, however, contribute much to prediction uncertainty even though the input error was relatively large. One reason for this insensitivity is the small magnitude of the deviation slopes which it lags. The deviations in the 11 stage compressor do not vary much with operating conditions, leading to small deviation slopes. The surge margin prediction of a compressor with larger deviation slopes would be more sensitive to the time lag constant of deviation. A better knowledge of these parameters would be desirable and would improve the prediction accuracy.

Boundary conditions

Error on the boundary conditions is not an important parameter for low-speed compressors and high-speed compressors limited by the [1,0] mode. Compressors exhibiting a least stable higher frequency mode would be sensitive to the upstream and downstream components and the distance from the compressor. The boundary conditions then become important.

With these major input errors eliminated, the issue limiting the absolute prediction accuracy of the surge line would then be the validity of the constitutive relations modeling the instability inception phenomena.

Blade row model

The mean flow and geometry were shown to be mostly important for high frequency modes, similar to the boundary conditions. The same comments therefore apply.

Improved constitutive relations: include blockage?

A parameter not yet included in stability models is the sensitivity of *blockage* to flow field perturbations. Blockage changes the static pressure rise and the ratio of axial velocities across a blade row, therefore influencing the disturbance-power of the blade row and the overall stability. Leading edge blockage also changes the incidence to the blade row (by changing the axial velocity), thus affecting its loading (pressure rise, slopes, ...). This sensitivity is shown by the relatively large uncertainty regions for blockage in Figure 4-4 (c) and (d) (p. 90). As an initial investigation, blockage could be included in the incompressible model developed in Appendix A. This expanded formulation of the Moore-Greitzer model includes blockage, but currently assumes it to be constant with operating conditions. Re-linearizing the pressure rise relation with blockage perturbations would introduce the slopes of blockage (similar to the slopes of loss and deviation). A similar approach could also be applied in *2DCompSIM*, re-linearizing the continuity equations at the leading edge and trailing edge, and introducing the slopes:

$$\frac{\partial \bar{k}}{\partial inc} \text{ and } \frac{\partial \bar{k}}{\partial inc} \tag{4.10}$$

Blockage sensitivity may improve the physical accuracy of the model, but also introduce extra uncertainties on the eigenvalue prediction through the error on the blockage slopes. The effect of blockage in compressor models and the sensitivity of blockage to operating conditions would require further investigation.

Finally, even though the input uncertainties would be reduced, the assessment of the stability modeling tool for surge margin prediction would not be complete until the modeling results are compared with experimental results. This first step was however useful to separate the importance of input errors from the modeling errors.

Chapter 5

Compressor Design Issues for Enhanced Stability

Through the previous chapters, we have presented tools for the prediction and understanding of pre-stall dynamics of a compressor given its design parameters: stability models, energy-based analysis and sensitivity analysis. We can now focus on the use of these tools for designing compressors with enhanced stability. Classic methods such as bleeds, variable vane angle setting and casing treatment could be directly analyzed with these tools, but due to resource constraints, this study we will focus on understanding only the most basic design parameters such as blade row loss and turning, and propose various stabilizing strategies. After presenting an overall methodology for improving compressor stability through modeling, the specific effects of compressor design parameters on blade row disturbance-power and stability are discussed. The last section applies these concepts in a preliminary manner towards the redesign of the 11 stage high-speed compressor for enhanced stability.

5.1 Methodology for improving compressor stability

A methodology for improving the stall margin of a compressor could consist of the following steps:

1. Calculate the pre-stall dynamics near stall. This requires executing the procedure presented in Figure 2-3 (p. 40).
2. Identify the critical modes that limit the operating range.
3. Identify the most sensitive blade rows for these modes and the proper modifications:
   - Calculate the stability sensitivity of the critical modes with respect to changes in blade row design parameters (sensitivity analysis)
   - Analyze the blade row disturbance-power for each critical mode (energy-based analysis)
4. Redesign the compressor within these guidelines.

These steps are repeated until the the stability objective is attained, if possible. As mentioned in Chapter 1, these steps are part of an overall compressor design process, where the compressor designer must meet many goals and is limited by various constraints. The proposed modifications for enhanced stability should therefore respect these limitations and not ignore other design requirements, such as delivered pressure rise, mass flow capability and efficiency. Although this exceeds the scope of this thesis, performance considerations will be kept in mind while redesigning the compressor in Section 5.3.

The first two steps of the redesign process have been done in Chapter 2. The root locus of the 11 stage compressor at design speed was shown in Figure 2-4 and the critical modes listed in Table 2.1. The critical modes were found to be, in decreasing order of importance: the [1,0], [2,0] and [1,2] modes. For simplicity, only the first circumferential harmonic will be considered, focusing on the [1,0] and [1,2] modes. The key element in the process is the third step. Before undertaking this step, we will describe the effects of varying the design parameters on stability and disturbance-power to understand the impacts of design parameter modifications.

5.2 Effect of compressor design parameters on stability

Changing the compressor design parameters can modify the pre-stall dynamics in two ways:

1. changing the mean flow (steady background flow and blade row characteristics);
2. changing the structure of the pre-stall flow field (mode shapes).

The geometry and blade row performance parameters (loss, blockage, deviation, and bleeds) have both effects, modifying the mean flow of the downstream blade rows and the pre-stall mode shapes. They directly link the steady performance of the compressor with its pre-stall dynamics.

The slopes, lags and boundary conditions however do not affect the steady background flow field and will only change the system stability (i.e. the disturbance-power of the blade rows) by modifying the phase and magnitude of the pre-stall modes, i.e. by changing the mode shapes. These parameters somewhat decouple the steady performance from the pre-stall dynamics[1].

Each one of these parameters will be analyzed in more detail in the following sections. The focus is to identify and explain the effects of changing design parameter on stability.

The sensitivity analysis described in Section 4.2 will be used to quantify magnitudes and define these trends, while the disturbance-energy analysis presented in Chapter 3 will allow the explanation of these trends. In this analysis, the inlet mass flow and rotation speed will be considered constant as the various parameters are changed. In this exercise, we will neglect changes in operating point due to the different compressor map and the matching between the compressor and the other components, limiting the scope of this study.

5.2.1 Values of loss, deviation, blockage and bleed

Perturbing the values of loss, deviation, leading edge blockage, trailing edge blockage and bleed for each blade row individually leads to the sensitivity coefficients through the sen-

[1]The dynamics are not completely decoupled from the steady performance. For example, the slopes come from the shape of the steady blade row characteristics and the lags depend on the local aerodynamics of the blade rows

sitivity analysis. The stability sensitivity of the [1,0] and [1,2] modes are shown in Figure 5-1 (p. 115).

The first effect of changing a blade row performance parameter is to modify the characteristic of the blade row and therefore its disturbance-power. Stronger effects are however seen by the blade rows downstream and upstream of the one modified.

Downstream effect

We note that changes in the front blade rows have a larger impact than the back rows, for all five parameters. *This results from the downstream propagating impact of changing the characteristics of a blade row.* The downstream effects are of two types: incompressible and compressible. The *incompressible effect* is the change in velocity triangles with unchanged axial velocity. If the sensitivity of deviation with respect to incidence is small, this impact should not propagate far downstream, and therefore only the mean flow of the following few blade rows will be modified.

The *compressible effect* is the change in axial velocity due to changes in density. All the downstream blade rows will be affected, similar to a change of inlet mass flow. The main effect of changing the loss, deviation, blockage or bleed on the downstream blade rows is therefore a change in their inlet flow, similar to changes in operating point along a speedline. From knoledge of the steady flow, the incidence angles increase as the compressor is throttled toward stall. Thus, a change in compressor design parameter that increases the incidences (loading) is most likely to destabilize the compression system. This point is shown in Figure 5-2, where the incidence change is plotted along with the change in blade row disturbance-power for the 11 stage compressor with the deviation of one blade row modified. The third blade row deviation was increased by a small amount and the resulting incidence change of all the blade rows drawn as the dashed line. The bars correspond to the change in blade row disturbance-power due to the deviation modification. Magnitudes have been scaled to better compare the incidence change with the sensitivity coefficients. We note the direct relation between the blade row operating conditions disturbance-power, concluding that the main effect of changing blade row performance parameters on stability is similar to changes in inlet flow for the downstream blade rows.

Upstream effect

Changing the loss, deviation, blockage or bleed of a blade row also has an influence on the disturbance-power of the upstream blade rows. This upstream influence is due to the upstream traveling potential perturbations and to the fact that an entire mode shape is modified by changing the characteristics of one blade row. The blade rows should therefore not be considered individually, but as part of a system (including all the blade rows, the ducts, and the boundary conditions) for the upstream effect to be analyzed.

The upstream effect is illustrated in Figure 5-3 by comparing the change in blade row disturbance-powers of the [1,0] mode for three different situations where we change: 1) the inlet mass flow; 2) the third blade row deviation; and 3) the 11th blade row deviation. We note that changes in blade row disturbance-power for cases 1) and 2) are similar over the entire compressor, and also downstream of the 11th blade row for case 3). Also, the change in disturbance-power upstream of the 11^{th} blade row for case 3) is not zero. This confirms the upstream influence of steady flow performance parameter modifications.

Design issues

From the sensitivity, increases in loss and deviation tend to stabilize. This trend is simply explained, since increasing losses or deviation moves the pressure rise characteristic to lower pressure rise and mass flow. The peak of the characteristic has therefore shifted to a lower mass flow, lowering the stalling mass flow. These are, however, not good parameters to increase since doing so reduces the steady performance of the compressor. The axial distribution of loss, deviation, blockage and bleed can however be analyzed to procure the optimal steady performance and stability. An Illustration of this type of design process will be presented in Section 5.3.

5.2.2 Slopes of loss and deviation

The stability sensitivities of the [1,0] and [1,2] modes with respect to the slopes of loss and deviation are shown in Figure 5-4. These *slopes* have a simpler effect on the system stability than the *values* of these parameters since they do not modify the steady background flow

field. Changing the slopes of a blade impacts stability by directly affecting the disturbance-power of that blade rows. The upstream and downstream effects are minimal since the mode shapes are not largely affected by a slope change of one blade row.

The performance slopes of a given blade row can be shown to directly affect the blade row disturbance-power, weighted by the magnitude of the axial velocity perturbations. As shown by Eqn 3.38, the intensity component of the blade row disturbance-power ($\mathcal{P}_\mathcal{I}$) for incompressible flow varies according to the product of the static-to-static pressure rise slope $\frac{\partial \Psi^{ss}}{\partial \phi}$ and the magnitude of axial velocity perturbation $|\delta V_x|^2$. Appendix A expanded $\frac{\partial \Psi^{ss}}{\partial \phi}$ as a function of the slopes of loss and deviation versus incidence. The blade row disturbance-power in compressible flow should, by analogy, be governed by the amplitude of δV_x and the blade row performance slopes: $\frac{\partial \omega_1'}{\partial inc}$, $\frac{\partial \omega_1'}{\partial M_1'}$, $\frac{\partial dev}{\partial inc}$, and $\frac{\partial dev}{\partial M_1'}$. Similarly, the *sensitivity* of stability to the slopes will also be weighted by the magnitude of the axial velocity perturbations. This dependence is shown in Figure 5-5, where the sensitivity of stability versus $\frac{\partial \omega_1'}{\partial inc}$ for each blade row is plotted (bars) along with the axial velocity perturbation magnitude (line) for the [1,0] and [1,2] modes. We note the direct relation between the amplitude of δV_x and the blade row performance slopes.

Design issues

The sensitivity coefficients suggest that decreasing the slopes versus incidence, $\frac{\partial \omega_1'}{\partial inc}$, $\frac{\partial dev}{\partial inc}$, (as is well known from steady state reasoning) and increasing the slopes versus relative inlet Mach number, $\frac{\partial \omega_1'}{\partial M_1'}$, $\frac{\partial dev}{\partial M_1'}$ will improve stability. Both of these trends result in a decreasing static-to-static pressure rise slope, reducing the disturbance-power and therefore stabilizing the compressor.

These slopes are not common parameters for the compressor designer, so the means of modifying them is not as well documented as the means of modifying the values of loss and deviation. It is shown in literature [3] that blade rows operating at high relative Mach numbers have steeper slopes of loss versus incidence. This increases the blade row disturbance-power and therefore reduces the stability. To reduce the disturbance-power of such a blade row, the designer can either reduce the slope of the loss bucket near stall or make it coincide with a "node" in the axial velocity perturbation mode shape (axial locations

where $|\delta V_x|$ is small). The first, more conventional option can result of course from unloading the blade row (making it operate at a lower incidence) or by a different aerodynamic design flattening the loss bucket. The second option requires a view of the entire compression system. The mode shapes can be modified by changing compressor parameters, such as the axial loading distribution, or by modifying the boundary conditions. This mode shape tailoring is only effective for higher frequency modes since the [1,0] mode is of decaying nature and therefore not affected by the boundary conditions.

The slopes versus Mach number ($\frac{\partial \omega_1'}{\partial M_1'}$, $\frac{\partial\, dev}{\partial M_1'}$) need to be *increased* for improved stability. Since increasing the losses is usually easier then reducing them, mechanisms that do so for small changes in Mach number at off-design conditions (low mass flow, high incidence) may be realizable. High-speed compressors designers therefore have an extra parameter to tailor the pre-stall dynamics.

5.2.3 Loss and deviation time lags

Figure 5-6 presents the stability sensitivity to the time lag constants of loss and deviation for the [1,0] and [1,2] modes.

We first note that larger lags of loss and deviation tend to be stabilizing the compression system, which is in accordance with the incompressible models [31]. The stabilizing mechanism is simply explained using the concept of disturbance-intensity flux. As a velocity perturbation rotates around the annulus, the pressure rise perturbation will lag behind. The pressure perturbation at the exit of the compressor will then be dephased with respect to the velocity perturbation, increasing the phase difference between them. According to the expression of intensity flux (Eqn 3.30) a larger phase difference between δV_x and intensity flux exiting the blade row, $\mathcal{F}_2$. Since the disturbance-power goes as $\mathcal{F}_2 - \mathcal{F}_1$, reducing $\mathcal{F}_2$ reduces the disturbance-power of the blade row. Increasing the lags is therefore stabilizing. The magnitude of this stabilizing effect is proportional to $n\omega\tau$, so higher harmonics and higher frequency modes will be further stabilized by the lags. An illustration of the larger stabilizing effect on higher frequency modes is shown in Figure 4-9 (p. 95). These plots represent the motion of the eigenvalues with a change in the time lag constant, τ. We note the increasing sensitivity of the eigenvalues as we depart from the real axis.

We also note in Figure 5-6 that the lag sensitivity is greater for the front stages than the rear stages. The main effect of the lags is to dephase the perturbations across a blade row. This change in phase will then be seen by the blade rows downstream, affecting their disturbance-power. The stabilizing effect will sum to a larger reduction of blade row disturbance-power for the front blade rows, and therefore to a larger stability improvement.

Design issues

The time lag constants of loss and deviation are defined by the aerodynamic characteristics of the blade row. The time it takes for the total pressure losses due to a change of inflow conditions to reach the trailing edge is a function of the 2-D and 3-D loss mechanisms, such as profile losses, tip leakage losses, casing boundary layers and shock losses. These time responses of loss or deviation are not well understood. Errors on these lags were shown to introduce large uncertainties on the stall margin prediction in Chapter 4. This uncertainty also restricts us from using this unsteady phenomena to our advantage in increasing the stall margin. Establishing the link between blade row aerodynamic design parameters and the loss and deviation lags would enable the designer to consider the stabilizing effect of lags while optimizing the blade row aerodynamic performance. Since the effects of changing these lags was shown to be substantial, further investigation is justified.

5.2.4 Boundary conditions

The boundary conditions are given by the lengths of the upstream and downstream ducts and by the impedance of the components at the end of these ducts.

The stability is affected by the boundary conditions because they determine the axial mode shapes. Figure 5-7 shows how the dynamics change with duct lengths, by comparing the eigenvalues and axial mode shapes for short and long ducts. Plots for the [1,0] and [1,2] mass flow perturbation shape mode are shown. As discussed above, the location of the troughs or nodes relative to the blade rows affects their disturbance-power, so boundary conditions influence stability. We note from the root locus plot that the higher frequency modes are much more sensitive than the [1,0] mode to boundary conditions, which is explained by the decaying nature of the incompressible-like mode. Since the modes of decaying nature

will not be noticeably affected by the boundary conditions, this parameter is not useful in stabilizing these low frequency modes. Higher frequency modes, however, are affected by the boundary conditions, so this parameters can be used for tailoring those dynamics.

Design issues

The boundary conditions are more difficult for the compressor designer to modify than the previous parameters. Upstream and downstream duct lengths cannot be arbitrarily modified, since they are guided by the overall engine configuration and design.

The end impedances could be modified by tailoring the inlet and exit duct areas or inserting components in the flow path that would modify these boundary conditions. For example, high solidity struts would restrict tangential velocity perturbations and impose a different boundary condition. Doing so may change the mode shapes, influencing the blade row disturbance-power and the fluxes of disturbance-enthalpy at the inlet and exit planes of the compression system.

For the compressor designer, the boundary conditions have the advantage of not being directly related to the compressor steady performance, which simplifies the trade-offs of compressor design for enhanced stability and high performance.

An important conclusion at this point is that the boundary conditions used in the model must mimic the engine installation, otherwise, the high frequency mode will not be well represented.

5.2.5 Summary of design parameter effects and implementations

The blade row performance parameters both affect the mean flow (in the downstream blade rows) and the mode shapes. The strongest effect on stability is to change these parameters for the front blade rows, modifying the mean flow seen by all downstream blade rows. Increasing loss and deviation tends to stabilize, but also reduces the steady performance. The sensitivities of steady performance and stability to loss, deviation, and blockage can be used to optimize the axial distribution of these performance parameters (or of loading) for the best combination of surge margin and performance.

The slopes have a stabilizing effect when the loss and deviation characteristics are flattening versus incidence and steepened versus inlet relative Mach number, corresponding to a lower static-to-static pressure rise slope. This is desired at low mass flow, high incidence conditions.

Actual design modifications that would create changes in loss, deviation, blockage and the slopes include, for example:

- 2D airfoil aerodynamics, since for example, the profile losses versus incidence are determined by the airfoil type [3];
- 3D flows features, such as the PW4000 core compressor redesign [30], where the trailing edge of a few stators were removed to modify the radial distribution of the flow;
- Casing treatment, modifying the tip region blockage and pre-stall behavior [13]
- Tip region blowing with air injectors [47], having a similar overall effect as casing treatment;
- Boundary layer suction [40] or blowing [32], which were shown to modify the stall inception on high-speed and low-speed compressors.

The time lag constants for loss and deviation should be increased for improved stability, especially for the front blade rows. Actual implementation of this effect by blade row design modifications deserves further investigation.

Finally, the boundary conditions would only affect the surge margin if the critical mode is of propagating nature. Methods for affecting the mode shapes by the boundary conditions could be used to stabilize the critical higher frequency mode, and require further investigation.

Design implementations such as these would need to be explored and analyzed with stall inception in mind in order to determine their effectiveness. Stability modeling can however be used to optimize the loading distribution, as will be shown in the next section.

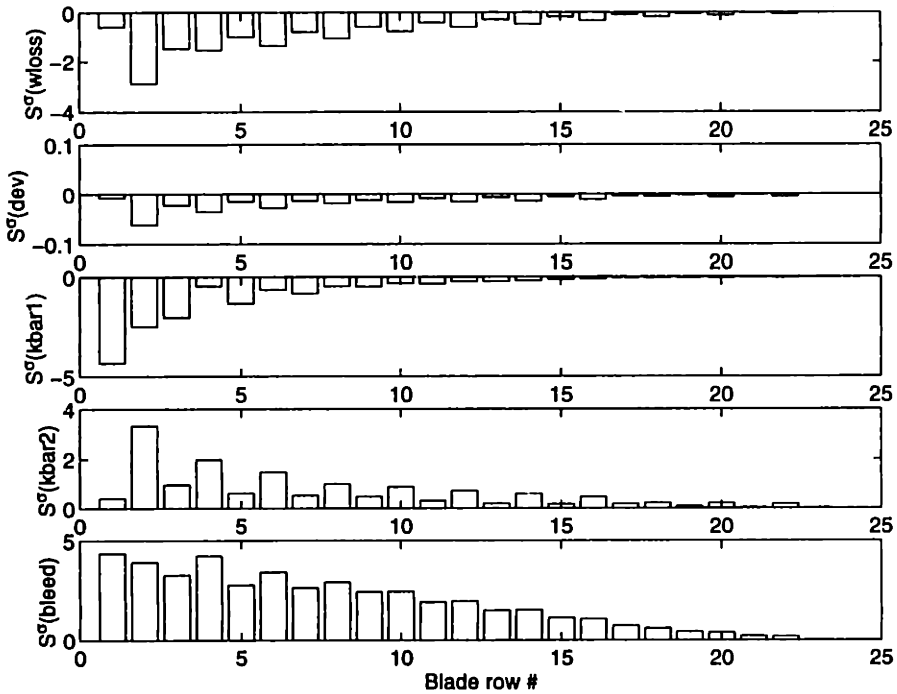

(a) Sensitivity of (1,0) mode stability

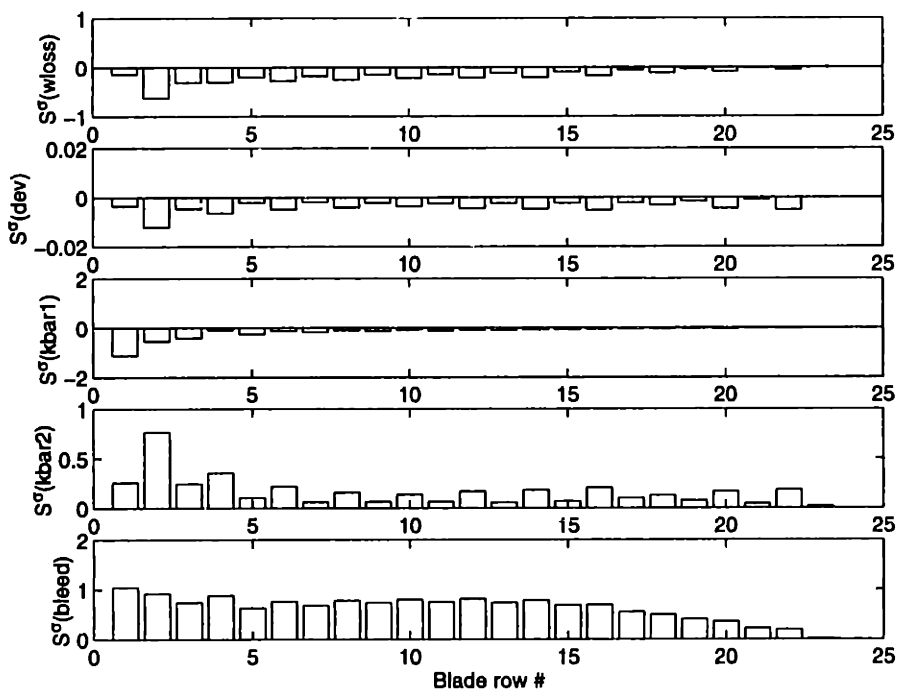

(b) Sensitivity of (1,2) mode stability

Figure 5-1: Sensitivity of stability to the steady flow performance parameters.

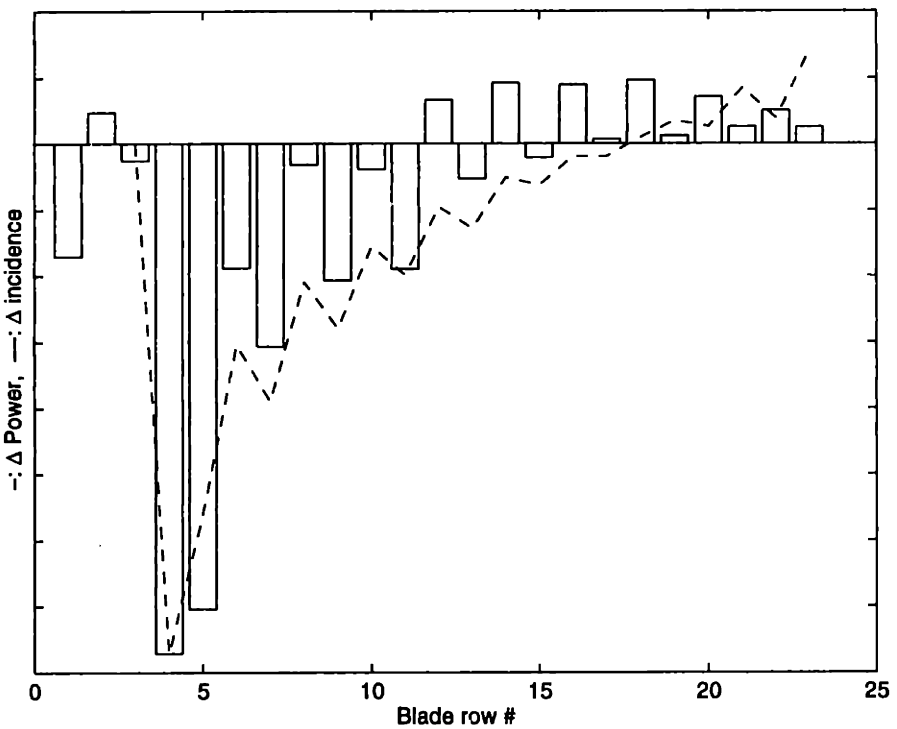

Figure 5-2: Comparison of incidence and blade row disturbance-power change due to an increase in deviation of the 3^{rd} blade row by 1 degree. The bars represent the change in blade row disturbance-power while the dashed line is the change in incidence angle due to the modification of the 3rd blade row. They have been scaled for comparison (11 stage, design speed, $M_{in} = 0.438$, (1,0) mode).

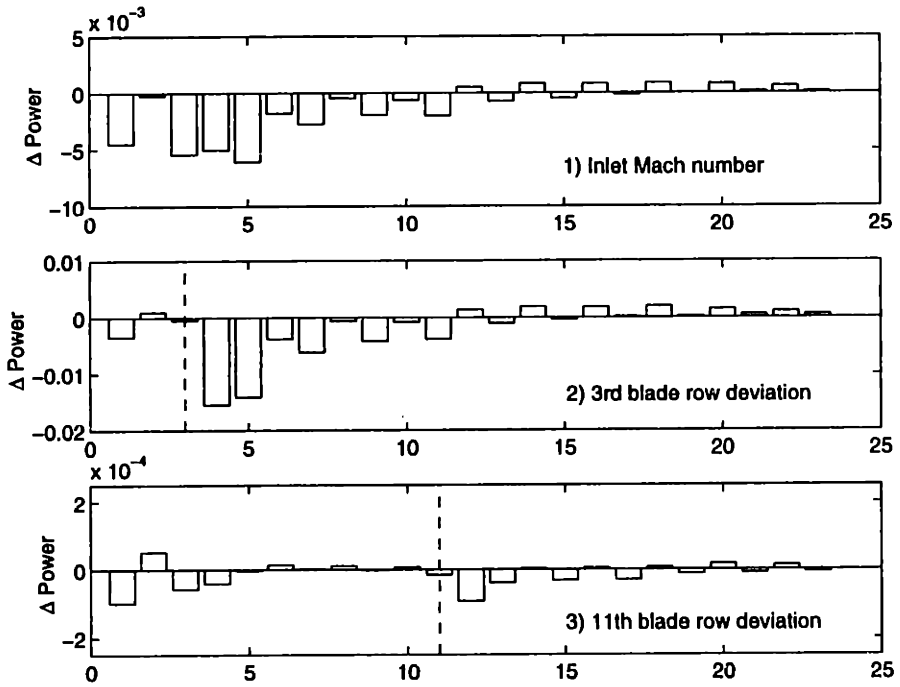

Figure 5-3: Comparison of change in blade row disturbance-power due to three modifications: 1) change inlet Mach number; 2) increase deviation of the 3^{rd} blade row by 1 degree; 3) increase deviation of the 11^{th} blade row by 1 degree (11 stage, design speed, $M_{in} = 0.438$, (1,0) mode).

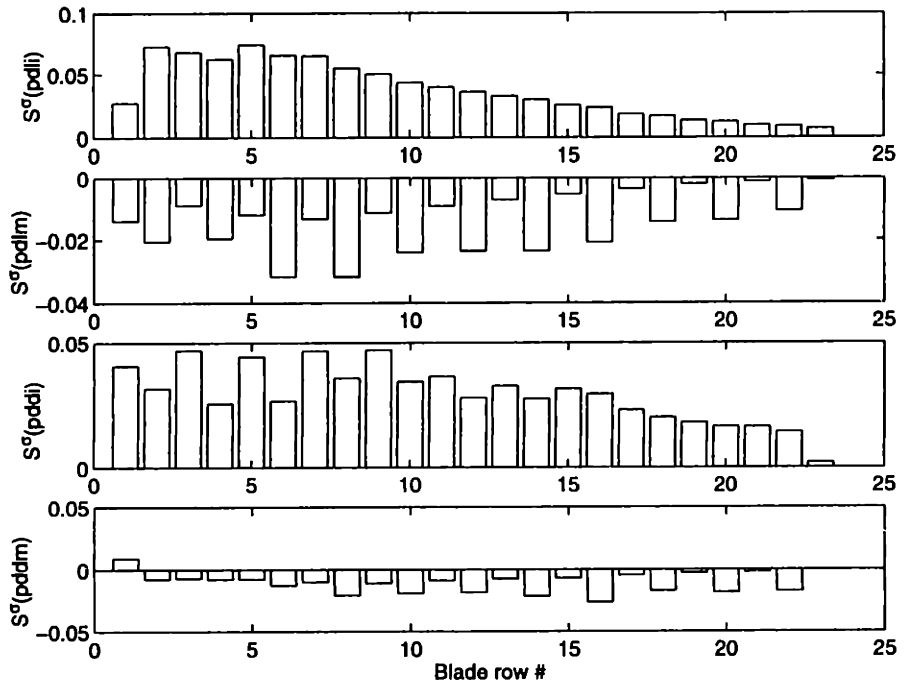

(a) Sensitivity of the (1,0) mode stability

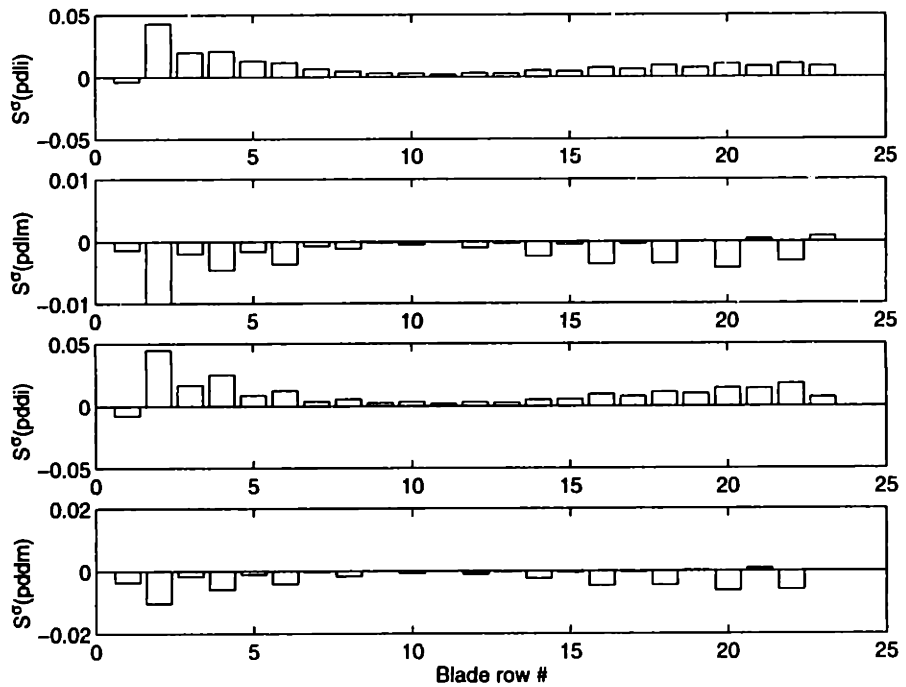

(b) Sensitivity of the (1,2) mode stability

Figure 5-4: Sensitivity of stability to the performance slopes.

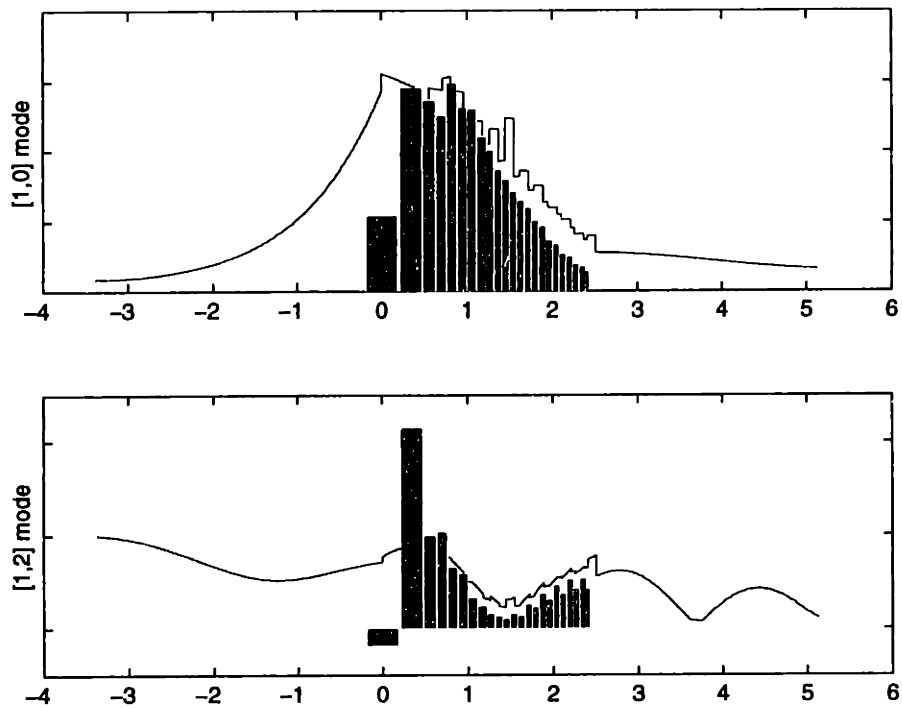

Figure 5-5: Similarity between the axial velocity perturbation amplitude and the sensitivity of stability to the performance slope $\frac{\partial \omega_i'}{\partial inc}$. Scaled for comparison (11 stage, design speed. $M_{in} = 0.438$, (1,0) mode).

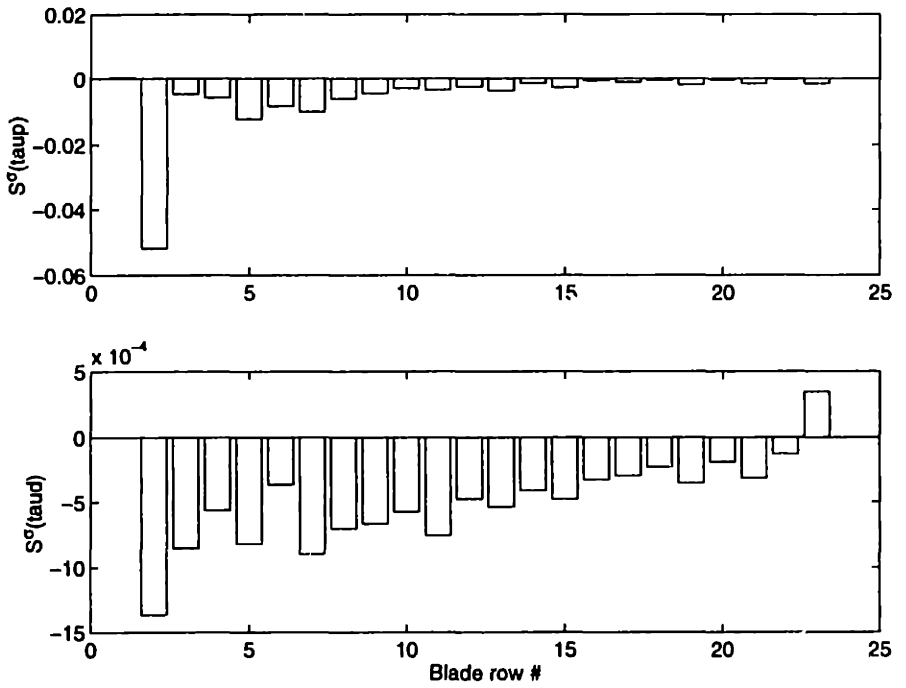

(a) Sensitivity of the (1,0) mode stability

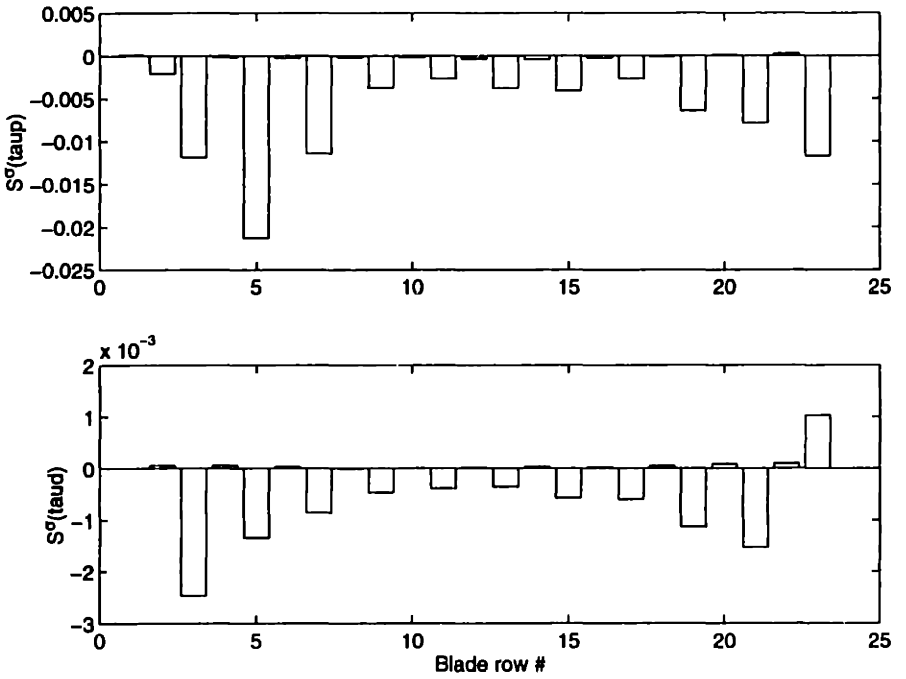

(b) Sensitivity of the (1,2) mode stability

Figure 5-6: Sensitivity of stability to the time lag constants

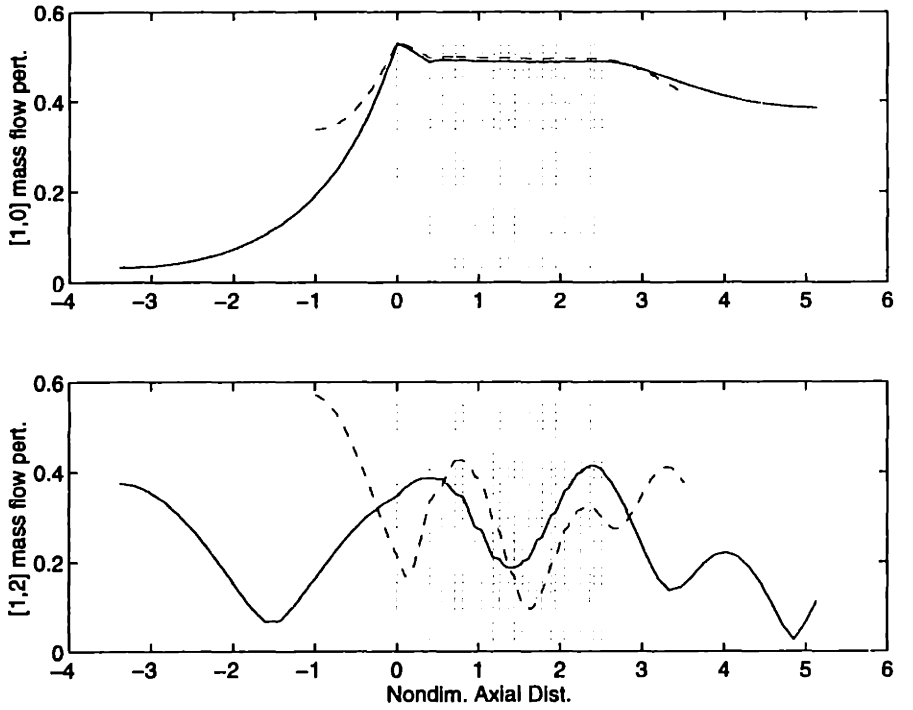

(a) Sensitivity of the mode shape

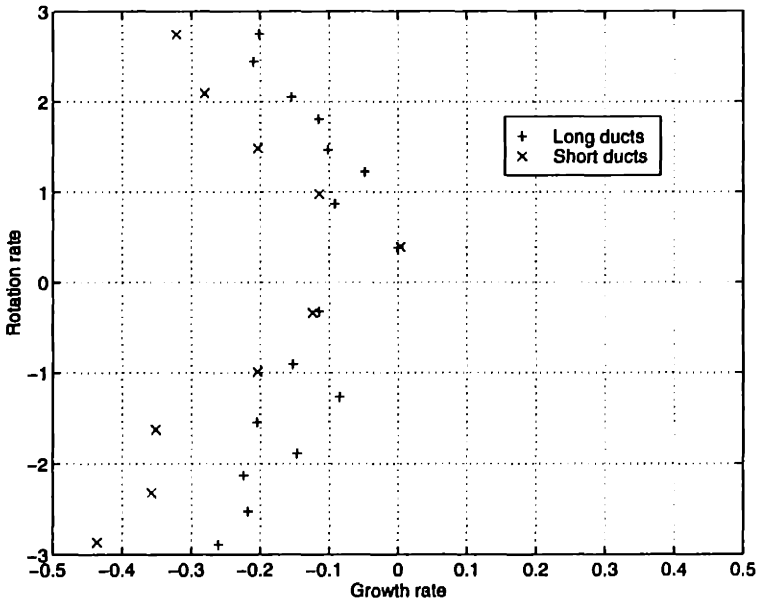

(b) Sensitivity of the eigenvalues

Figure 5-7: Sensitivity of the dynamics to boundary conditions. The locations of the inlet and exit planes are varied to simulate different boundary conditions.

5.3 Illustration of compressor redesign for enhanced stability

The stabilizing mechanisms discussed in the previous sections can be applied during the initial design process of a compressor, or to solve surge margin problems of an existing compressor. Although the actual compressor design modifications that would implement the stabilizing mechanisms still need further investigation, examples of compressor redesign will be presented to illustrate the method and demonstrate the usefulness of stability modeling in high-speed, multi-stage axial compressor design.

The first two redesigns make use of the variable guide vanes (VGV) in the 11 stage compressor. The stagger angle of the inlet guide vanes and following three stators are modified to maximize the surge margin. Since their setting angle is already adjustable, the redesign effort is minimal; it simply demands a re-scheduling of vane opening. The scheduling for the 11 stage compressor is nominally a function of rotor speed, so the first redesign will determine one optimal VGV setting for maximum surge margin at design speed, while maintaining the design point mass flow and pressure rise. The stagger setting is only a function of shaft speed, imposing the same VGV setting along the entire speedline.

The variable geometry could be fully exploited by also scheduling the VGV settings as a function of mass flow, allowing the geometry to be modified for off-design operation without compromising the design point performance. The second redesign explores this possibility by optimizing the VGV setting for maximum surge margin *without* design point constraints. This extra degree of freedom allows the VGV to be reset to their nominal values when the engine is on its operating line.

Finally, a third redesign is proposed which modifies the stagger angles of all 23 blade rows. This type of modification could be applied in the earlier stages of the compressor design to define the optimal loading distribution for desired performance and maximum stability.

5.3.1 Optimization approach

In all the redesigns, the sensitivity analysis method presented in Section 4.2 is used to determine the stability sensitivity of the most critical mode ([1,0]) to changes in stagger

angle for each blade[2]. The stability sensitivity coefficients are defined as the change in the eigenvalue real part per unit change in stagger angle:

$$S_\xi^\sigma = \frac{\Delta\sigma}{\Delta\xi} \tag{5.1}$$

Since the pressure rise is also a concern, the sensitivity of overall total pressure rise (PR) to changes in stagger angle will also be calculated:

$$S_\xi^{PR} = \frac{\Delta PR}{\Delta\xi} \tag{5.2}$$

These sensitivities are calculated by perturbing the stagger angle of each blade row individually and noting the change in pressure ratio (from the steady flow calculation) and in the real part of the [1,0] eigenvalue (from the stability model). Figure 5-8 shows, from top to bottom, the sensitivities of [1,0] mode stability near stall, pressure ratio near stall and pressure ratio at design with respect to stagger angle. The shaded bars correspond to the variable guide vanes.

The surge margin definition used in Chapter 4 is recalled here:

$$SM = 1 - \left(\frac{PR_{des}}{PR_{stall}} \times \frac{\mathcal{D}(M_{stall})}{\mathcal{D}(M_{des})}\right) \tag{4.8}$$

where $\mathcal{D}(M)$ is the Mach number function (Eqn 4.9). Since the design pressure ratio (PR_{des}) and Mach number function ($\mathcal{D}(M_{des})$) are fixed, maximizing the surge margin is equivalent to minimizing the the following ratio:

$$\min\left\{\frac{\mathcal{D}(M_{stall})}{PR_{stall}}\right\} \tag{5.3}$$

As in Section 4.6, the surge margin can be estimated from the sensitivities. First, the change in [1,0] eigenvalue real part and in pressure ratio near stall are estimated from the

[2]A change in stagger angle is considered *positive* when it departs from the axial direction.

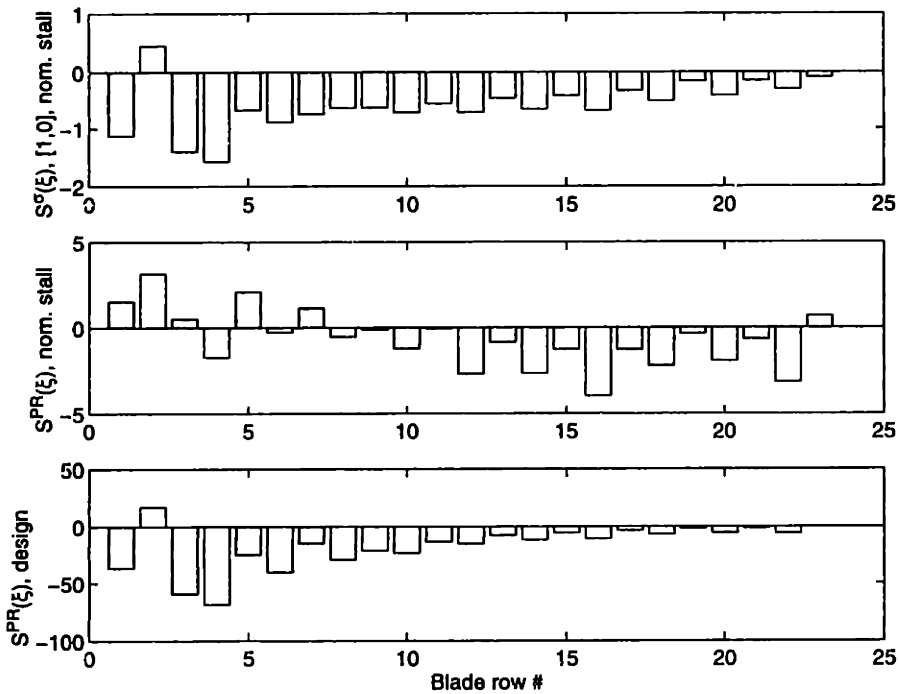

Figure 5-8: Sensitivity coefficients of (1,0) mode stability near stall, pressure ratio near stall and pressure ratio at design with respect to stagger angle.

sensitivities and the changes in stagger angle ($\Delta\xi(k)$) for each blade row, k:

$$\Delta\sigma = \sum_{k=1}^{N} S_{\xi}^{\sigma}(k)\ \Delta\xi(k) \tag{5.4}$$

$$\Delta PR_{stall} = \sum_{k=1}^{N} S_{\xi}^{PR}|_{stall}(k)\ \Delta\xi(k) \tag{5.5}$$

The change in stalling Mach number is then estimated using the sensitivity of $\sigma_{[1,0]}$ to M_{in}:

$$\Delta M_{stall} = \frac{\Delta\sigma}{S_{M_{in}}^{\sigma}} \tag{5.6}$$

Knowing ΔM_{stall} and ΔPR_{stall} along with the nominal M_{stall} and PR_{stall} allows the calculation of the ratio, Eqn 5.3. The optimal combination of $\Delta\xi$ can therefore be estimated.

The first and third redesigns are constrained optimizations, imposing zero change in total pressure ratio at design mass flow:

$$\Delta PR_{des} = \sum_{k=1}^{N} S_{\xi}^{PR}|_{des}(k)\ \Delta\xi(k) = 0 \tag{5.7}$$

The `constr.m` routine from Matlab's Optimization Toolbox was used to optimized the re-staggering with the pressure rise constraint. It implements a methods commonly referred to as Sequential Quadratic Programming (SQP), which iteratively solves a quadratic approximation of the Lagrangian function (see Fletcher [11] for details).

5.3.2 Redesign results

The re-staggering suggested by the optimization with the PR_{des} constraint are presented in Figure 5-9 (a) and (b), for the VGV only (redesign 1) and for all the blade rows (redesign 3), respectively. The optimal stagger settings for maximum surge margin *without* any constraint (redesign 2) is simply the maximum stagger for each VGV since S_ξ^σ are all negative and $S_\xi^{PR}|_{stall}$ are all positive for the VGV.

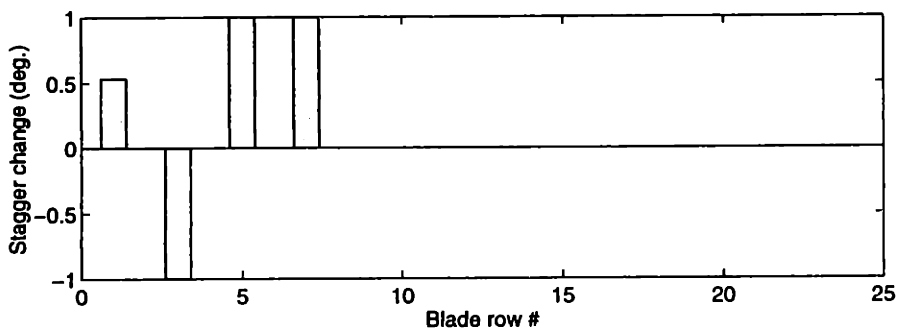

(a) Optimized re-staggering of VGV for redesign 1

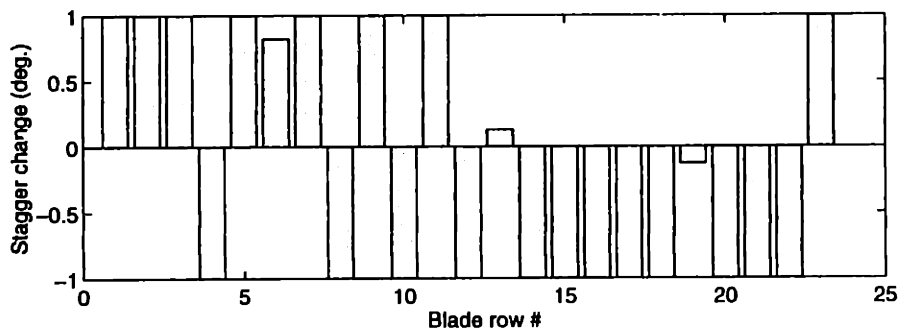

(b) Optimized re-staggering of all rows for redesign 3

Figure 5-9: Optimized re-staggering for maximum surge margin with a constraint on design pressure ratio

The actual changes in stagger angles applied for redesigns 1 and 2 are summarized in Table 5.1, while those for redesign 3 are directly the proposed angles from the optimization (Figure 5-9 (b)). In redesign 1, they slightly differ from those suggested from the optimization in order to exactly recover the design pressure rise. Angles were mostly limited to 5° (for redesigns 1 and 2) and 1° to avoid numerical problems in the calculation. More aggressive modifications would yield greater surge margin enhancement.

	VGV 1	VGV 2	VGV 3	VGV 4
Redesign 1	+5°	−6°	+1.5°	+5°
Redesign 2	+5°	+5°	+5°	+5°

Table 5.1: VGV re-staggering for redesigns 1 and 2

The stalling mass flow and pressure rise for each of the designs are presented in Table 5.2, along with the absolute change in surge margin ($\Delta SM = SM_{redesign} - SM_{nominal}$) and the relative surge margin increase ($\%SM = \frac{SM_{red} - SM_{nom}}{SM_{nom}}$).

	M_{stall}	PR_{stall}	SM	ΔSM	$\%SM$
Design point	0.500	9.48	-	-	-
Nominal design	0.438	10.87	21.2%	-	-
Redesign 1 - VGV w/ PR_{des} constraint	0.428	10.89	22.5%	1.4%	6%
Redesign 2 - VGV w/o PR_{des} constraint	0.399	10.83	26.4%	5.2%	25%
Redesign 3 - All rows w/ PR_{des} constraint	0.442	11.40	24.2%	3.0%	14%

Table 5.2: Surge margin improvements for the three redesigns

The characteristics of the redesigned 11 stage compressors are presented in Figure 5-10, confirming the conservation of the design point for redesigns 1 and 3. The speedline portion plotted for redesign 2 (VGV, unconstrained) is only shown for completeness, since the stagger setting should change as a function of mass flow, blending its speedline with the

nominal one.

The stability modeling tools can therefore be successfully used to design (or redesign) a high-speed multistage compressor with enhanced stability. Useful surge margin increase was obtained with only slight compressor modifications. This redesign exercise was only to demonstrate the method and effectiveness of compressor design using stability models. More aggressive modifications could offer greater surge margin improvement.

Furthermore, the only parameter modified was the stagger angle of the blade rows. Modifying other parameters, such as the loss and deviation characteristics, could also have greater impact. The tool used here for redesign was only the sensitivity analysis of the eigenvalues. The disturbance-power could also be used for more involved redesigns by determining the disturbance-power sensitivity of each blade row to compressor design modifications and comparing it with the pressure rise sensitivity. Various optimizations can be formulated, this section only presenting one of them.

We can conclude that stability modeling offers a method for designing more stable compressors through design modifications that are non-intuitive without these modeling tools.

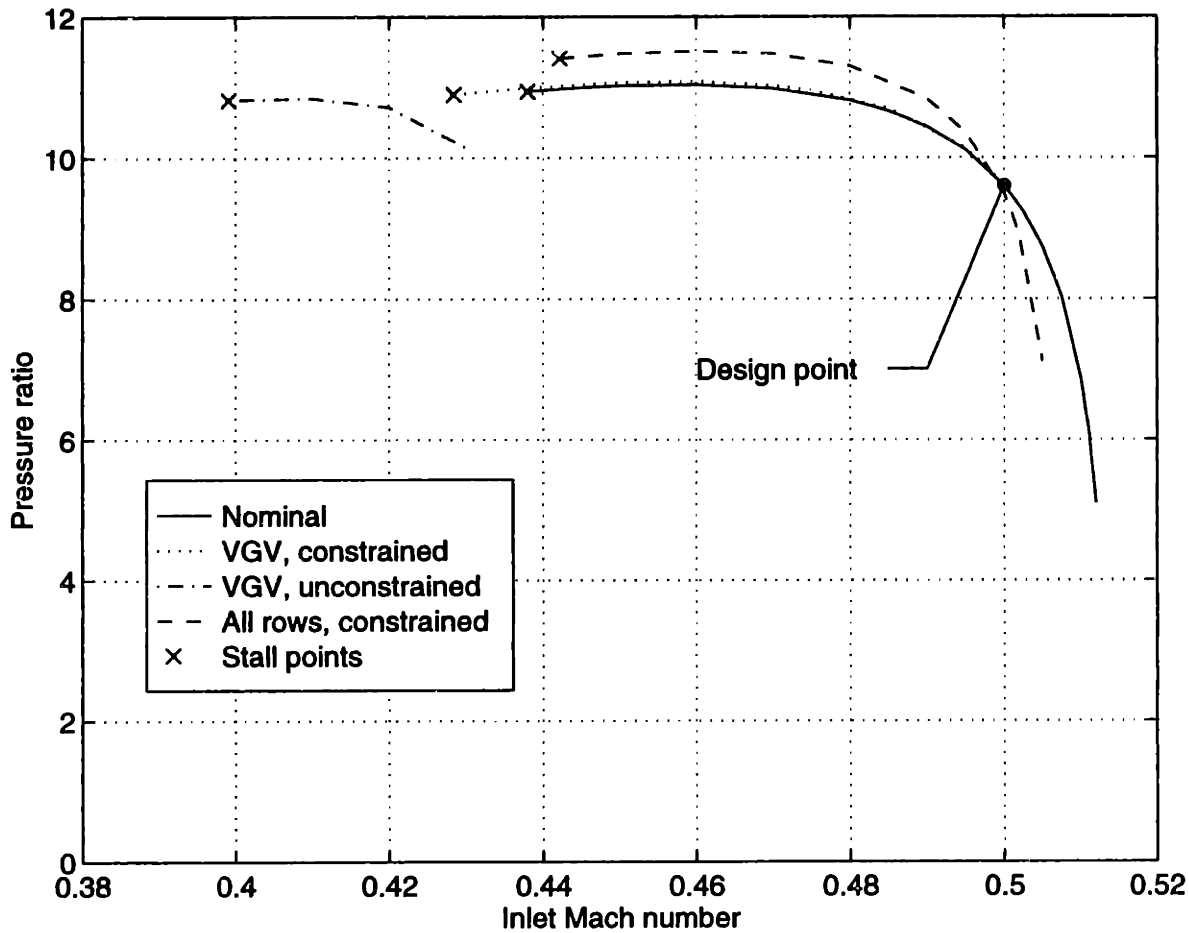

Figure 5-10: Speedlines of the 11 stage compressor redesigns.

CHAPTER 6

CONCLUDING REMARKS

6.1 Summary and Conclusions

A complete methodology for predicting and analyzing the pre-stall fluid dynamics leading to rotating stall and surge inception in high-speed axial compressors has been established and allowed the three main goals of this research to be assessed:

1) Introduce a new tool for understanding compressible modal stall inception

As a first step in understanding the role of the detailed blade row model parameters in the compressible model (*2DCompSIM*) was to formulate an incompressible model including these parameters (*2DIncSIM*).

The main physical features of pre-stall dynamics in high-speed axial compressors have then been described in further detail than previous investigations of this topic (Chapter 2). The various modes predicted by the model are physically understood.

The stability of the pre-stall small amplitude waves was explained from a new energy-based approach in Chapter 3. A corollary describing the transport of energy by these disturbances was presented and applied to low-speed and high-speed compressors. It led to the definition of perturbation quantities describing the stability of the pre-stall waves. Of main interest are the *disturbance-power* of blade rows and *stagnation disturbance-enthalpy* quantities, because the overall compression system stability is defined by the balance between the total

disturbance-power created by all the blade rows and the net flux of stagnation disturbance-enthalpy out of the inlet and exit ducts. This energy-based analysis led to a new view of the role of each blade row on the overall compression system stability. The disturbance-power of a blade row is a function of how it changes the magnitude and phase of the pressure and velocity perturbations across it. A numerical method was established to calculate the blade row disturbance-power for the linearized compressible pre-stall flow field from *2DCompSIM*. An analytical expression was derived for the incompressible rotating stall inception model, proposing how the blade row performance parameters should affect the disturbance-power. This expression is equivalent to the stability criteria from the Moore-Greitzer model.

2) Assess the predictive capabilities of stability models

The compressible model (*2DCompSIM*) was found in Chapter 4 to offer a total uncertainty range on the surge margin prediction of 3.6% (nominal surge margin 21.2%) for an 11 stage high-speed axial compressor representative of modern aircraft core compressors. This uncertainty is due to input parameter errors to the overall stability analysis procedure. The main source of uncertainty on the stall point prediction is the poor knowledge of the steady flow parameters: loss coefficient, deviation, blockage, bleed and the slopes of loss and deviation with respect to incidence and relative Mach number. Removing these uncertainties can reduce the total surge margin prediction uncertainty to less then 1%. The time lag constants for loss are the next most limiting parameters.

The stability modeling procedure is therefore not a very accurate tool for absolute surge line prediction given the current uncertainty of the input parameters, but could become one with more accurate mean flow and time lag constants. Improving the model such that it does not require these performance parameters may eliminate the errors due to these inputs and improve the prediction uncertainty.

Finally, this work has not proven that the adequate modeling assumptions are currently being used. Comparison with experimental data and complex models would complete this predictive capability assessment.

A complete surge line prediction tool should also include a model for the inception of rotating stall through short-length scale phenomena, which has not yet been developed.

3) Illustrate the use of stability modeling in compressor design

The current stability modeling can be used to determine the effect of compressor design modifications on modal stability. The effect of changing compressor design parameters were determined through a sensitivity analysis and explained using disturbance-energy concepts.

The effect of basic **blade row performance parameters** such as loss, deviation and blockage on stability were described mainly as changes in operating conditions (inlet flow) seen by the downstream blade rows. Modifying these parameters such that the downstream blade rows operate at higher loading (incidence) has a destabilizing effect similar to reducing the inlet mass flow. The performance parameters of the front blade rows have a greater impact on stability than the rear blade rows.

The **slopes of loss and deviation** mainly have the effect of directly changing the disturbance-power of the blade row, without affecting much the downstream rows. The compressor is stabilized if the slopes with respect to incidence angle are decreased and the slopes with respect to Mach number increase. Both these trends correspond to a decreasing blade row static-to-static pressure rise characteristic slope.

The stabilizing effect of **time lags of loss and deviation** is explained from an energy point of view, showing that a time lag in the front blade rows has a larger effect than the rear rows. Also, higher frequency modes are more sensitive to these lags.

The **boundary conditions** at the inlet and exit planes of the compression system were shown to only affect the stability (and frequency) of the higher frequency, propagating modes; the fundamental Moore-Greitzer mode not being affected by upstream and downstream impedance modifications. Since the higher frequency modes are largely dependent on the boundary conditions, the ground testing environment may yield different compression system dynamics than the actual compressor embedded in an engine.

Suggestions for compressor redesign to enhance stability were presented, validating the use of stability modeling in the design (or redesign) process of high-speed multistage compressors. Illustrations of design modifications were applied to the 11 stage high-speed compressor, increasing the surge margin. Improvements up to 5.2% in surge margin (representing 25% of the nominal surge margin), were achieved for minor re-staggering of the first four sta-

tors, which already have variable geometry for this compressor. The optimization method used for determining the new stagger settings made use of the sensitivities of stability versus the stagger angle of each blade row, which are given by the stability model. Two redesigns illustrations also constrained the design point pressure rise, using the sensitivities of overall pressure rise versus the stagger angle of each blade row.

Compressors can therefore be designed not only for performance, but also for stability, and the tool to do so is *stability modeling*. As shown, it allows the distributions of loading and other design parameters to be optimized in otherwise non-intuitive ways.

6.2 Recommendations for Future Work

Many issues throughout this work were found to require further research and development for the ultimate goal of implementing stability modeling into industrial compressor design procedures.

Steady flow knowledge

The knowledge of loss, deviation, and blockage parameters and their related slopes should be improved. Trends for modern compressor blade rows (transonic, non-standard airfoil shapes, 3D design) should be well-established and understood. This would not only reduce the uncertainty on the surge line prediction, but would enable the compressor designer to control the loss and deviation values and slopes, and to optimize the blade row aerodynamics for both performance and stability.

Stability model

- **Blockage** - Include blockage perturbations in the incompressible and compressible models and assess the impact of this new performance parameter and its slopes. The change in blockage with operating conditions needs to be investigated in order to determine the slopes of blockage.

- **Short-length scale** - To complete the surge line prediction tool, a model for short-length scale rotating stall inception is necessary. Until then, only the modal stall stability boundary can be predicted.
- **Complete aero-engine model** - Turboprop and helicopter engines often include centrifugal compression stages. An impeller model, similar to the blade row model in *2DCompSIM*, should be developed in order to model this type of component. The potential equation must however be solved for non-uniform mean flow due to the changing radius in impellers and diffusers.

Model validation

In order to use a model with confidence, it should be successfully compared to experimental measurements. The uncertainty on the prediction due to input errors however limits the usefulness of the comparison. A direct validation of the constitutive relations forming the model (without input error) could be achieved by comparing the model with CFD numerical pre-stall behavior [19]. The inputs to the model (mean flow, slopes, time lag constants and boundary conditions) can all be extracted from the CFD calculation, so the prediction error is directly caused by modeling errors.

Blade row model analysis

Along the same lines, the validity of various blade row models (such as actuator disks, semi-actuator disks, body force representations...) can be assessed by comparing their perturbation transmission and reflexion with linearized CFD results (from programs such as Linsub). The figure of merit could be the disturbance-power of the blade row, decomposed into the intensity, kinetic energy, and potential energy components of the disturbance-power.

Disturbance-energy concepts and applications

The concept of disturbance-energy in pre-stall flow fields should be investigated further since it is at the heart of compressor stability. The mechanisms by which a blade row creates disturbance-energy have only been introduced in this thesis. An analytical investi-

gation of blade row disturbance-power for various blade row models would help understand the mechanisms of disturbance-energy creation (or damping), and develop more accurate models.

Experimental measurement of blade row disturbance-power, using both hot-wire measurements and static pressure sensors, would be useful to validate the concept of disturbance-power.

Also, the Disturbance-Energy Corollary and its integrated form could be expanded to 3D and non-linear flow fields. This would allow to qualify and quantify the importance of these new features by comparing the disturbance-powers with simpler representations of the flow field.

Design modifications for enhanced stability

The effects of changing the blade row performance parameters, slopes, lags and boundary conditions on disturbance-power and overall stability have been discussed in Chapter 5, but actual compressor design modifications have not yet been completely linked to these input parameters. A variety of compressor design modification ranging from classic 2D airfoil design, 3D flow pattern tailoring, to boundary layer suction should be investigated with stability in mind, as discussed in Chapter 5. Guidelines for *tailoring compressor dynamics* could then be established.

Experimental applications of stability modeling and disturbance-energy

Experimental uses of stability modeling should also be explored, such as enhanced steady performance measurements, compressor health monitoring and stall warning:

- **Enhanced steady performance measurements** - The direct connection between compressor pre-stall dynamics and steady performance through the losses, deviations and blockage may be used to determine the *steady performance* from *pre-stall unsteady flow field measurements*[1]. The complexity of determining the pressure rise and effi-

[1]Such an application was proposed by Epstein [8] and a first example was shown by Van Schalkwyk in a three stage low-speed compressor ([43], Appendix E).

ciency of individual blade rows embedded into a multistage compressor may therefore be eased.

- **Compressor health monitoring** - Along the same lines, the steady performance of an installed aircraft engine compressor may be monitored by measuring the system dynamic response and comparing it with the model's predictions. Changes in these dynamics can then be related to changes in performance of the various blade rows. The blade row disturbance-power could also be monitored in this fashion, allowing a more detailed health monitoring approach.
- **Stall warning** - A stall inception warning signal based on the expression for disturbance-energy could provide a more complete measure of traveling wave energy then that proposed by Tryfonidis et al. [42]. Measurements of pressure waves and velocity waves would however be required.

Hopefully, this work is only the beginning of the use of stability modeling in the design of modern compressors, and this promising future will become reality within the aircraft gas turbine industry.

APPENDIX A

AXIALLY DISTRIBUTED 2D INCOMPRESSIBLE STALL INCEPTION MODEL (*2DIncSIM*)

In this appendix, the classic 2D, linearized, incompressible rotating stall model is reformulated to make the relative total pressure loss coefficient and the deviation for each blade row appear explicitly. The classic Moore-Greitzer formulation says that the slope of the overall total-to-static pressure rise characteristic is the governing parameter for compressor stability. In order to relate this result to compressor design parameters, the overall pressure rise characteristic will be expanded into the pressure rise of each blade row using relative total pressure loss and deviation characteristics. This formulation also allows for the steady axial velocity and density to vary from blade row to blade row. This new formulation is a step towards a better understanding of the effects of compressor design parameters on stability. It also uses the same input parameters as *2DCompSIM*. Since the steady-state flow is allowed to vary axially, this new formulation may model the incompressible-like mode seen while modeling high speed compressors with a fully compressible stall inception model (Section 2.3).

The first section relaxes a few assumptions from the Moore-Greitzer model and presents a lumped compressor formulation of the overall compression system dynamics that allows for axially varying flow coefficient and density [1]. The second section expands the overall

[1] which is an extension of Longley ([31], Appendix B)

total-to-static pressure rise characteristic into the characteristics of each blade row. The last section addresses the addition of unsteady losses and deviations to each blade row. This model is implemented in the *IncSIM* portion of the *2DSIM Toolbox* described in Appendix B.

A.1 Lumped 2D Incompressible Rotating Stall Model

This section starts by reformulating the classic compressor dynamics equation to allow for changes in the mean axial velocity and density along the axis of the compressor. Inlet swirl sensitivity and deviation of the last blade row are also included. After describing the inlet and exit duct dynamics, the model is assembled to give the stability and rotational frequency of the incompressible pre-stall mode.

A.1.1 Axially distributed compressor dynamics

The classic pressure relation across the compressor[2] and those in the upstream and downstream ducts are reformulated here allowing for changes in axial velocity and density from blade row to blade row.

In this appendix, the mean radius is considered constant and the flow redistribution in the gaps is neglected. The non-dimensionalizing values are:

Length (r_o):	mean radius
Velocity (U_o):	wheel speed (Ωr_o)
Density (ρ_o):	inlet static density
Pressure:	dynamic head based on wheel speed ($\rho_o U_o^2$)
Time:	r_o/U_o

The relations that connect the flow variables across a single blade row are: continuity, deviation and the pressure rise characteristic.

[2]see Moore [34] for the original formulation or Hynes & Greitzer [21] for the formulation using this nomenclature

Continuity

Across a blade row:

$$\rho_1 A_1 V_{x,1} = \rho_2 A_2 V_{x,2}$$
$$\frac{\phi_2}{\phi_1} = \frac{\rho_1 A_1}{\rho_2 A_2}$$

linearizing, without density perturbations:

$$\frac{\delta\phi_2}{\delta\phi_1} = \frac{\rho_1 A_1}{\rho_2 A_2} = c \tag{A.1}$$

where c is defined as the axial velocity ratio across the blade row.

Exit flow angle

The flow exits the blade rows in the relative reference frame at the trailing edge metal angle (κ_2) plus a certain deviation (δ°) angle. Since the blade metal angles are fixed, a perturbation in exit relative flow angle is the same as a perturbation in deviation. Both terms will therefore be used interchangeably.

In general, the deviation is a function of Reynolds number, relative Mach number and relative inlet flow angle (in other words, incidence angle). For low speed blading, the deviation is mainly a function of incidence (see [22] and [3]), so the relative exit flow angle ($\delta \tan\beta_2$)[3] can be expressed as:

$$\delta \tan\beta_2 = \frac{\partial \tan\beta_2}{\partial \tan\beta_1} \delta \tan\beta_1 \tag{A.2}$$

where $\frac{\partial \tan\beta_2}{\partial \tan\beta_1}$ is a characteristic of the blade row, representing the sensitivity of deviation with respect to incidence angle.

[3] $\delta \tan\beta_2$ is used instead of δ° since it will appear directly in the equations. A perturbation in incidence is directly related to a perturbation in tangent of exit flow angle by the exit angles ($\beta_2 = \kappa_2 + \delta^\circ \rightarrow \delta\beta_2 = \delta(\delta^\circ)$) and the derivative of tangent, so: $\delta(\delta^\circ) = \frac{\delta \tan\beta_2}{(1+\tan^2\beta_2)}$

Blade Passage Dynamics

In steady-state, the blade row has a pressure gradient across it which is determined by its turning and viscous losses. A perturbation about this steady pressure gradient will tend the accelerate (or decelerate) the flow in the blade's reference frame proportionally to the blade row fluid inertia. The unsteady pressure rise is then:

$$P_2 - P_1 = (P_2 - P_1)_{steady} - \rho_{br} \times chord \times \frac{\partial W}{\partial t'}$$

where ρ_{br} and W are representative values of density and relative velocity respectively across the blade row. Since W is defined as the relative velocity along the stagger angle, we can write the pressure rise as:

$$\begin{aligned} P_2 - P_1 &= (P_2 - P_1)_{steady} - \rho_{br} \frac{c_x}{\cos^2 \xi} \frac{\partial V_{x,br}}{\partial t'} \\ \frac{P_2 - P_1}{\rho_o {U_o}^2} &= \psi^{ss} - \varrho_{br} \frac{c_x / r_o}{\cos^2 \xi} \frac{\partial \phi_{br}}{\partial \tau'} \end{aligned} \tag{A.3}$$

The blade row density (ρ_{br}) can be chosen as the average of the leading edge and trailing edge densities, or any other representative value.

The blade row axial velocity (ϕ_{br}) can be expressed as a linear function of the leading edge axial velocity:

$$\phi_{br} = I_{br} \times \phi_1 \tag{A.4}$$

where the blade row continuity parameter (I_{br}) can result from choosing ϕ_{br} according to any reasonable modeling assumption. One possibility is to define ϕ_{br} as the average ϕ across the blade row:

$$\begin{aligned} \phi_{br} &= \frac{\phi_1 + \phi_2}{2} \\ &= \phi_1 \left(\frac{1 + \phi_2 / \phi_1}{2} \right) \\ &= \phi_1 \left(\frac{1 + c}{2} \right) \end{aligned}$$

so:

$$I_{br} = \frac{1+c}{2} \tag{A.5}$$

The pressure rise equation becomes:

$$\begin{aligned}\frac{P_2 - P_1}{\rho_o {U_o}^2} &= \psi^{ss} - \varrho \frac{c_x/r_o}{\cos^2 \xi} I_{br} \frac{\partial \phi_1}{\partial \tau'} \\ &= \psi^{ss} - \Lambda_{row} \frac{\partial \phi_1}{\partial \tau'}\end{aligned}$$

which once linearized gives:

$$\frac{\delta P_2 - \delta P_1}{\rho_o {U_o}^2} = \delta\psi^{ss} - \Lambda_{row} \frac{\partial \delta\phi_1}{\partial \tau'} \tag{A.6}$$

where the blade row inertia parameter is:

$$\Lambda_{row} = \varrho \frac{c_x/r_o}{\cos^2 \xi} I_{br} \tag{A.7}$$

For rotors, the time derivative in the relative reference frame is related to that in the absolute reference frame by:

$$\frac{\partial(\cdot)}{\partial t'} = \frac{\partial(\cdot)}{\partial t} + \Omega \frac{\partial(\cdot)}{\partial \theta}$$

and in non-dimensional form[4]:

$$\begin{aligned}\frac{\partial(\cdot)}{\partial \tau'} &= \frac{\partial(\cdot)}{\partial \tau} + \frac{\Omega r_o}{U_o} \frac{\partial(\cdot)}{\partial \theta} \\ \frac{\partial(\cdot)}{\partial \tau'} &= \frac{\partial(\cdot)}{\partial \tau} + \frac{\partial(\cdot)}{\partial \theta}\end{aligned} \tag{A.8}$$

[4]since we chose U_o as the wheel speed, $\frac{\Omega r_o}{U_o}$ is unity

Eqn A.6 for a rotor is then:

$$\boxed{\frac{\delta P_2 - \delta P_1}{\rho_o {U_o}^2} = \delta\psi^{ss} - \Lambda_{row}\frac{\partial\delta\phi_1}{\partial\tau} - \Lambda_{row}\frac{\partial\delta\phi_1}{\partial\theta}} \tag{A.9}$$

and for a stator (or IGV):

$$\boxed{\frac{\delta P_2 - \delta P_1}{\rho_o {U_o}^2} = \delta\psi^{ss} - \Lambda_{row}\frac{\partial\delta\phi_1}{\partial\tau}} \tag{A.10}$$

A.1.2 Inlet duct dynamics

The compressor 2D inlet flow field is considered irrotational ($\nabla \times \vec{V}_{in} = 0$) so the velocity is the gradient of a potential ($\vec{V}_{in} = \nabla\varphi$). Since the flow is also considered incompressible ($\nabla \cdot \vec{V}_{in} = 0$), the upstream duct flow field satisfies Laplace's equation: $\nabla^2\varphi_{in} = 0$ and $\nabla^2\delta\varphi_{in} = 0$. Since the potential must decay upstream, the harmonic expression for the velocity potential perturbation is:

$$\begin{aligned}\delta\varphi_{in}(\chi,\theta,\tau) &= \sum_{n=-\infty}^{n=\infty} \delta\varphi_{in,n} \\ &= \sum_{n=-\infty}^{n=\infty} \bar{\varphi}_{in,n}(\tau)\, e^{|n|\chi}\, e^{jn\theta}\end{aligned} \tag{A.11}$$

By definition of the velocity potential, the non-dimensional axial ($\delta\phi_{in}$) and tangential velocity ($\delta\vartheta_{in}$) perturbations are:

$$\begin{aligned}\delta\phi_{in} &= \frac{\partial}{\partial\chi}(\delta\varphi_{in}) \\ &= |n|\delta\varphi_{in}\end{aligned} \tag{A.12}$$

$$\begin{aligned}\delta\vartheta_{in} &= \frac{\partial}{\partial\theta}(\delta\varphi_{in}) \\ &= jn\delta\varphi_{in}\end{aligned} \tag{A.13}$$

So:

$$\delta\vartheta_{in} = \frac{jn}{|n|}\,\delta\phi_{in} \tag{A.14}$$

Inlet duct flow angle perturbation

Instead of using the tangential velocity, we will use the tangent of the flow angle: $\tan\alpha_{in} = \frac{\vartheta_{in}}{\phi_{in}}$. Linearizing this expression gives:

$$\delta\tan\alpha_{in} = \frac{1}{\bar{\phi}_{in}}\delta\vartheta_{in} - \frac{\bar{\vartheta}_{in}}{\bar{\phi}_{in}^2}\delta\phi_{in}$$

which can be expressed in terms of the axial velocity perturbation ($\delta\phi_{in}$) only using Eqn A.14:

$$\boxed{\delta\tan\alpha_{in} = \left(\frac{jn}{|n|\bar{\phi}_{in}} - \frac{\tan\bar{\alpha}_{in}}{\bar{\phi}_{in}}\right)\delta\phi_{in}} \tag{A.15}$$

Inlet duct momentum equation

The momentum equation for inviscid, irrotational flow is:

$$\frac{\partial\vec{V}_{in}}{\partial t} + \nabla\left(\frac{V_{in}^2}{2}\right) = -\frac{\nabla P_{in}}{\rho_{in}}$$

$$\frac{\partial\nabla\varphi_{in}}{\partial t} = -\frac{\nabla}{\rho_{in}}\left(P_{in} + \frac{\rho V_{in}^2}{2}\right) = -\frac{\nabla P_{t,in}}{\rho_{in}}$$

$$\nabla\left[\frac{\partial\varphi_{in}}{\partial t} + \frac{P_{t,in}}{\rho_{in}}\right] = 0$$

The term between brackets is therefore not a function of space, it remains only a function of time. However, since the perturbations decay far upstream, the term between brackets is actually a constant. For small amplitude perturbations, it can be linearized and written in non-dimensional form as[5]:

$$\frac{\partial\delta\varphi_{in}}{\partial\tau} + \frac{\delta P_{t,in}}{\rho_o {U_o}^2} = 0$$

[5] ρ_o replaces ρ_{in} since the reference density was chosen to be the inlet static density

Finally, using Eqn A.12, the inlet total pressure is:

$$\boxed{\frac{\delta P_{t,in}}{\rho_o {U_o}^2} = -\frac{1}{|n|}\frac{\partial \delta\phi_{in}}{\partial \tau}} \tag{A.16}$$

This equation will be coupled to the compressor dynamics by evaluating it at the leading edge of the first blade row.

A.1.3 Exit duct dynamics

The downstream duct flow field is a combination of vortical and potential disturbances[6]. The potential (or pressure) perturbations decay downstream and have the form:

$$\begin{aligned}\frac{\delta P_{ex}}{\rho_o {U_o}^2} &= \sum_{n=-\infty}^{n=\infty} \frac{\delta P_{ex,n}}{\rho_o {U_o}^2} \\ &= \sum_{n=-\infty}^{n=\infty} \frac{\delta \tilde{P}_{ex,n}}{\rho_o {U_o}^2}(\tau)\, e^{-|n|\chi}\, e^{jn\theta}\end{aligned} \tag{A.17}$$

Exit duct flow angle perturbation

The tangential velocity perturbation can be expressed as a function of the flow angle perturbation using the relations:

$$\bar{\vartheta}_{ex} = \bar{\phi}_{ex} \tan \bar{\alpha}_{ex} \tag{A.18}$$

$$\delta\vartheta_{ex} = \delta\phi_{ex} \tan \bar{\alpha}_{ex} + \bar{\phi}_{ex} \delta \tan \alpha_{ex} \tag{A.19}$$

In general, the exit flow angle of the last blade row is a function of the flow coefficient, the inlet swirl and the wheel speed, so[7]:

$$\delta \tan \alpha_{ex} = \frac{\partial \tan \alpha_{ex}}{\partial \phi_{in}} \delta\phi_{in} + \frac{\partial \tan \alpha_{ex}}{\partial \tan \alpha_{in}} \delta \tan \alpha_{in}$$

[6]For incompressible, uniform flow, the small amplitude perturbations are a combination of potential and vortical modes [28]. For swirling flow, these modes are coupled together [24]. However, since they only interact in the radial momentum equation, the 2D flow perturbations as we are modeling here are formed of uncoupled potential and vortical perturbations.

[7]in this model, the wheel speed is considered to be constant, so $\delta\Omega = 0$

and using the expression for $\delta \tan \alpha_{in}$ (Eqn A.15):

$$\begin{aligned}\delta \tan \alpha_{ex} &= \frac{\partial \tan \alpha_{ex}}{\partial \phi_{in}} \delta \phi_{in} + \frac{\partial \tan \alpha_{ex}}{\partial \tan \alpha_{in}} \left(\frac{jn}{|n| \bar{\phi}_{in}} - \frac{\tan \bar{\alpha}_{in}}{\bar{\phi}_{in}} \right) \delta \phi_{in} \\ &= \left(\left(\frac{\partial \tan \alpha_{ex}}{\partial \phi_{in}} - \frac{\tan \bar{\alpha}_{in}}{\bar{\phi}_{in}} \frac{\partial \tan \alpha_{ex}}{\partial \tan \alpha_{in}} \right) + jn \left(\frac{1}{|n| \bar{\phi}_{in}} \frac{\partial \tan \alpha_{ex}}{\partial \tan \alpha_{in}} \right) \right) \delta \phi_{in}\end{aligned} \tag{A.20}$$

To simplify the algebra, let's write $\delta \tan \alpha_{ex}$ as:

$$\boxed{\delta \tan \alpha_{ex} = (d_{R,ex} + jn\, d_{I,ex})\, \delta \phi_{in}} \tag{A.21}$$

where the overall deviation parameters are:

$$\begin{aligned} d_{R,ex} &= \frac{\partial \tan \alpha_{ex}}{\partial \phi_{in}} - \frac{\tan \bar{\alpha}_{in}}{\bar{\phi}_{in}} \frac{\partial \tan \alpha_{ex}}{\partial \tan \alpha_{in}} \\ d_{I,ex} &= \frac{1}{|n| \bar{\phi}_{in}} \frac{\partial \tan \alpha_{ex}}{\partial \tan \alpha_{in}} \end{aligned} \tag{A.22}$$

Exit duct momentum equation

The axial momentum equation is:

$$-\frac{1}{\varrho_{ex}} \frac{\partial}{\partial \chi} \left(\frac{P_{ex}}{\rho_o {U_o}^2} \right) = \frac{\partial \phi_{ex}}{\partial \tau} + \phi_{ex} \frac{\partial \phi_{ex}}{\partial \chi} + \vartheta_{ex} \frac{\partial \phi_{ex}}{\partial \theta}$$

Assuming that the exit duct has a uniform steady-state flow ($\frac{\partial(\cdot)}{\partial \chi} = \frac{\partial(\cdot)}{\partial \theta} = 0$), the momentum equation can be linearized as:

$$-\frac{1}{\varrho_{ex}} \frac{\partial}{\partial \chi} \left(\frac{\delta P_{ex}}{\rho_o {U_o}^2} \right) = \frac{\partial \delta \phi_{ex}}{\partial \tau} + \bar{\phi}_{ex} \frac{\partial \delta \phi_{ex}}{\partial \chi} + \bar{\vartheta}_{ex} \frac{\partial \delta \phi_{ex}}{\partial \theta} \tag{A.23}$$

The continuity equation is:

$$\begin{aligned} \frac{\partial}{\partial \chi} (\delta \phi_{ex}) &= -\frac{\partial}{\partial \theta} (\delta \vartheta_{ex}) \\ &= -jn \delta \vartheta_{ex} \end{aligned}$$

Substituting the continuity equation into the momentum equation and using the expression for δP_{ex} (Eqn A.17):

$$\frac{|n|}{\varrho_{ex}}\frac{\delta P_{ex}}{\rho_o {U_o}^2} = \frac{\partial \delta\phi_{ex}}{\partial \tau} - jn\bar{\phi}_{ex}(\delta\vartheta_{ex}) + jn\bar{\vartheta}_{ex}(\delta\phi_{ex})$$

replacing the tangential velocity with Eqns A.18 and A.19:

$$\boxed{\frac{\delta P_{ex}}{\rho_o {U_o}^2} = \frac{\varrho_{ex}}{|n|}\frac{\partial \delta\phi_{ex}}{\partial \tau} - \frac{jn}{|n|}\varrho_{ex}\bar{\phi}_{ex}^2(\delta \tan\alpha_{ex})} \tag{A.24}$$

Substituting the expression for $\delta \tan\alpha_{ex}$ (Eqn A.21), we get:

$$\begin{aligned}\frac{\delta P_{ex}}{\rho_o {U_o}^2} &= \frac{\varrho_{ex}}{|n|}\frac{\partial \delta\phi_{ex}}{\partial \tau} - \frac{jn}{|n|}\varrho_{ex}\bar{\phi}_{ex}^2(d_{R,ex} + jnd_{I,ex})\delta\phi_{in} \\ &= \frac{\varrho_{ex}}{|n|}\frac{\partial \delta\phi_{ex}}{\partial \tau} - jn\frac{(\varrho_{ex}\bar{\phi}_{ex}^2\, d_{R,ex})}{|n|}\delta\phi_{in} - |n|(\varrho_{ex}\bar{\phi}_{ex}^2\, d_{I,ex})\delta\phi_{in}\end{aligned} \tag{A.25}$$

A more useful form of this equation would be expressed as a function of the axial flow coefficient at the first blade row's leading edge (ϕ_{in})[8] instead of the exit flow coefficient from the last blade row (ϕ_{ex}). By defining C_{ex} as the axial velocity ratio $\frac{\phi_{ex}}{\phi_{in}}$:

$$\begin{aligned}\bar{\phi}_{ex} &= C_{ex}\,\bar{\phi}_{in} = C_{ex}\,\bar{\phi}_{in} \\ \delta\phi_{ex} &= C_{ex}\,\delta\phi_{in}\end{aligned} \tag{A.26}$$

the exit duct dynamics (Eqn A.25) become:

$$\frac{\delta P_{ex}}{\rho_o {U_o}^2} = \frac{\varrho_{ex}C_{ex}}{|n|}\frac{\partial(\delta\phi_{in})}{\partial \tau} - jn\frac{(\varrho_{ex}C_{ex}^2\bar{\phi}_{in}^2\, d_{R,ex})}{|n|}\delta\phi_{in} + |n|(\varrho_{ex}C_{ex}^2\bar{\phi}_{in}^2\, d_{I,ex})\delta\phi_{in} \tag{A.27}$$

Let's define two useful non-dimensional parameters:

1. *Axial velocity-density ratio*, defined across a blade row (*axdr*), between the k^{th} blade

[8] where ϕ_{in} is the inlet duct flow coefficient evaluated at the leading edge of the first blade row

row leading edge and the inlet ($AVDR(k)$), and across the whole compressor ($AVDR_{ex}$):

$$\begin{aligned} AVDR &= \frac{\rho_2}{\rho_1}\frac{V_{x,2}}{V_{x,1}} = \frac{\rho_2}{\rho_1}\frac{\phi_2}{\phi_1} = \frac{\rho_2}{\rho_1}c \\ AVDR(k) &= \frac{\rho_1(k)}{\rho_{in}}\frac{V_{x,1}(k)}{V_{x,in}} = \frac{\rho_1(k)}{\rho_{in}}\frac{\phi_1(k)}{\phi_{in}} = \varrho(k)C(k) \\ AVDR_{ex} &= \frac{\rho_{ex}}{\rho_{in}}\frac{V_{x,ex}}{V_{x,in}} = \frac{\rho_{ex}}{\rho_{in}}\frac{\phi_{ex}}{\phi_{in}} = \varrho_{ex}C_{ex} \end{aligned} \tag{A.28}$$

2. *Axial momentum ratio*, defined across a blade row (υ), between the k^{th} blade row leading edge and the inlet ($\Upsilon(k)$), and across the whole compressor (Υ_{ex}):

$$\begin{aligned} \upsilon &= \frac{\rho_2}{\rho_1}\left(\frac{V_{x,2}}{V_{x,1}}\right)^2 = \frac{\rho_2}{\rho_1}\left(\frac{\phi_2}{\phi_1}\right)^2 = \frac{\rho_2}{\rho_1}c^2 \\ \Upsilon(k) &= \frac{\rho_1(k)}{\rho_{in}}\left(\frac{V_{x,1}(k)}{V_{x,in}}\right)^2 = \frac{\rho_1(k)}{\rho_{in}}\left(\frac{\phi_1(k)}{\phi_{in}}\right)^2 = \varrho(k)C(k)^2 \\ \Upsilon_{ex} &= \frac{\rho_{ex}}{\rho_{in}}\left(\frac{V_{x,ex}}{V_{x,in}}\right)^2 = \frac{\rho_{ex}}{\rho_{in}}\left(\frac{\phi_{ex}}{\phi_{in}}\right)^2 = \varrho_{ex}C_{ex}^2 \end{aligned} \tag{A.29}$$

Using this nomenclature, the exit duct dynamics (Eqn A.27) become:

$$\boxed{\frac{\delta P_{ex}}{\rho_o {U_o}^2} = \frac{AVDR_{ex}}{|n|}\frac{\partial(\delta\phi_{in})}{\partial\tau} - jn\frac{(\Upsilon_{ex}\bar{\phi}_{in}^2\, d_{R,ex})}{|n|}\delta\phi_{in} + |n|(\Upsilon_{ex}\bar{\phi}_{in}^2\, d_{I,ex})\delta\phi_{in}} \tag{A.30}$$

Finally, expanding out the $d_{R,ex}$ and $d_{I,ex}$ terms:

$$\frac{\delta P_{ex}}{\rho_o {U_o}^2} = \left[\frac{AVDR_{ex}}{|n|}\frac{\partial}{\partial\tau} - jn\frac{\Upsilon_{ex}\bar{\phi}_{in}^2}{|n|}\left(\frac{\partial\tan\alpha_{ex}}{\partial\phi_{in}} - \frac{\tan\bar{\alpha}_{in}}{\bar{\phi}_{in}}\frac{\partial\tan\alpha_{ex}}{\partial\tan\alpha_{in}}\right) + \Upsilon_{ex}\left(\bar{\phi}_{in}\frac{\partial\tan\alpha_{ex}}{\partial\tan\alpha_{in}}\right)\right]\delta\phi_{in} \tag{A.31}$$

This equation will be coupled to the compressor dynamics by evaluating it at the trailing edge of the last blade row.

A.1.4 Overall compression system dynamics

Combined blade row dynamics

A single equation for the dynamics of all the blade rows combined can be expressed by summing the pressure rises across all the blade rows. To do so, all the leading edge axial flow coefficients (ϕ_1) can be expressed as a function of the inlet axial flow coefficient at the leading edge of the first blade row (ϕ_{in}), which will be our reference flow coefficient and simply be denoted as ϕ from now on.

The axial flow coefficient at the leading edge of the k^{th} blade row is defined using the axial velocity ratios of the previous blade rows (Eqn A.1):

$$\begin{aligned}\phi_1(k) &= \frac{\phi_2}{\phi_1}(k-1)\,\frac{\phi_2}{\phi_1}(k-2)\ldots\frac{\phi_2}{\phi_1}(1)\,\phi_{in} \\ &= \prod_{i=1}^{k-1} c(i)\,\phi_{in} \\ &= C(k)\,\phi_{in}\end{aligned}$$

dropping the subscript on ϕ_{in}:

$$\phi_1(k) = C(k)\,\phi \tag{A.32}$$

The combined blade row dynamics are then the sum of the rotor (Eqn A.9) and stator (Eqn A.10) pressure rises, resulting in:

$$\boxed{\frac{\delta P_{ex} - \delta P_{in}}{\rho_o {U_o}^2} = \delta\Psi^{ss} - \mu\frac{\partial\delta\phi}{\partial\tau} - \lambda\frac{\partial\delta\phi}{\partial\theta}} \tag{A.33}$$

where:

$$\delta\Psi^{ss} = \sum_{\text{all rows}} \delta\psi^{ss} = \sum_{\text{all rows}} \left.\frac{\delta P_2 - \delta P_1}{\rho_o {U_o}^2}\right|_{steady} \tag{A.34}$$

$$\mu = \sum_{\text{all rows}} \Lambda_{row} \times C = \sum_{\text{all rows}} \varrho \frac{c_x/r_o}{\cos^2 \xi} I_{br}\, C \tag{A.35}$$

$$\lambda = \sum_{\text{rotors}} \Lambda_{row} \times C = \sum_{\text{rotors}} \varrho \frac{c_x/r_o}{\cos^2 \xi} I_{br}\, C \tag{A.36}$$

Subtracting an inlet dynamic head on both sides of Eqn A.33 and using the form of $\delta\phi_{in}$ for the n^{th} harmonic ($\delta\phi_n \propto e^{jn\theta}$) leads to a more useful form:

$$\frac{\delta P_{ex} - \delta P_{t,in}}{\rho_o {U_o}^2} = \delta\Psi^{ts} - \mu \frac{\partial \delta\phi}{\partial \tau} - jn\lambda\delta\phi \tag{A.37}$$

T-S pressure rise perturbation

In general, the steady pressure rise is a function of the flow coefficient, the inlet swirl and the wheel speed, so:

$$\delta\Psi^{ts} = \frac{\partial \Psi^{ts}}{\partial \phi}\delta\phi + \frac{\partial \Psi^{ts}}{\partial \tan\alpha_{in}}\delta\tan\alpha_{in}$$

and using the expression for $\delta\tan\alpha_{in}$ (Eqn A.15):

$$\begin{aligned}\delta\Psi^{ts} &= \frac{\partial \Psi^{ts}}{\partial \phi}\delta\phi + \frac{\partial \Psi^{ts}}{\partial \tan\alpha_{in}}\left(\frac{jn}{|n|\bar{\phi}} - \frac{\tan\bar{\alpha}_{in}}{\bar{\phi}}\right)\delta\phi \\ &= \left[\left(\frac{\partial \Psi^{ts}}{\partial \phi} - \frac{\tan\bar{\alpha}_{in}}{\bar{\phi}}\frac{\partial \Psi^{ts}}{\partial \tan\alpha_{in}}\right) + jn\left(\frac{1}{|n|\bar{\phi}}\frac{\partial \Psi^{ts}}{\partial \tan\alpha_{in}}\right)\right]\delta\phi\end{aligned} \tag{A.38}$$

To simplify the algebra, let's write $\delta\Psi^{ts}$ as:

$$\delta\Psi^{ts} = (TS_R + jn\, TS_I)\, \delta\phi \tag{A.39}$$

where the total-to-static pressure rise parameters are:

$$TS_R = \frac{\partial \Psi^{ts}}{\partial \phi} - \frac{\tan \bar{\alpha}_{in}}{\bar{\phi}_{in}} \frac{\partial \Psi^{ts}}{\partial \tan \alpha_{in}} \tag{A.40}$$

$$TS_I = \frac{1}{|n| \bar{\phi}_{in}} \frac{\partial \Psi^{ts}}{\partial \tan \alpha_{in}} \tag{A.41}$$

Using this relation for $\delta \Psi^{ts}$, the combined blade row dynamics (Eqn A.37) become:

$$\boxed{\frac{\delta P_{ex} - \delta P_{t,in}}{\rho_o {U_o}^2} = (TS_R + jn\, TS_I)\, \delta\phi - \mu \frac{\partial \delta\phi}{\partial \tau} - jn\lambda\delta\phi} \tag{A.42}$$

Overall compression system dynamics

Finally, combining the compressor dynamics (Eqn A.42) with the inlet duct dynamics (Eqn A.16) and the exit duct dynamics (Eqn A.30) leads to:

$$\frac{(AVDR_{ex}+1)}{|n|} \frac{\partial(\delta\phi)}{\partial \tau} - jn \frac{(\Upsilon_{ex} \bar{\phi}^2\, d_{R,ex})}{|n|} \delta\phi + |n|(\Upsilon_{ex} \bar{\phi}^2\, d_{I,ex}) \delta\phi = (TS_R + jn\, TS_I)\, \delta\phi - \mu \frac{\partial(\delta\phi)}{\partial \tau} - jn\lambda\delta\phi$$

Rearranging, we obtain the closed form of the linearized rotating stall compression system dynamics for the n^{th} circumferential harmonic:

$$\left(\frac{(AVDR_{ex}+1)}{|n|} + \mu\right) \frac{\partial(\delta\phi)}{\partial \tau} = \left[\left(TS_R - |n|(\Upsilon_{ex} \bar{\phi}^2\, d_{I,ex})\right) - jn\left(\lambda - TS_I - \frac{(\Upsilon_{ex} \bar{\phi}^2\, d_{R,ex})}{|n|}\right)\right] \delta\phi \tag{A.43}$$

The solution to this differential equation has the form: $e^{s\tau} = e^{(\sigma - jn\omega)\tau}$, where:

$$\sigma = \frac{TS_R - |n| \Upsilon_{ex} \bar{\phi}^2\, d_{I,ex}}{\left(\frac{AVDR_{ex}+1}{|n|} + \mu\right)} \tag{A.44}$$

$$\omega = \frac{\lambda - TS_I - \frac{(\Upsilon_{ex} \bar{\phi}^2\, d_{R,ex})}{|n|}}{\left(\frac{AVDR_{ex}+1}{|n|} + \mu\right)} \tag{A.45}$$

A.2 Expansion of the total-to-static pressure rise

This section expands the overall total-to-static pressure rise into the isentropic pressure rise and total pressure loss across each blade row. An analytical expression for the total-to-static slope will be found as a function of the loss coefficient and exit flow angle (or deviation) of each blade row.

The overall total-to-static pressure rise is:

$$\frac{(P_{ex} - P_{t,in})}{\rho_o {U_o}^2} = \frac{(P_{ex} - P_{in})}{\rho_o {U_o}^2} - \frac{1}{2}\frac{V_{in}^2}{U_o^2}$$

which is linearized as:

$$\delta\Psi^{ts} = \delta\Psi^{ss} - \delta\left(\frac{1}{2}\frac{V_{in}^2}{U_o^2}\right)$$

Since $V_{in} = V_{x,in} \times \sec\alpha_{in}$ and $\sec^2\alpha_{in} = 1 + \tan^2\alpha_{in}$:

$$\begin{aligned}\delta\Psi^{ts} &= \delta\Psi^{ss} - \delta\left(\frac{1}{2}\phi_{in}^2(1 + \tan^2\alpha_{in})\right) \\ &= \delta\Psi^{ss} - \bar{\phi}\delta\phi - \bar{\phi}\tan^2\bar{\alpha}_{in}\delta\phi - \bar{\phi}_{in}^2\tan\bar{\alpha}_{in}\delta\tan\alpha_{in}\end{aligned}$$

and using the expression for $\delta\tan\alpha_{in}$ (Eqn A.15), we get:

$$\delta\Psi^{ts} = \delta\Psi^{ss} - \bar{\phi}\delta\phi - jn\frac{\bar{\phi}\tan\bar{\alpha}_{in}}{|n|}\delta\phi \qquad \text{(A.46)}$$

where $\delta\Psi^{ss}$ is the sum of the pressure rises across each blade row (Eqn A.34).

We wish to decompose the static-to-static pressure rise across a blade row (ψ_{ss}) into the isentropic pressure rise (ψ_{is}^{ss}) from which is subtracted the pressure losses (ψ_{loss}). From the definition of the relative total pressure, we can write across a blade row (at constant

radius):

$$P_2 - P_1 = \frac{1}{2}(\rho_1 V_1'^2 - \rho_2 V_2'^2) + P'_{t,2} - P'_{t,1}$$

$$\frac{P_2 - P_1}{\rho_o {U_o}^2} = \frac{1}{2}\left[\frac{\rho_1}{\rho_o}\left(\frac{V'_1}{U_o}\right)^2 - \frac{\rho_2}{\rho_o}\left(\frac{V'_2}{U_o}\right)^2\right] - \frac{P'_{t,1} - P'_{t,2}}{\rho_o {U_o}^2}$$

or:

$$\boxed{\psi^{ss} = \psi^{ss}_{is} - \psi_{loss}} \tag{A.47}$$

where we define:

$$\boxed{\psi^{ss}_{is} = \frac{1}{2}\left[\frac{\rho_1}{\rho_o}\left(\frac{V'_1}{U_o}\right)^2 - \frac{\rho_2}{\rho_o}\left(\frac{V'_2}{U_o}\right)^2\right]} \tag{A.48}$$

$$\boxed{\psi_{loss} = \frac{P'_{t,1} - P'_{t,2}}{\rho_o {U_o}^2} \text{ (always } > 0)} \tag{A.49}$$

A.2.1 Isentropic pressure rise perturbation

The isentropic pressure rise (Eqn A.48) can be expressed as a function of our variables of interest using the velocity triangle relations ($V'^2 = V_x^2 + V_\theta'^2$ and $V' = V_x/\cos\beta$):

$$\psi^{ss}_{is} = \frac{1}{2}\frac{\rho_1}{\rho_o}\left[\left(\frac{V_{x,1}}{U_o}\right)^2(1 + \tan^2\beta_1) - \frac{\rho_2}{\rho_1}\left(\frac{V_{x,2}}{U_o}\right)^2(1 + \tan^2\beta_2)\right]$$

using our non-dimensional parameters and the relations between the leading edge and trailing edge flow values (Eqns A.1 and A.29)

$$\psi^{ss}_{is} = \frac{\varrho\phi_1^2}{2}\left[\tan^2\beta_1 - \upsilon\tan^2\beta_2 + 1 - \upsilon\right] \tag{A.50}$$

The exit flow angle (β_2) is a function of the blade row performance (deviation characteristic).

Linearization

Since we are not taking density perturbations into account: ϱ = constant. We will also assume as a first approximation that the axial momentum ratio is constant across a blade row:

$$v = \bar{v} = \text{constant} \tag{A.51}$$

The exit flow angle from an blade row is generally a function of leading edge relative Mach number, incidence angle and Reynolds number. For traditional low-speed blading, incidence angle has the major effect on the exit flow angle [22], so we can write the relative exit flow angle perturbation as:

$$\delta \tan \beta_2 = \frac{\partial \tan \beta_2}{\partial \tan \beta_1} \delta \tan \beta_1 \tag{A.52}$$

where $\frac{\partial \tan \beta_2}{\partial \tan \beta_1}$ represents the sensitivity of deviation with respect to incidence angle. This is a performance characteristic of the blade row.

Linearizing Eqn A.50 leads to:

$$\boxed{\delta \psi_{is} = \varrho \bar{\phi}_1 \left[\tan^2 \bar{\beta}_1 - v \tan^2 \bar{\beta}_2 + 1 - v \right] \delta \phi_1 + \frac{\varrho \bar{\phi}_1^2}{2} \left[(2 \tan \bar{\beta}_1) - v (2 \tan \bar{\beta}_2) \frac{\partial \tan \beta_2}{\partial \tan \beta_1} \right] \delta \tan \beta_1} \tag{A.53}$$

A.2.2 Relative total pressure loss perturbation

The viscous losses across a blade row are also a function of blade row performance. They are generally expressed as a function of the relative total pressure loss coefficient [22]:

$$\omega_l' = \frac{P'_{t,2_{is}} - P'_{t,2}}{P'_{t,1} - P_1}$$

which, for incompressible flow at constant radius, can be expressed as:

$$\omega_l' = \frac{P_{t,1}' - P_{t,2}'}{\frac{1}{2}\rho_1 V_1'^2} \tag{A.54}$$

The relative total pressure loss (Eqn A.49) is then:

$$\begin{aligned} \psi_{loss} &= \frac{P_{t,1}' - P_{t,2}'}{\frac{1}{2}\rho_1 V_1'^2} \times \frac{\frac{1}{2}\rho_1 V_1'^2}{\rho_o {U_o}^2} \\ &= \omega_l' \frac{\varrho \phi_1^2}{2}(1 + \tan^2 \beta_1) \end{aligned} \tag{A.55}$$

Linearization

As for the exit flow angle, the loss coefficient (ω_l') is generally a function of leading edge relative Mach number, incidence angle and Reynolds number, but the incidence angle has the major effect [22], so we can write the loss coefficient perturbation as:

$$\delta\omega_l' = \frac{\partial \omega_l'}{\partial \tan\beta_1}\, \delta \tan\beta_1 \tag{A.56}$$

where $\frac{\partial \omega_l'}{\partial \tan\beta_1}$ represents the sensitivity of the losses with respect to incidence angle. This is also a performance characteristic of the blade row.

Therefore, linearizing Eqn A.55 leads to:

$$\boxed{\delta\psi_{loss} = \varrho\bar{\phi}_1\bar{\omega}_l'(1 + \tan^2\bar{\beta}_1)\,\delta\phi_1 + \frac{\varrho\bar{\phi}_1^2}{2}\left[(1 + \tan^2\bar{\beta}_1)\frac{\partial\omega_l'}{\partial\tan\beta_1} + 2\,\bar{\omega}_l'\tan\bar{\beta}_1\right]\delta\tan\beta_1} \tag{A.57}$$

A.2.3 Overall total-to-static pressure rise perturbation

In order to connect the pressure rises across all the blade rows together, forming the overall pressure rise, we must relate the leading edge flow angle perturbation ($\delta\tan\beta_1$) and local axial flow coefficient ($\delta\phi_1$) to the axial flow coefficient at the leading edge of the first blade row ($\delta\phi$).

Axial flow perturbation

As defined in Eqn A.32:

$$\phi_1(k) = C(k)\ \phi$$
$$\delta\phi_1(k) = C(k)\ \delta\phi$$

Leading edge relative flow angle perturbation

Using the velocity triangle relations[9]:

$$\tan\beta = \tan\alpha - \frac{\Omega_{nd}}{\phi}$$
$$\delta\tan\beta = \delta\tan\alpha + \frac{\Omega_{nd}}{\bar{\phi}^2}\,\delta\phi \tag{A.58}$$

For the first blade row, $\delta\tan\alpha_1$ comes from the inlet duct equation A.15, so:

$$\delta\tan\beta_1(1) = \left(\frac{jn}{|n|\bar{\phi}} - \frac{\tan\bar{\alpha}_{in}}{\bar{\phi}} + \frac{\Omega_{nd}(1)}{\bar{\phi}^2}\right)\delta\phi \tag{A.59}$$

For the other blade rows, the inlet flow angle is equal to the exit flow angle from the previous blade row in the absolute reference frame, assuming no gaps between the blade rows. Using Eqns A.52 and A.58:

$$\delta\tan\alpha_1(k) = \delta\tan\alpha_2(k-1)$$
$$\delta\tan\beta_1(k) = \delta\tan\beta_2(k-1) + \frac{\Delta\Omega_{nd}(k)}{\bar{\phi}(k)^2}\delta\phi(k)$$
$$\delta\tan\beta_1(k) = \frac{\partial\tan\beta_2}{\partial\tan\beta_1}(k-1)\ \delta\tan\beta_1(k-1) + \frac{\Delta\Omega_{nd}(k)}{C(k)\bar{\phi}^2}\delta\phi \tag{A.60}$$

where:

$$\Delta\Omega_{nd}(k) = \Omega_{nd}(k) - \Omega_{nd}(k-1) \tag{A.61}$$

The incidence angle perturbation seen by the k^{th} blade row is function of the $\frac{\partial\tan\beta_2}{\partial\tan\beta_1}$ slopes

[9] Ω_{nd} is defined as $\frac{\Omega r}{a_0}$ and is therefore zero for a stator or IGV

of the previous blade rows. Using Eqn A.60 recursively along with Eqn A.15 yields an expression for the leading edge relative flow angle of the k^{th} blade row as a function of the inlet axial flow coefficient (ϕ). Let's take the third blade row as an example[10]:

$$\begin{aligned}
\delta\tan\beta_1(3) &= \frac{\partial\tan\beta_2}{\partial\tan\beta_1}(2)\left(\frac{\partial\tan\beta_2}{\partial\tan\beta_1}(1)\,\delta\tan\beta_1(1)+\frac{\Delta\Omega_{nd}(2)}{C(2)\bar{\phi}^2}\delta\phi\right)+\frac{\Delta\Omega_{nd}(3)}{C(3)\bar{\phi}^2}\delta\phi \\
&= \left[\frac{\partial\tan\beta_2}{\partial\tan\beta_1}(2)\left(\frac{\partial\tan\beta_2}{\partial\tan\beta_1}(1)\left(\frac{jn}{|n|\bar{\phi}}-\frac{\tan\bar{\alpha}_{in}}{\bar{\phi}}+\frac{\Delta\Omega_{nd}(1)}{C(1)\bar{\phi}^2}\right)+\frac{\Delta\Omega_{nd}(2)}{C(2)\bar{\phi}^2}\right)+\frac{\Delta\Omega_{nd}(3)}{C(3)\bar{\phi}^2}\right]\delta\phi \\
&= \left[\frac{\partial\tan\beta_2}{\partial\tan\beta_1}(2)\frac{\partial\tan\beta_2}{\partial\tan\beta_1}(1)\left(\frac{jn}{|n|\bar{\phi}}-\frac{\tan\bar{\alpha}_{in}}{\bar{\phi}}\right)\right. \\
&\quad \left. \ldots+\frac{\partial\tan\beta_2}{\partial\tan\beta_1}(2)\frac{\partial\tan\beta_2}{\partial\tan\beta_1}(1)\frac{\Delta\Omega_{nd}(1)}{C(1)\bar{\phi}^2}+\frac{\partial\tan\beta_2}{\partial\tan\beta_1}(2)\frac{\Delta\Omega_{nd}(2)}{C(2)\bar{\phi}^2}+\frac{\Delta\Omega_{nd}(3)}{C(3)\bar{\phi}^2}\right]\delta\phi
\end{aligned}$$

so, in general:

$$\delta\tan\beta_1(k)=\frac{1}{\bar{\phi}^2}\sum_{l=1}^{k}\left[\frac{\Delta\Omega_{nd}(l)}{C(l)}\prod_{m=l}^{k-1}\left(\frac{\partial\tan\beta_2}{\partial\tan\beta_1}(m)\right)\right]\delta\phi+\left(\frac{jn}{|n|\bar{\phi}}-\frac{\tan\bar{\alpha}_{in}}{\bar{\phi}}\right)\prod_{m=1}^{k-1}\left(\frac{\partial\tan\beta_2}{\partial\tan\beta_1}(m)\right)\delta\phi \tag{A.62}$$

where the products, $\prod$, are taken to be unity for $m > k-1$. To simplify the algebra, let's denote:

$$d_R(k)=\frac{1}{\bar{\phi}^2}\sum_{l=1}^{k}\left[\frac{\Delta\Omega_{nd}(l)}{C(l)}\prod_{m=l}^{k-1}\left(\frac{\partial\tan\beta_2}{\partial\tan\beta_1}(m)\right)\right]-\frac{\tan\bar{\alpha}_{in}}{\bar{\phi}}\prod_{m=1}^{k-1}\left(\frac{\partial\tan\beta_2}{\partial\tan\beta_1}(m)\right) \tag{A.63}$$

$$d_I(k)=\frac{1}{|n|\bar{\phi}}\prod_{m=1}^{k-1}\left(\frac{\partial\tan\beta_2}{\partial\tan\beta_1}(m)\right) \tag{A.64}$$

so:

$$\boxed{\delta\tan\beta_1(k)=\left(d_R(k)+jn\,d_I(k)\right)\delta\phi} \tag{A.65}$$

Total-to-static pressure rise perturbation

This expression can now be inserted into the isentropic pressure rise perturbation, Eqn A.53, leading to:

[10] $\Delta\Omega_{nd}(1)=\Omega_{nd}(1)$ and $C(1)=1$

$$\delta\psi_{is} = \varrho C^2\bar{\phi}\Big[\tan^2\bar{\beta}_1 - v\tan^2\bar{\beta}_2 + 1 - v\Big]\delta\phi + \varrho C^2\bar{\phi}^2\left[\tan\bar{\beta}_1 - v\tan\bar{\beta}_2\frac{\partial\tan\beta_2}{\partial\tan\beta_1}\right]\Big(d_R + jn\,d_I\Big)\delta\phi$$

$$\delta\psi_{is}(k) = \Bigg(\Upsilon(k)\bar{\phi}\Big[\tan^2\bar{\beta}_1 - v\tan^2\bar{\beta}_2 + 1 - v\Big]_k + \Upsilon(k)\bar{\phi}^2\left[\tan\bar{\beta}_1 - v\tan\bar{\beta}_2\frac{\partial\tan\beta_2}{\partial\tan\beta_1}\right]_k d_R(k)$$

$$\ldots + jn\,\Upsilon(k)\bar{\phi}^2\left[\tan\bar{\beta}_1 - v\tan\bar{\beta}_2\frac{\partial\tan\beta_2}{\partial\tan\beta_1}\right]_k d_I(k)\Bigg)\delta\phi \tag{A.66}$$

or, simply:

$$\delta\psi_{is}(k) = \left[t(k) + t_R(k) + jn\,t_I(k)\right]\,\delta\phi$$

and summing over all the blade rows:

$$\delta\Psi_{is} = [T + T_R + jnT_I]\delta\phi \tag{A.67}$$

where:

$$T = \sum_{\text{all rows}} t = \sum_{\text{all rows}} \Upsilon(k)\bar{\phi}\Big[\tan^2\bar{\beta}_1 - v\tan^2\bar{\beta}_2 + 1 - v\Big]_k \tag{A.68}$$

$$T_R = \sum_{\text{all rows}} t_R = \sum_{\text{all rows}} \Upsilon(k)\bar{\phi}^2\left[\tan\bar{\beta}_1 - v\tan\bar{\beta}_2\frac{\partial\tan\beta_2}{\partial\tan\beta_1}\right]_k d_R(k) \tag{A.69}$$

$$T_I = \sum_{\text{all rows}} t_I = \sum_{\text{all rows}} \Upsilon(k)\bar{\phi}^2\left[\tan\bar{\beta}_1 - v\tan\bar{\beta}_2\frac{\partial\tan\beta_2}{\partial\tan\beta_1}\right]_k d_I(k) \tag{A.70}$$

Similarly for the pressure loss perturbation (Eqn A.57):

$$\delta\psi_{loss} = \varrho C^2\bar{\phi}\bar{\omega}'_l(1 + \tan^2\bar{\beta}_1)\,\delta\phi + \varrho C^2\bar{\phi}^2\left[\frac{(1 + \tan^2\bar{\beta}_1)}{2}\frac{\partial\omega'_l}{\partial\tan\beta_1} + \bar{\omega}'_l\tan\bar{\beta}_1\right]\Big(d_R + jn\,d_I\Big)\,\delta\phi$$

$$\delta\psi_{loss} = \Bigg(\Upsilon\bar{\phi}\,\bar{\omega}'_l(1 + \tan^2\bar{\beta}_1) + \Upsilon\bar{\phi}^2\left[\frac{(1 + \tan^2\bar{\beta}_1)}{2}\frac{\partial\omega'_l}{\partial\tan\beta_1} + \bar{\omega}'_l\tan\bar{\beta}_1\right]_k d_R(k)$$

$$\ldots + jn\,\Upsilon\bar{\phi}^2\left[\frac{(1 + \tan^2\bar{\beta}_1)}{2}\frac{\partial\omega'_l}{\partial\tan\beta_1} + \bar{\omega}'_l\tan\bar{\beta}_1\right]_k d_I(k)\Bigg)\,\delta\phi \tag{A.71}$$

or, simply:

$$\delta\psi_{loss} = [l + l_R + jn\, l_I]\ \delta\phi$$

and summing over all the blade rows:

$$\delta\Psi_{loss} = [L + L_R + jnL_I]\delta\phi \tag{A.72}$$

where:

$$L = \sum_{\text{all rows}} l = \sum_{\text{all rows}} \Upsilon(k)\bar{\phi}\left[\bar{\omega}_l'(1+\tan^2\bar{\beta}_1)\right]_k \tag{A.73}$$

$$L_R = \sum_{\text{all rows}} l_R = \sum_{\text{all rows}} \Upsilon(k)\bar{\phi}^2\left[\frac{(1+\tan^2\bar{\beta}_1)}{2}\frac{\partial\omega_l'}{\partial\tan\beta_1} + \bar{\omega}_l'\tan\bar{\beta}_1\right]_k d_R(k) \tag{A.74}$$

$$L_I = \sum_{\text{all rows}} l_I = \sum_{\text{all rows}} \Upsilon(k)\bar{\phi}^2\left[\frac{(1+\tan^2\bar{\beta}_1)}{2}\frac{\partial\omega_l'}{\partial\tan\beta_1} + \bar{\omega}_l'\tan\bar{\beta}_1\right]_k d_I(k) \tag{A.75}$$

The overall static-to-static pressure rise perturbation is then given by:

$$\begin{aligned}\delta\Psi^{ss} &= \delta\Psi_{is} - \delta\Psi_{loss} \\ &= [T + T_R - L - L_R + jn(T_I - L_I)]\ \delta\phi\end{aligned} \tag{A.76}$$

The total-to-static pressure rise perturbation is found by subtracting the inlet dynamic head perturbation (Eqn A.46) from the above. Using the notation introduced in section A.1.4:

$$\boxed{\delta\Psi^{ts} = (TS_R + jn\, TS_I)\ \delta\phi} \tag{A.77}$$

where:

$$\begin{aligned}TS_R &= T + T_R - L - L_R - \bar{\phi} \\ TS_I &= T_I - L_I - \frac{\bar{\phi}\tan\bar{\alpha}_{in}}{|n|}\end{aligned} \tag{A.78}$$

Exit duct flow angle perturbation

Using Eqns A.52, A.65 and A.58, we can write the relative exit flow angle perturbation as:

$$\begin{aligned}\delta \tan \alpha_{ex} &= \delta \tan \beta_{ex} - \frac{\Omega_{nd}}{\bar{\phi}^2}\,\delta\phi \\ &= \frac{\partial \tan \beta_2}{\partial \tan \beta_1}(N)\delta \tan \beta_1(N) - \frac{\Omega_{nd}}{\bar{\phi}^2}\,\delta\phi \\ &= \frac{\partial \tan \beta_2}{\partial \tan \beta_1}(N)\Big(d_R(k) + jn\, d_I(k)\Big) - \frac{\Omega_{nd}}{\bar{\phi}^2}\,\delta\phi \end{aligned} \tag{A.79}$$

The exit deviation parameters that define the exit duct flow angle perturbation (Eqn A.21) can be expressed as:

$$\begin{aligned} d_{R,ex} &= \frac{1}{\bar{\phi}^2}\sum_{l=1}^{N+1}\left[\frac{\Delta\Omega_{nd}(l)}{C(l)}\prod_{m=l}^{N}\left(\frac{\partial \tan \beta_2}{\partial \tan \beta_1}(m)\right)\right] - \frac{\tan \bar{\alpha}_{in}}{\bar{\phi}}\prod_{m=1}^{N}\left(\frac{\partial \tan \beta_2}{\partial \tan \beta_1}(m)\right) \\ d_{I,ex} &= \frac{1}{|n|\bar{\phi}}\prod_{m=1}^{N}\left(\frac{\partial \tan \beta_2}{\partial \tan \beta_1}(m)\right) \end{aligned} \tag{A.80}$$

Detailed overall compression system dynamics

The overall compression system dynamics are still given by Eqn A.43 with Eqns A.44 and A.45 still representing the stability (σ) and rotational frequency (ω) of the incompressible pre-stall mode, repeated here for completeness:

$$\sigma = \frac{TS_R - |n|\Upsilon_{ex}\bar{\phi}^2\, d_{I,ex}}{\left(\frac{AVDR_{ex}+1}{|n|} + \mu\right)} \tag{A.44}$$

$$\omega = \frac{\lambda - TS_I - \frac{(\Upsilon_{ex}\bar{\phi}^2\, d_{R,ex})}{|n|}}{\left(\frac{AVDR_{ex}+1}{|n|} + \mu\right)} \tag{A.45}$$

The above definitions of TS_R and TS_I give a direct expression of the system's eigenvalue as a function of compressor aerodynamic design parameters.

A.3 Possible addition of unsteady losses and deviations

More detailed compressor dynamics are obtained by including unsteady blade row loss and deviation [16]. The fact that pressure loss and deviation do not respond instantaneously to an axial or tangential flow perturbation can be modeled by a simple time lag on loss and deviation. Within an axially distributed formulation, the loss coefficient and deviation of *each* blade row will be associated to a first order time lag. Lags usually have a stabilizing effect on the system dynamics [31]. Including these time lags increases the number of differential equations (order of the system) and make an analytical expression for the pre-stall mode difficult to obtain. A numerical solution is then necessary. Since the main goal of this appendix is to determine an analytical expression that relates the damping and frequency of the [1,0] pre-stall mode to the compressor design parameters, unsteady losses and deviation were not included, although they could.

APPENDIX B

DESCRIPTION OF THE 2D STALL/SURGE INCEPTION MODELING TOOLBOX: 2DSIM

This appendix describes the *2DSIM Tcolbox* put together throughout the course of this research. It is the result of a collaborative effort with Harald Weigl [45] and includes the state-space formulation of the compressible model by Matthew Feulner [10]. Further details will be included in an internal Gas Turbine Laboratory document [46].

The Toolbox is structured into subdirectories, each one containing Matlab routines implementing a specific part of the stability modeling process shown in Figure 2-3 (p. 40). The first two steps in this process consist of creating the inputs for the stability model and are implemented in the `PreSIM` directory. The third step is to run the stability model, using the routines in the `CompSIM` directory (compressible model) or the `IncSIM` directory (incompressible model). Finally, the analysis of the modeling results is done using the routines in the `PostSIM` directory. Figure B-1 summarizes the directory structure.

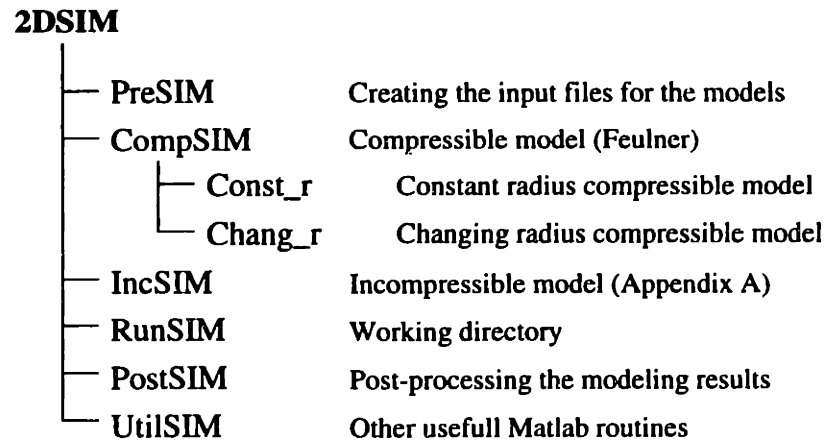

Figure B-1: Structure of the 2D Stall/Surge Inception Modeling Toolbox.

Running the models

The input files are created, the model is run, and the results are analyzed all from the `RunSIM` directory. When Matlab is started from this directory, it reads a `startup.m` file giving it access to files in the other directories.

Utilities to execute different parts of the stability modeling procedure are contained in `UtilSIM` and in the respective directories.

The following sections describe the new routines completing the stability modeling process. The model itself is described in detail by Feulner [10], Weigl [45], and in Chapter 2 of this thesis.

B.1 Creating the inputs: PreSIM

The inputs to the model are created in two steps: 1) calculate the steady flow, then 2) model the steady flow and derive the slopes.

B.1.1 Steady flow calculation

The steady flow calculation implemented in this Toolbox is a compressible mean-line calculation, as described in many turbomachinery books. The flow along the mean-line[1] is assumed one-dimensional, varying only in the axial direction. It is calculated at each leading edge and trailing edge, i.e. across each blade row, gap and duct.

The flow across ducts and gaps is determined from mass conservation, total pressure and total temperature conservation, along with angular momentum conservation. The hub and casing boundary layers reduce the effective area seen by the mean-line flow. This effect is introduced by an empirical blockage parameter:

$$\bar{k} = \frac{A_{effective}}{A_{geometric}} \tag{B.1}$$

reducing the area at each axial location where the continuity equation is applied. Bleeds within the gaps are included as reductions of mass flow across the gap.

The flow across rotors and stators is determined by the following steps:

1. Relative total temperature conservation[2]:

$$T'_{t,2} = T'_{t,2} + \frac{\Omega^2}{2C_p}(r_2^2 - r_1^2) \tag{B.2}$$

2. Relative total pressure loss coefficient:

$$P'_{t,2} = P'_{t,2\,is} - \omega'_l(P'_{t,1} - P_1) \tag{B.3}$$

where $P'_{t,2\,is}$ is the isentropic relative total pressure at the trailing edge and ω'_l is an

[1]The mean-line is the radial location separating the flow in two equal parts.
[2]Relative total temperature conservation is equivalent to the Euler turbine equation.

empirical loss coefficient defined as:

$$\omega_l' = \frac{P_{t,2\,is}' - P_{t,2}'}{P_{t,1}' - P_1} \tag{B.4}$$

3. Blade row exit flow angle is directly determined by the trailing edge blade metal angle and the deviation.

4. Mass conservation at the trailing edge:

$$\frac{M_2'}{\left(1 + \frac{\gamma-1}{2} M_2'^2\right)^{\frac{\gamma+1}{2(\gamma-1)}}} = \frac{\dot{m}\sqrt{T_{t,2}}}{A_{eff,2} P_{t,2}} \sqrt{\frac{R}{\gamma}} \tag{B.5}$$

   For the trailing edge Mach number to be extracted from this non-linear equation, it is solved iteratively.

This approach introduces three types of performance parameters:

- deviation ($\delta°$) for each blade row;
- loss coefficient (ω_l') for each blade row;
- blockage ($\bar{k}$) at each leading edge and trailing edge.

They may be based on correlations, calculated using CFD, or derived from experimental measurements. When the compressor information consists of experimental measurements (such as P, P_t, and T_t), the mean-line flow can be calculated by iteratively:

1. choosing a set of performance parameters ($\delta°$, ω_l', $\bar{k}$);
2. calculating the mean-line flow ($P_t(x)$, $T_t(x)$, $V_x(x)$, $V_\theta(x)$);
3. comparing the calculated and measured values.

These steps are repeated until the calculated values equal the experimental measurements, or are within the measurement error bounds. The performance parameters have therefore been determined.

These performance parameters and the geometry (mean radius, annulus area, blade row leading edge and trailing edge metal angles) is the only compressor information needed for

the mean-line calculation. The output of this calculation is the mean-line flow, completely described by: $P_t(x)$, $T_t(x)$, $V_x(x)$, and $V_\theta(x)$.

B.1.2 Steady flow modeling

The geometry and steady flow are modeled in *2DCompSIM* as constant in each duct, gap and blade row. The axially varying steady flow calculated previously must therefore be modeled to be consistent with the stability model. Average values of the mean flow and geometry (annulus area and radius) are taken in the gaps and ducts. The mean flow in the blade passages is determined according to *2DCompSIM*'s blade row model, described in Section 2.1.

B.1.3 Slope calculation

The loss coefficient and deviation are mostly a function of incidence and inlet relative Mach number for a given blade row. The method used to determine the slopes ($\frac{\partial \omega_1'}{\partial inc}$, $\frac{\partial \omega_1'}{\partial M_1'}$, $\frac{\partial dev}{\partial inc}$, $\frac{\partial dev}{\partial M_1'}$) depends on the compressor information available. If the loss and deviation are calculated from correlations or CFD, the slopes can be obtained by perturbing the input incidence or Mach number to the calculation. The slope is then the ratio of change in the output (loss or deviation) to change in the input (incidence or Mach number).

If the performance parameters were derived from experimental measurements, the slopes can be determined by combining the loss and deviation at different operating points. At each operating point, the steady flow calculation determined the incidence and Mach number into each blade row, and the resulting loss coefficient and deviation. These parameters can be plotted versus incidence and Mach number. The gradients of a function fitted through these points are the slopes. This approach is implemented in the Toolbox, using a second order polynomial in incidence and Mach number as the function fitted, with the possibility for a cross term of incidence times Mach number.

Since the performance information varies depending on the compressor analyzed, different Matlab routines were created for specific tasks. They are described in `README` files within subdirectories created for each compressor.

B.2 Analyzing the results: `PostSIM`

The output from *2DCompSIM* is a state-space representation of the compression system dynamics (Eqn 2.25 repeated here):

$$\dot{\vec{x}} = [A]\,\vec{x} + [B]\,\vec{u}$$
$$\vec{y} = [C]\,\vec{x} + [D]\,\vec{u}$$

The eigenvalues of $[A]$ represent the stability and rotational speed of each pre-stall mode. They can be calculated using Matlab's eigenvalue solver (`eig`).

An eigen-decomposition of this system also allows the calculation of the flow field perturbations (δP, $\delta \rho$, δV_x, δV_θ) associated with each mode. These pre-stall flow fields can then be plotted, as in Figure 2-5 (p. 51). These pre-stall perturbations are also used to evaluate the various terms in the Disturbance-energy Corollary and to calculate the disturbance-power of each blade row (Chapter 3).

BIBLIOGRAPHY

[1] BONNAURE, L. P. "Modelling High Speed Multistage Compressor Stability". Master's thesis, Massachusetts Institute of Technology, 1991.

[2] BROWN, R. G. *Introduction to Random Signal Analysis and Kalman Filtering.* John Wiley & Sons, 1983, ch. 1.

[3] CUMPSTY, N. A. *Compressor Aerodynamics.* Addison Wesley Longman Limited, England, 1989.

[4] CUMPSTY, N. A., AND MARBLE, F. E. "The Generation of Noise by the Fluctuations in Gas Temperature into a Turbine". CUED/A Turbo/TR 57, University of Cambridge, 1974.

[5] DAY, I. J. "Stall Inception in Axial Flow Compressors". *ASME Journal of Turbomachinery, Vol. 115* (January 1993), pp. 1–9.

[6] DOWLING, A. P., AND FFOWCS WILLIAMS, J. E. *Sound and Sources of Sound.* Ellis Horwood Limited, 1983.

[7] EMMONS, H. W., PEARSON, C. E., AND GRANT, H. P. "Compressor Surge and Stall Propagation". *ASME Transactions, Vol. 27* (April 1955), pp. 455–469.

[8] EPSTEIN, A. H., 1996. Personal communications.

[9] EPSTEIN, A. H., FFOWCS WILLIAMS, J. E., AND GREITZER, E. M. "Active Suppression of Aerodynamics Instabilities in Turbomachines". *AIAA Journal of Propulsion and Power, Vol. 5*, No. 2 (1989), pp. 204–211.

[10] FEULNER, M. R. *Modeling and Control of Rotating Stall in High Speed Mutli-Stage Axial Compressors.* PhD thesis, Massachusetts Institute of Technology, May 1994.

[11] FLETCHER, R. *Practical Methods of Optimization*, vol. 2, Constrained Optimization. John Wiley & Sons, 1980.

[12] GARNIER, V. H. "Rotating Stall Waves as a Stall Inception Indication in Axial Compressors". *ASME Journal of Turbomachinery, Vol. 113* (April 1991), pp. 290–302.

[13] GORRELL, S. E., AND RUSSLER, P. M. "Stall Inception in a High-Speed Low Aspect Ratio Fan Including the Effects of Casing Treatment". ASME IGTI Conference at The Hague, Netherlands (1994).

[14] GREITZER, E. M. "The Stability of Pumping Systems - The 1980 Freeman Scholar Lecture". *Journal of Fluids Engineering, Vol. 103* (June 1981), pp. 193–242.

[15] GYSLING, D. L. "Dynamic Control of Rotating Stall in Axial Flow Compressors Using Aeromechanical Feedback". GTL Report No. 219, Massachusetts Institute of Technology, August 1993.

[16] HAYNES, J. M., HENDRICKS, G. J., AND EPSTEIN, A. H. "Active Stabilization of Rotating Stall in a Three-Stage Axial Compressor". *ASME Journal of Turbomachinery, Vol. 116*, No. 2 (April 1994), pp. 226–239.

[17] HENDRICKS, G. J., BONNAURE, L. P., LONGLEY, J. P., GREITZER, E. M., AND EPSTEIN, A. H. "Analysis of Rotating Stall Onset in High Speed Axial Flow Compressors". AIAA Paper No. 93-2233 (June 1993).

[18] HENDRICKS, G. J., SABNIS, J. S., AND FEULNER, M. R. "Analysis of Instability Inception in High-Speed Multi-Stage Axial-Flow Compressors". ASME/IGTI Paper No. 96-GT-360 (June 1996).

[19] HOYING, D. A. *Blade Passage Flow Structure Effects on Axial Compressor Rotating Stall Inception.* PhD thesis, Massachusetts Institute of Technology, Septembre 1996.

[20] HYNES, T. P. "Actuator and Semi-actuator Disk Models of Compression Systems Operating with Inlet Distorsion". CUED/A Turbo/TR 104, University of Cambridge, 1980.

[21] HYNES, T. P., AND GREITZER, E. M. "A Method for Assesing Effects of Circumferential Flow Distorsion on Compressor Stability". *ASME Journal of Turbomachinery, Vol. 109* (July 1987), pp. 371–379.

[22] JONHSEN, I. A., AND BULLOCK, R. O. "Aerodynamic Design of Axial-Flow Compressors". Tech. Rep. SP-36, NASA, 1965.

[23] KAJI, S., AND OKAZAKI, T. "Propagation of Sound Waves Through a Blade Row, Part I: Analysis Based on the Semi-Actuator Disk Theory". *Journal of Sound and Vibration, Vol. 11*, No. 3 (1970), pp. 339–353.

[24] KERREBROCK, J. L. "Waves and Wakes in Turbomachine Annuli with Swirl". AIAA Paper No. 74-87 (January 1974).

[25] KERREBROCK, J. L. *Aircraft Engines and Gas Turbines*, 2nd ed. The MIT Press, Cambridge, Massachusetts, 1992.

[26] KIRCHHOFF, G. *Vorlesungen über mathematische Physik: Mechanik*, 2 ed. Teubner, Leipzig, 1877, pp. 311–336.

[27] KOCH, C. C. "Stalling Pressure Rise Capability of Axial Flow Compressor Stages". *Journal of Engineering for Power, Vol. 103* (October 1981), pp. 645–656.

[28] KOVASZNAY, L. S. G. "Turbulence in Supersonic Flow". *Journal of the Aeronautical Sciences, Vol. 20* (October 1953), pp. 657–674.

[29] LEJAMBRE, C. R., December 1996. Personal communications.

[30] LEJAMBRE, C. R., ZACHARIAS, R. M., BIEDERMAN, B. P., GLEIXNER, A. J., AND YETKA, C. J. "Development and Application of a Multistage Navier-Stokes Flow Solver - Part II: Application to a High Pressure Compressor Design". ASME/IGTI Paper No. 95-GT-343 (June 1995).

[31] LONGLEY, J. P. "A review of non-steady flow models for compressor stability". *ASME Journal of Turbomachinery, Vol. 116* (1994), pp. 202–215.

[32] LOUGHERY, R. J., HORN, R. A., AND TRAMM, P. C. "Single-Stage Experimental Evaluation of Boundary Layer Blowing and Bleed Techniques for High Lift Stator Blades - V. Final Report". Contractor Report CR-54573, NASA, March 1971.

[33] MAZZAWY, R. S. "Multiple Segment Parallel Compressor Model for Circumferential Flow Distorsion". *ASME Journal of Engineering for Power, Vol. 99* (April 1977).

[34] MOORE, F. K. "A Theory of Rotating Stall of Multistage Compressors - Parts I-II-III". *ASME Journal of Engineering for Gas Turbines and Power, Vol. 106* (April 1984), pp. 313–336.

[35] MOORE, F. K., AND GREITZER, E. M. "A Theory of Post-Stall Transients in Axial Compressors: Part I - Development of the Equations". *ASME Journal of Engineering for Gas Turbines and Power, Vol. 108* (1986), pp. 68–76.

[36] MORFEY, C. L. "Acoustic Energy in Non-Uniform Flows". *Journal of Sound and Vibration, Vol. 14*, No. 2 (1971), pp. 159–170.

[37] MYERS, M. K. "Transport of Energy by Disturbances in Arbitrary Steady Flows". *Journal of Fluid Mechanics, Vol. 226* (1991), pp. 383–400.

[38] PADUANO, J. D. "Active Control of Rotating Stall in Axial Compressors". GTL Report No. 208, Massachusetts Institute of Technology, June 1993.

[39] PIERCE, A. D. *Acoustics: An Introduction to its Physical Principles and Applications.* McGraw-Hill, 1981.

[40] REIJNEN, D. P. *Experimental Study of Boundary Layer Suction in a Transonic Compressor.* PhD thesis, Massachusetts Institute of Technology, Februrary 1997.

[41] SUN, X.-F. "Three-Dimensional Compressible Flow Stability Theory of Rotating Stall". BUAA Technical Report BH-B4765, Beijing University of Aeronautics and Astronautics, Department of Jet Propulsion, May 1996.

[42] TRYFONIDIS, M., ETCHEVERS, O., PADUANO, J. D., EPSTEIN, A. H., AND HENDRICKS, G. J. "Prestall Behavior of Several High-Speed Compressors". *ASME Journal of Turbomachinery, Vol. 117* (1995), pp. 62–80.

[43] VAN SCHALKWYK, C. M. "Active Control of Rotating Stall with Inlet Distorsion". GTL Report No. 222, Massachusetts Institute of Technology, June 1996.

[44] VO, H. D. "Active Control of Rotating Stall in a Three-Stage Axial Compressor with Jet Actuators". Master's thesis, Massachusetts Institute of Technology, February 1997.

[45] WEIGL, H. J. *Active Stabilization of Rotating Stall and Surge in a Transonic Single Stage Axial Compressor.* PhD thesis, Massachusetts Institute of Technology, expected June 1997.

[46] WEIGL, H. J., AND FRÉCHETTE, L. G. "An update on Compressible Stall Inception Modeling". MIT Gas Turbine Laboratory, Internal document, 1997.

[47] WEIGL, H. J., PADUANO, J. D., FRÉCHETTE, L. G., EPSTEIN, A. H., GREITZER, E. M., BRIGHT, M. M., AND STRAZISAR, A. J. "Active Stabilization of Rotating Stall and Surge in a Transonic Single Stage Axial Compressor". Paper submitted for presentation at the 1997 ASME/IGTI International Gas Turbine and Aero-engine Congress & Exhibition.

[48] WHITEHEAD, D. S. "The Vibration of Air in a Duct with a Subsonic Mean Flow". *The Aeronautical Quarterly* (February 1961), pp. 34–40.